

1

[ATLAS Semivisible Jets]

2

[Elena Laura Busch]

3

Submitted in partial fulfillment of the
requirements for the degree of
Doctor of Philosophy
under the Executive Committee
of the Graduate School of Arts and Sciences

4

5

6

7

8

COLUMBIA UNIVERSITY

9

2024

10

© 2024

11

[Elena Laura Busch]

12

All Rights Reserved

13

Abstract

14

[ATLAS Semivisible Jets]

15

[Elena Laura Busch]

16

Abstract of dissertation (place-holder).

Table of Contents

18	Acknowledgments	xv
19	Dedication	xvi
20	Introduction or Preface	1
21	I Theory	2
22	Chapter 1: The Standard Model	3
23	1.1 Phenomenology: Particles and Forces	3
24	1.1.1 Particles	3
25	1.1.2 Forces	5
26	1.2 QCD and Jets	7
27	1.3 Symmetries	8
28	1.3.1 Spontaneous Symmetry Breaking and The Higgs Mechanism	9
29	1.4 Experimental Validation of the Standard Model	10
30	1.5 Limitations of the Standard Model	11
31	Chapter 2: Physics Beyond the Standard Model	13
32	2.1 Hidden Valley Models	13
33	2.2 Dark QCD	14

34	2.3 Semi-visible Jets	15
35	II Experiment	17
36	Chapter 3: The Large Hadron Collider	18
37	3.1 Accelerator Physics	19
38	3.1.1 The Journey of a Proton	19
39	3.1.2 Magnets	20
40	3.2 Luminosity	21
41	3.3 LHC Timeline	24
42	Chapter 4: The ATLAS Detector	26
43	4.1 Coordinate System and Geometry	27
44	4.2 Inner Detector	28
45	4.2.1 Pixel Detector	29
46	4.2.2 Semiconductor Tracker	31
47	4.2.3 Transition Radiation Tracker	31
48	4.3 Calorimeters	31
49	4.3.1 Liquid Argon Calorimeter	32
50	4.3.2 Tile Calorimeter	35
51	4.4 Muon Spectrometer	36
52	4.5 Magnet System	38
53	4.6 Forward Detectors	39
54	4.7 Trigger and Data Acquisition	40

55	Chapter 5: Particle Reconstruction and Identification	44
56	5.1 Inner Detector Tracks	44
57	5.2 Photons and Electrons	46
58	5.3 Muons	48
59	5.4 Jets	50
60	5.4.1 Calorimeter Clusters	51
61	5.4.2 Particle Flow Algorithm	52
62	5.4.3 Jet Clustering	54
63	5.4.4 Ghost Track Association	56
64	5.5 Missing Transverse Energy	57
65	III Search	59
66	Chapter 6: Monte Carlo and Data	60
67	6.1 Data	60
68	6.2 Simulation	61
69	6.2.1 Simulated Backgrounds	61
70	6.2.2 Signal Simulation	62
71	Chapter 7: Machine Learning Tools	65
72	7.1 Introduction	65
73	7.1.1 Particle Flow Network (Supervised)	66
74	7.1.2 ANTELOPE (Semi-supervised)	76
75	Chapter 8: Analysis Strategy	83

76	8.1 Preselection	83
77	8.2 SVJ Fit and Discovery Analysis Strategies	85
78	8.3 Analysis Regions	89
79	8.3.1 Control and Validation Regions	89
80	8.3.2 Signal Region	91
81	8.4 Background Estimation	93
82	8.5 Fit Strategy and Validation	94
83	8.5.1 SVJ Fit Strategy	94
84	8.5.2 Discovery Strategy	102
85	Chapter 9: Results	108
86	Conclusion or Epilogue	109
87	References	113
88	Appendix A: Trigger Studies	119
89	Appendix B: Machine Learning Approaches	123
90	B.1 Unsupervised: AE vs. ANTELOPE	123
91	B.2 PFN Optimality Checks	124
92	B.3 Supervised: BDT vs. PFN	127
93	B.4 Single Jet vs Jet System ML Approach	127
94	B.5 PFN Training Composition	129
95	B.6 E_T^{miss} and $E_T^{\text{miss}}\phi$ Shapes	131

96	B.6.1 NCB Preselection	131
97	B.6.2 TileCal Correction	133
98	Appendix C: Truth Studies	136
99	C.1 Jet dR Matching	136
100	Appendix D: BumpHunter	138
101	D.1 Signal Mass Resolution m_T Binning	138

List of Figures

103	1.1	Diagram of the 17 particles comprising the Standard Model	4
104	1.2	Fundamental particle interactions of the three fundamental forces described by the	
105		Standard Model [2].	6
106	1.3	An example Feynmann diagram of jet production	7
107	1.4	An illustration of the “hat shaped” potential of the Higgs field, resulting in a non-	
108		zero vacuum expectation value.	9
109	2.1	Illustration of the hidden valley potential.	14
110	2.2	The massive mediator particle Z' of the s-channel realization of a HV model . . .	14
111	3.1	The LHC accelerator complex at CERN [29]	20
112	3.2	The octants of the LHC and location of various beam activities [28]. Stars indicate	
113		the locations of beam collisions, and the associated detectors recording the	
114		outcome of those collisions.	21
115	3.3	(Left) Total integrated luminosity over the course of Run 2. (Right) Average num-	
116		ber of pp interactions per bunch crossing in Run 2. Each curve is weighted by the	
117		integrated luminosity for the year.	23
118	3.4	Timeline of LHC and HL-LHC activities [31]. Integrated luminosity estimates are	
119		approximate, and not reflective of the exact amount delivered to each experiment. .	25
120	4.1	The ATLAS detector [34].	26
121	4.2	ATLAS coordinate system and geometry	29
122	4.3	A 3D visualization of the structure of the ID in the barrel region [35]	30

123	4.4 A 3D visualization of the structure of the ID end-caps [34]. The paths of two charged particles ($\eta = 1.4$ and 2.2) are illustrated.	30
124		
125	4.5 ATLAS calorimetry system [36]	32
126		
127	4.6 Diagram of a segment of the EMB, demonstrating the accordion plate arrangement and the cell segmentation pattern [37]. Three layers are illustrated, and the variation in the cell granularity between the front layer (Layer 1) and the back layer (Layer 3) is shown.	33
128		
129		
130	4.7 A LAr pulse as produced in the detector (triangle) and after shaping (curve) [37] . .	34
131		
132	4.8 Readout gap structure in HEC [37]	35
133		
134	4.9 TileCal wedge module [40]	36
135		
136	4.10 Cross section view of the muon spectrometer system [41]	37
137		
138	4.11 Layout of the barrel and end-cap toroid magnets [34]	39
139		
140	4.12 Block diagram of the L1 trigger process [34]. The overall L1 trigger decision is made by the CTP.	41
141		
142		
143		
144		
145	4.13 Block diagram of the trigger and data acquisition processes, including L1 and HLT processes [45].	42
146		
147		
148		
149		
150		
151	5.1 This graphic illustrates a slice of ATLAS detector barrel [46]. A photon, electron, and two jets (associated to the proton and neutron) are shown, illustrating each object's interaction with various ATLAS subsystems. The path of the charged particles is curved on account of the strong magnetic field produced by the solenoid and toroid magnets. A neutrino, generally representing the reconstruction of missing transverse energy, is also illustrated.	45
152		
145	5.2 Track reconstruction seeding, finding and fitting illustration [47]	46
146		
147	5.3 Three types of EM object candidates [49].	47
148		
149		
150		
151	5.4 The four types of muon track candidates [51]. The red bands indicate where detector measurements for each muon track candidate are made. The dashed lines indicate the path of the muon through detectors where no measurement is made. Standalone muons is another term for extrapolated muon.	50
152		
151	5.5 The fragmentation and hadronization processes undergone by a quark produced in a proton-proton collision [53].	51
152		

153	5.6 A flow chart illustrating the particle flow algorithm progression [56]. The solid 154 lines indicate the progression of tracks through the algorithm, while the dotted 155 lines indicate the progression of clusters. The process begins with track selection 156 and continues until the energy associated with the tracks has been removed from 157 the calorimeter. At the end charged particle tracks, unmodified topo-clusters, and 158 the remnants of topo-clusters which have had part of their energy removed remain.	53
159	5.7 A comparison of jet clustering with four different jet algorithms. The anti- k_t al- 160 gorithm is observed to create the most conical jets, where the shape of the jet is 161 immune to the presence of soft radiation [57].	55
162	5.8 A comparison of MC simulation and data for $Z \rightarrow \mu\mu$ events where real $E_T^{\text{miss}} =$ 163 0 [65]. The resolution of the missing energy in the transverse ($x - y$) plane is 164 observed to increase with increasing total $\sum E_T$	58
165	6.1 The transverse momentum slices of the QCD MC simulation, overlayed to show 166 how they come together to create a smooth distribution (left) once weighted prop- 167 erly. The original unweighted distribution is shown on the right, illustrating the 168 enhanced statistics for the high p_T range.	62
169	6.2 Background processes relevant to the SVJ signal. The agreement between the black 170 line (data) and grey line (all MC processes combined) illustrates that this collection 171 of background processes is sufficient to model the expected E_T^{miss} in the selected 172 data events.	63
173	7.1 The Energy/Particle Flow Network concept, from Ref. [71].	67
174	7.2 An annotated diagram of the PFN architecture. y and ϕ represent geometric in- 175 formation for the input particles, z represents energy information, and PID encom- 176 passes any other particle ID information in the input.	67
177	7.3 A illustration of the expected dijet behavior of semi-visible jets, where one jet is 178 closely aligned with E_T^{miss}	68
179	7.4 Illustration of track coordinates d_0 and z_0	69
180	7.5 Distributions of the track multiplicity in the leading and subleading jets, comparing 181 signal and background PFN training samples.	69
182	7.6 A diagram demonstrating how the two jet system is rotated in (ϕ, η)	70

183	7.7 The 6 PFN track variables in background MC and signal MC. There are some 184 differences between signal and background, but the track kinematics are largely 185 similar.	70
186	7.8 The 6 PFN track variables in data and background MC, after the scaling and ro- 187 tation procedure is applied. There is excellent modeling of the data by the MC 188 within the track variables. The slight discrepancy in the phi distribution is due to 189 the modeling of dead TileCal cells by the QCD MC, which will be discussed in 190 Chapter 8. The level of discrepancy is determined to be within tolerance given that 191 the final result will be data driven and the QCD model is used in the PFN training 192 only.	71
193	7.9 PFN score for background MC, data, and signal, comparing a PFN training on 194 QCD-only vs all-background MC samples. The average AUC for the QCD-only 195 training (left) is 0.93, while the average AUC for the mixed background training 196 (right) is 0.84. The sensitivity estimate across the grid is better for the QCD-only 197 training - from the distribution we can conclude that this is because the sensitivity 198 to MET enhanced signals is greatly reduced.	73
199	7.10 PFN architecture loss during training as a function of epoch (left) and the evaluated 200 loss over the signal and background (right).	73
201	7.11 ROC the PFN score for combined signal (true positive) and QCD background (false 202 positive).	74
203	7.12 AUC from the PFN score for each signal in the SVJ grid, shown versus the QCD- 204 only training sample.	75
205	7.13 PFN score for two signals and the total background MC (top), and between data 206 and MC (bottom). The difference between data and MC efficiency is minimal (< 207 5%).	75
208	7.14 A visual representation of the 64 PFN latent space variables which create the input 209 of the VAE component of ANTELOPE. The left shows a 2D histogram of the PFN 210 latent space index (0-63) versus the value assumed by that index. The right shows 211 1D histograms of two particular PFN latent space variables.	77
212	7.15 An annotated diagram of the ANTELOPE architecture.	78
213	7.16 ANTELOPE architecture loss during training as a function of epoch.	79
214	7.17 ANTELOPE score distribution comparing data and the total background MC (left), 215 with good agreement observed between data and simulated background, and com- 216 paring all background MC to signals (right), revealing good discrimination power. 217	80

218	7.18 AUC from the ANTELOPE score for each signal in the SVJ grid.	81
219	7.19 Comparing data and the alternate signal models for the PFN score (left) and AN-	
220	TELOPE score (right). The emerging jet signal is an example of the gain of the	
221	model-independent ANTELOPE approach, where it has a bimodal shape in PFN	
222	score but is clearly tagged as anomalous by ANTELOPE.	82
223	7.20 Comparing data and the alternate signal models in terms of sensitivity (S/\sqrt{B}) for	
224	the PFN and ANTELOPE tools, applying the selection that is used in the analysis.	
225	The ANTELOPE network is found to provide significant added sensitivity to alter-	
226	nate signals such as the gluino → R-hadron and emerging jets, which have higher	
227	E_T^{miss} than the SVJs.	82
228	8.1 Preselection cutflow for data (left) and signal (right).	84
229	8.2 Energy and momentum analysis variables at preselection, for data, all background	
230	MC and representative signal models. m_T is the key fit variable, and this plot	
231	illustrates the smoothly falling background in comparison to the resonant shape of	
232	the signals. m_T is further illustrated in Figure 8.9.	86
233	8.3 Orientation analysis variables at preselection, for data, all background MC and	
234	representative signal models. While $\Delta\phi(E_T^{\text{miss}}, j)$ variables are not used explicitly	
235	in the analysis flow, they help create a picture of the event.	87
236	8.4 Flow of analysis selections, regions, and background estimation/validation fitting	
237	strategy. TODO: diagram needs to be corrected	88
238	8.5 Distributions of the subleading jet width width_{j2} (left) and leading jet with width_{j1}	
239	(right) in data, background MC and signals at preselection. All SVJ signals are	
240	seen to be wider than the background in width_{j2} . The same is not true for width_{j1} ,	
241	where some signals are observed to closely match the background.	89
242	8.6 2D plots revealing correlations between width_{j2} and m_T (left), width_{j2} and ML	
243	score (middle), and m_T with ML score (right). For the top row, the ML score is	
244	the PFN score, and for the bottom three, the ML score is the ANTELOPE score.	
245	Minimal correlations are observed and are shown to not sculpt m_T , validating these	
246	variables for analysis region construction and statistical treatment.	90
247	8.7 m_T in simulation across the CR, VR, and SR for both PFN (left) and ANTELOPE	
248	(right) selections.	91

249	8.8 Definition of CR, VR, and SR regions using width_{j2} and the ML score, along with 250 the population of each region in data statistics. The SVJ Fit region is shown on top 251 with the PFN score on the x-axis, and Discovery region is shown on the bottom, 252 with the ANTELOPE score on the x-axis.	92
253	8.9 The resonant shape of the SVJ signals in m_T , in contrast to the smoothly falling 254 m_T background. The high R_{inv} signals (right) boast a wider shape, making them 255 more difficult to detect, while the low R_{inv} signals(left) produce a more narrow 256 resonance in m_T	93
257	8.10 Background-only m_T fits using representative MC in the CR (left), VR (middle), 258 and SR (right).	95
259	8.11 Background-only m_T fits using data in the full statistics CR and VR regions. . . .	96
260	8.12 Post-fit parameters for the PFN CR and VR. $p1$ can also be considered N_{bkg} or the 261 normalization factor.	96
262	8.13 m_T distribution in the data CR, before (left) and after (right) smoothing.	97
263	8.14 Background-only m_T fits using pseudo-data from the CR template.	98
264	8.15 p -value histograms from 100 fits to Asimov data in the CR.	98
265	8.16 Example S+B fit on a background m_T spectrum with injected signal from the point 266 ($4000 \text{ GeV}, R_{inv}=0.2$).	99
267	8.17 Measured signal at a variety of injected values (1x, 2x, and $5\sqrt{b}$), for all signal 268 points in the grid, $R_{inv}=0.2$ (top left), 0.4 (top right), 0.6 (bottom left), and 0.8 269 (bottom right).	100
270	8.18 95% C.L. upper limits for signal models across Z' mass, for four different R_{inv} frac- 271 tions, from the CR region (without systematics). TODO - ATLAS style	101
272	8.19 95% C.L. upper limits and observed limit for signal models across Z' mass, with 273 varying amounts of signal injected. TODO - ATLAS style	102
274	8.20 Post-fit function and residuals for the ANTELOPE CR and VR.	103
275	8.21 Post-fit parameters for the ANTELOPE CR and VR.	103
276	8.22 BumpHunter fits on the ANTELOPE m_T spectra for both the CR (left) and VR 277 (right). In a signal-depleted region, good agreement with the background estima- 278 tion is observed.	104

279	8.23 BumpHunter p-values extracted for 100 Asimov toys for both the ANTELOPE CR	105
280	(left) and VR (right).	
281	8.24 Example injected gaussian signal.	105
282	8.25 Response of the BumpHunter framework to signal injection of 5σ significance to	
283	the model-dependent polynomial fit framework. The local significance (top) and	
284	bump location (bottom) are shown.	107
285	8.26 Example BH response to gaussian signal injection at 4000 GeV with width of 10%. 107	
286	A.1 Trigger yield and efficiency for both the MET trigger and small-R jet trigger ap-	
287	proach. Each entry represent a signal point, labelled by the Z' mass and the	
288	R_{inv} fraction.	119
289	A.2 The factor of improvement in S/\sqrt{B} for each trigger method compared to the un-	
290	triggered case.	120
291	A.3 The ratio of S/\sqrt{B} of jet trigger over E_T^{miss} trigger selection.	120
292	A.4 Analysis variables where high R_{inv} signals a clearly distinct from background and	
293	low R_{inv} variables. On the contrary, leading jet p_T is one of the only variables	
294	where low R_{inv} signals are distinct from background.	122
295	A.5 OR of jet and E_T^{miss} triggers.	122
296	B.1	123
297	B.2	124
298	B.3 AUC from the PFN score for each signal in the SVJ grid, shown versus the QCD-	
299	only training sample (top) and the total MC background (bottom). Note the three	
300	missing points will be added shortly - they were delayed due to a DAOD production	
301	mistake.	125
302	B.4 Comparison of PFN AUC (top), SIC (middle), and sensitivity in the m_T mass win-	
303	dow (bottom) for a single PFN model (left) vs. two models, trained on $R_{inv} < 0.5$	
304	and > 0.5 separately.	126
305	B.5 Preferred cuts on the PFN score for each point in the grid, comparing the effect of	
306	adding the NCB preselection.	127
307	B.6 Scans done to check for optimality of PFN training parameters.	128

308	B.7	128
309	B.8 ϕ Performance comparison between single jet and jet system ML approach	129
310	B.9 ϕ Comparison in the AUC score across the grid for the mixed background strategy	
311	vs the QCD only strategy. The bottom table highlights that the QCD only strategy	
312	gives superior sensitivity across the signal grid.	130
313	B.10 E_T^{miss} in data before and after Tight event cleaning is applied.	131
314	B.11 E_T^{miss} vs jet1 p_T in data before and after Tight event cleaning is applied.	132
315	B.12 η vs ϕ for leading and subleading jets, before and after the application of tight	
316	cleaning.	132
317	B.13 Added NCB preselection and impact on E_T^{miss} shape.	133
318	B.14 NCB preselection impact on data and signal yields.	134
319	B.15 Impact of tight cleaning and non-collision background preselection.	135
320	B.16 $E_T^{\text{miss}}\phi$ in data, before (left) and after (right) application of the TileCal correction	
321	tool.	135
322	C.1 Index of jets truth matched (by requirement of $\Delta R < 0.4$) with dark quark.	136
323	C.2 Percent of jets with $\Delta R(j, E_T^{\text{miss}}) < 0.4$ comparing two jet identification strategies.	
324	Leading and subleading jets are seen to be the better metric for identifying jets	
325	associated with the dark quark decay.	137
326	D.1 Example determinations of the 60% mass window means for several signal points.	139
327	D.2 Signal mass resolution for m_T binning for the signal grid in (R_{inv} , mass) space.	139
328	D.3 m_T bins based on the signal mass resolution and the minimum 100 GeV width	
329	requirement, for each R_{inv} signal category.	140

List of Tables

331	4.1 General performance goals of the ATLAS detector [34].	27
332	6.1 Fixed parameters in the Pythia8 HV model	64
333	6.2 Values for m_{dark}	64
334	6.3 Mass points and cross sections of the SVJ search signal grid	64

335

Acknowledgements

336 Insert your acknowledgements text here. This page is optional, you may delete it if not

337 needed.

338

Dedication

339

Dedicated to my friends and family

340

Introduction or Preface

341 Insert your preface text here if applicable. This page is optional, you may delete it if not
342 needed. If you delete this page make sure to move page counter comment in thesis.tex to correct
343 location.

344

Part I

345

Theory

Chapter 1: The Standard Model

348 The Standard Model of particle physics is a universally accepted framework which explains
 349 the interactions of fundamental particles. All known fundamental particles, outlined in Figure
 350 1.1, are represented in the Standard Model. The model describes three of the four known forces:
 351 the electromagnetic force, the weak force, and the strong force. Gravity, the fourth fundamental
 352 force, is not addressed by the Standard Model. The Standard Model was primarily developed over
 353 the course of the 1960s and 1970s, by combining the work of many physicists into one coherent
 354 model. The Standard Model has been established as a well-tested theory by decades of experimen-
 355 tal physics research.

356 This chapter will seek to introduce the phenomenology and mathematical foundations of the
 357 Standard Model, and present the supporting experimental evidence. Phenomenon which are unex-
 358 plained by the Standard Model such as gravity will be considered at the end of the chapter, leading
 359 to an exploration of theories beyond the Standard Model in the subsequent chapter.

360 **1.1 Phenomenology: Particles and Forces**

361 1.1.1 Particles

362 A classic representation of the particles comprising the Standard Model is shown in Figure
 363 1.1. The two primary particles classes are bosons (gauge bosons and the scalar Higgs boson) and
 364 fermions (leptons and quarks). The bosons are carriers of fundamental forces, while the fermions
 365 are the building blocks of matter. Fermions are sorted into three *generations*, and each fermion is
 366 identified by a unique *flavor*.

367 Each entry in the table in Figure 1.1 is accompanied by 3 characteristic numbers: mass, charge,
 368 and spin. The mass of each particle is determined to limited precision by experimental observation,

Standard Model of Elementary Particles

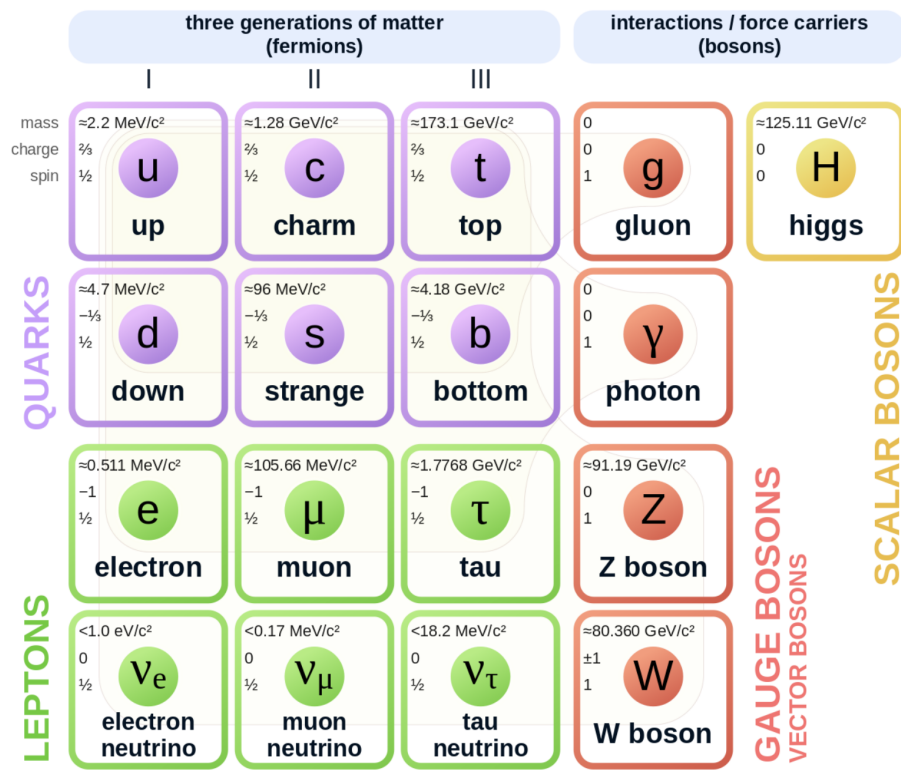


Figure 1.1: Diagram of the 17 particles comprising the Standard Model

³⁶⁹ with the exception of photons and gluons which are known to be massless. Charge refers to the
³⁷⁰ electromagnetic charge, which is integer for leptons and fractional for quarks. Spin is an intrinsic
³⁷¹ form of angular momentum carried by fundamental particles; all fermions have half integer spin,
³⁷² while bosons have integer spin.

³⁷³ Each particle is also known to have an *antiparticle*. Each antiparticle has the same mass but the
³⁷⁴ opposite charge of their Standard Model counter part; for example, the antiparticle of the electron
³⁷⁵ is the positron, which has all the same properties but a positive charge. The photon, Z boson,
³⁷⁶ and Higgs are each their own antiparticle. The nature of antineutrinos is an open question driving
³⁷⁷ neutrino physics research, as it is not currently known whether neutrinos are their own antiparticle.

³⁷⁸ 1.1.2 Forces

³⁷⁹ The three fundamental forces explained by the Standard Model are the electromagnetic force,
³⁸⁰ the strong force, and the weak force. The photon is the carrier of the electromagnetic force, which
³⁸¹ dictates the nature of interactions between electrically charged particles, and is widely covered by
³⁸² introductory physics courses. The electromagnetic force has an infinite interaction range, a result
³⁸³ of the massless and non-self interaction nature of the photon. The electromagnetic interaction is
³⁸⁴ described by the theory of quantum electrodynamics (QED).

³⁸⁵ The weak force gives rise to atomic radiation and decay. It allows for the processes of beta
³⁸⁶ decay, which enables conversion between neutrons and protons within the nucleus of an atom. In
³⁸⁷ the process of beta decay, a proton decays into a neutron, a positron, and a neutrino; or, a neutron
³⁸⁸ decays into a proton, an electron and an antineutrino. The weak interaction allows for quark flavor
³⁸⁹ mixing, the which enables beta decay. The W^+ , W^- , and Z^0 are the force carriers of the weak force.
³⁹⁰ The effective range of the weak force is limited to subatomic distances, as a result of the massive
³⁹¹ nature of the mediator bosons. The unified theory of the electroweak interaction posits that at high
³⁹² enough energies the electromagnetic interaction and the weak force merge into the same force.
³⁹³ This threshold is termed the unification energy and calculated to be about 246 GeV [1].

³⁹⁴ The strong force confines quarks into hadron particles, such as protons and neutrons. The

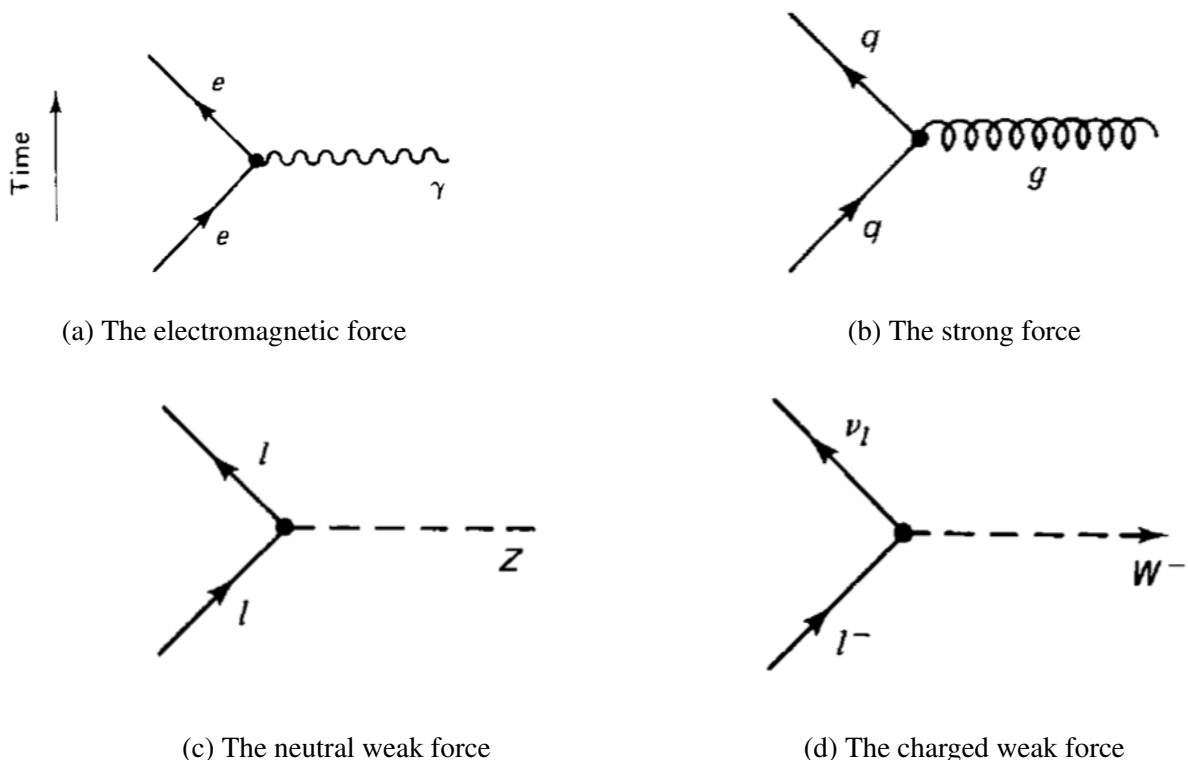


Figure 1.2: Fundamental particle interactions of the three fundamental forces described by the Standard Model [2].

395 strong force also allows for the creation of atomic nuclei by binding protons and neutrons together,
396 and is generally referred to as the “nuclear force” in this context. The gluon is the mediator of
397 the strong force, which is a short-range force which acts at subatomic distances on the order of
398 10^{-15} m. At this range, the strong force is about 100x as strong as the electromagnetic force,
399 which allows for the creation of positively charged nuclei [2]. The strong force is described by the
400 theory of quantum chromodynamics (QCD). In the same way that QED dictates the interaction of
401 electrically charges particles, QCD dictates the interactions of *color-charged* particles. Due to the
402 particular importance of QCD in this thesis, this topic will be explored in detail in section 1.2.

403 The fundamental Feynmann diagram for each of the three forces discussed here is depicted
404 in Figure 1.2. The fourth fundamental force, gravity, is not currently explained by any known
405 mechanism within the Standard Model.

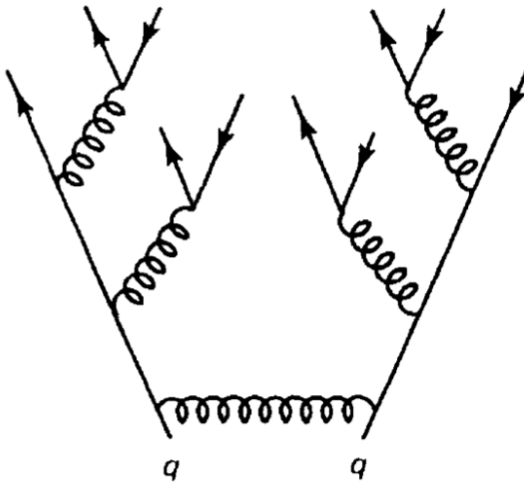


Figure 1.3: An example Feynmann diagram of jet production

406 1.2 QCD and Jets

407 While there is only one type of electric charge, there are three types of color charge; red, green,
 408 and blue. In the process $q \rightarrow q + g$, the color of the quark can change. In order to conserve color
 409 charge, gluons are bicolored, and always carry some positive color charge and some negative color
 410 charge.

411 Color charged particles can only exist in bound states which result in a neutral total color
 412 charge, a principle known as confinement. This requires that quarks and gluons exist in group
 413 states known as hadrons; either mesons in the case of two quarks or baryons in the case of three
 414 quarks. When a quark is separated from a hadron, confinement dictates that other colored objects
 415 are produced around the quark to obey confinement. An example of this process is shown in
 416 Figure 1.3. This ensemble of objects, generally a mixture of quarks and gluons, is termed a *jet*.
 417 Jets are among the most common phenomenon observed by detectors at hadron colliders, and their
 418 complex structure makes them a key focus of many physics analyses.

419 **1.3 Symmetries**

420 The Standard Model is a renormalizable quantum field theory that obeys the local symmetry

421 G_{SM} :

$$G_{SM} = SU(3)_C \times SU(2)_L \times U(1)_Y. \quad (1.1)$$

422 The $SU(3)_C$ symmetry component represents the non-Abelian gauge group of QCD. There
423 are 8 generators for the $SU_C(3)$ group which correspond to 8 types of gluon, each representing a
424 different superposition of color charge [3]. The $SU(2)_L \times U(1)_Y$ symmetry group represents the
425 electroweak sector of the Standard Model, which can be spontaneously broken into the electromag-
426 netic and weak sectors. There are 4 generators for this group, which correspond to four massless
427 gauge bosons W^1 , W^2 , W^3 , and B . From these massless gauge bosons are formed the massive
428 mediators of the weak force, the W^- , W^+ and Z^0 bosons, and the massless electromagnetic force
429 carrier, the photon γ . Spontaneous symmetry breaking and the process by which gauge bosons
430 acquire mass will be addressed in section 1.3.1.

431 Noether's theorem [4] stipulates that any continuous symmetry is associated with a conserved
432 quantity. In the Standard Model, this means that the $SU(3)_C$ symmetry gives rise to conservation of
433 color charge. The $SU(2)_L \times U(1)_Y$ symmetry gives rise to conservation of electromagnetic charge.
434 Conservation of spin results from the Poincaré symmetry described by the theory of special rela-
435 tivity, which combined with Noether's theorem gives us the conservation of energy, momentum,
436 and angular momentum.

437 The SM Lagrangian is invariant under CPT symmetry, or charge, parity, and time reversal.
438 Charge conjugation (C) transform a particle into its corresponding antiparticle by reversing the
439 charge and other quantum numbers. Parity conjugation (P) reverses spatial coordinates, which
440 transforms left-handed particles into right-handed particles and vice-versa. Time reversal (T) is
441 the theoretical process of reversing time. The L subscript in the $SU(2)_L$ group indicates that this
442 symmetry only applies to left-handed fermions. As a result, the $W^{1,2,3}$ gauge bosons of $SU(2)_L$

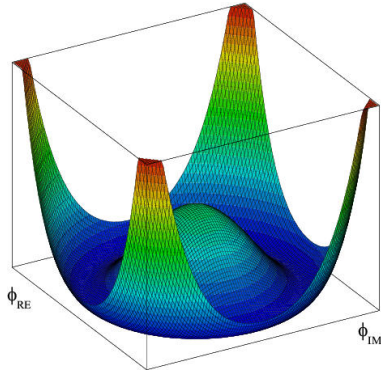


Figure 1.4: An illustration of the “hat shaped” potential of the Higgs field, resulting in a non-zero vacuum expectation value.

only interact with left handed particles, a process which maximally violates P-symmetry in the weak force. A small amount of the CP symmetry violation is also observed in the Standard Model, through the decays of strange flavored mesons [5] and b -mesons [6]. The CPT theorem posits that the violation of CP symmetry implies that T-symmetry must also be violated, so that CPT is a preserved symmetry.

1.3.1 Spontaneous Symmetry Breaking and The Higgs Mechanism

Spontaneous symmetry breaking is the process by which a Lagrangian obeys a symmetry at high energies, but exhibits asymmetric behavior at lower energies. The electroweak symmetry group is spontaneously broken as $SU(2)_L \times U(1)_Y \rightarrow U(1)_{EM}$. The quantity conserved by the $SU(2)_L$ symmetry is weak isospin $T_{1,2,3}$, while the quantity conserved by $U(1)_Y$ symmetry is weak hypercharge Y . Below very high energies, the presence of the Higgs field causes the electroweak symmetry to break. The Higgs field is a scalar field which forms a complex doublet of the $SU(2)$ symmetry group, with four degrees of freedom. The shape of the Higgs field potential, shown in Figure 1.4, results in a ground state with a non-zero vacuum expectation value; thus the Higgs field takes a non-zero value throughout all space, which breaks the symmetry of the weak isospin $SU(2)$ group.

The interaction with the Higgs field mixes the four massless gauge bosons $W^{1,2,3}$ and B . Three Higgs field degrees of freedom mix with the massless gauge bosons, resulting in three massive

461 gauge bosons W^- , W^+ and Z^0 . The massless photon γ is created from the components of the
462 massless gauge bosons which do not interact with the Higgs field. The scalar Higgs boson arises
463 from the one unmixed degree of freedom the Higgs field. Spontaneous symmetry breaking also
464 violates the conservation of weak isospin and weak hypercharge, leaving only electromagnetic
465 charge ($Q = T_3 + \frac{1}{2}Y$) as a conserved quantity associated with the $U(1)_{EM}$ symmetry.

466 1.4 Experimental Validation of the Standard Model

467 The theoretical framework of the Standard Model coalesced into a unified theory in the mid-
468 20th century. A cascade of discoveries providing empirical evidence for the model followed
469 closely. In the 1960s, three quarks (up, down and strange) and four leptons (electron, muon,
470 and their associated neutrinos) were the known particulate building blocks of matter and the Stan-
471 dard Model. The discovery of the charm quark in 1974, through the observation of the J/ψ meson
472 [7][8], confirmed the existence of a fourth quark flavor. The discovery of the τ in 1975 [9] provided
473 the first evidence of a 3rd generation of matter. This was quickly followed by the observation of
474 the Υ meson in 1977 [10], which provided evidence for the existence of a fifth quark, the b quark
475 (bottom, or beauty). The existence of a 3rd generation of fermion also explained the observation
476 of CP violation in the weak force, as it allowed for the addition of a complex phase in the CKM
477 matrix (a unitary matrix which describes flavor mixing in the weak interaction). The top quark
478 (t) and tau neutrino (ν_τ) were predicted at this point as the final building blocks of three complete
479 generations of fermions, and they were discovered by experimental observation around the turn of
480 the 21st century [11] [12] [13].

481 The W and Z bosons were predicted by the Standard Model, but to observe them required the
482 construction of a particle accelerator powerful enough to produce them. They were finally observed
483 at CERN in 1983 by the UA1 and UA2 experiments [14] [15] at the newly constructed Super Proton
484 Synchrotron (SPS). Their masses were observed to be compatible with the masses predicted by the
485 Standard Model nearly a decade earlier. The final missing piece then was confirming the existence
486 of the Higgs, which again required the construction of a newer and more powerful collider. CERN

487 achieved this with the construction of the Large Hadron Collider (LHC), and in 2012 the ATLAS
488 and CMS experiments announced the discovery of the Higgs particle [16] [17].

489 **1.5 Limitations of the Standard Model**

490 While the Standard Model has enjoyed decades of experimental results which confirm its pre-
491 dictions, there are several glaring shortcomings. The observed phenomenon for which the Standard
492 Model provides no explanation are summarized below.

- 493 • Gravity - the Standard Model does not account for the fourth fundamental force of gravity.
- 494 • Dark Matter - there is no viable candidate to explain the existence of dark matter, a non-
495 interacting form of matter which must exist to account for gravitational observations which
496 cannot be explained by general relativity, such as the motion of galaxies, gravitational lens-
497 ing, and the structure of the universe [18].
- 498 • Matter-Antimatter asymmetry - the level of CP violation in the Standard Model isn't suf-
499 ficient to explain the large discrepancy between the amount of matter and the amount of
500 antimatter in the universe today, and the origins of this imbalance are not understood.
- 501 • Neutrino masses - the Standard Model assumes that neutrinos are massless and provides
502 no mechanism for them to acquire mass. However, observations of neutrino oscillations
503 indicates they posses some small non-zero mass [19].

504 In addition to these unexplained natural phenomenon, there are several questions about the
505 *naturalness* of the Standard Model. The principle of naturalness states that dimensionless ratios
506 between physical constants should be of order 1, and that nature should not be arbitrarily fine-
507 tuned. While this is largely an aesthetic argument, it points to many aspects of the Standard Model
508 for which there exists no natural explanation.

- 509 • Strong CP - while CP symmetry is violated in the weak force, observations indicate that it
510 is preserved by the strong force [20]. The Standard Model predicts that CP violation in the

511 strong force is possible. There is no principle which motivates this incongruity between the
512 weak force and strong force.

- 513 • Hierarchy Problem - The wide range of masses for elementary particles and the wide range of
514 scales at which the four fundamental forces operate is not motivated by the SM. Specifically,
515 it is not understood why the Higgs mass is observed to be well below the Plank scale λ ,
516 which is the energy level at which the effects of quantum gravity become significant. QFT
517 indicates that the Higgs mass is determined by contributions from all energy scales including
518 λ , meaning that its observed mass is inexplicably small.

519 The limitations of the Standard Model provide a road map for theoretical and experimental
520 particle physicists, who seek to develop new theories which account for these observations, and
521 then to find evidence which might support these *Beyond the Standard Model* (BSM) theories. The
522 next chapter will introduce the BSM theories which motivate the physics search presented in this
523 thesis.

Chapter 2: Physics Beyond the Standard Model

526 In light of the various phenomenon unexplained by the Standard Model, physicists have pro-
 527 posed various extensions to the Standard Model, collectively termed *Beyond the Standard Model*
 528 (BSM) theories. A particular focus of the physics programs at the Large Hadron Collider (LHC)
 529 are BSM models which suggest dark matter candidate particles. If these particles couple to Stan-
 530 dard Model, they could be produced and observed at the LHC. This chapter will explore Hidden
 531 Valley models, and in particular the potential for Hidden Valley models to produce *semi-visible*
 532 *jets*. This will set the theoretical foundations for the experimental search presented in the later
 533 chapters of this thesis. The mechanisms of dark QCD that arise from these models and allow for
 534 the production of semi-visible jets will also be discussed.

535 **2.1 Hidden Valley Models**

536 Hidden Valley (HV) models are a category of BSM models that allow for dark matter (DM)
 537 production at the LHC. They extend the Standard Model with an additional non-Abelian gauge
 538 group [21]. This introduces the possibility of a complex dark sector, which mirrors the complexities
 539 of Standard Model QCD, and introduces the possibility of dark quarks and gluons. The term
 540 “hidden valley” refers to the idea that the DM is hidden from the SM by a high-energy barrier, as
 541 illustrated in Figure 2.1. The dark sector is assumed to communicate with the Standard Model via
 542 a “portal”, or “messenger particle”, that can interact with both Standard Model and HV forces. For
 543 the s-channel scenario, the portal is considered to be a new massive mediator particle Z' .

544 The portal particle allows for the production of dark sector particles at hadron colliders. If
 545 dark quarks are produced via the decay $Z' \rightarrow q_D q_D$ they can hadronize and form dark jets. The
 546 properties of the dark jets are determined by the dynamics of the dark sector, which are explored in

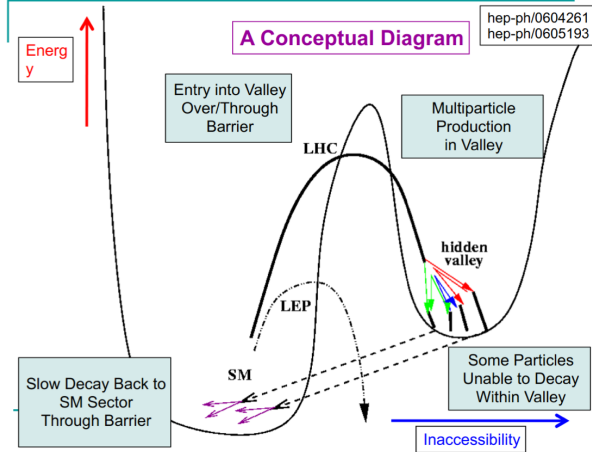


Figure 2.1: Illustration of the hidden valley potential.

547 the subsequent section. Depending on the details of the model, the jets formed by the dark hadrons
 548 can be categorized as fully dark, semi-visible, leptonic, emerging, or other [21].

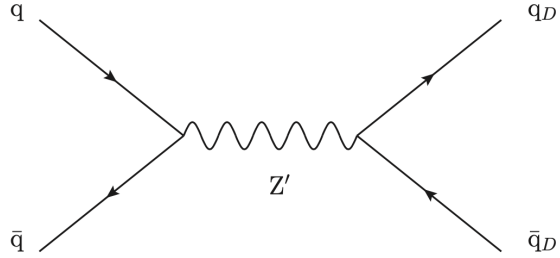


Figure 2.2: The massive mediator particle Z' of the s-channel realization of a HV model

549 2.2 Dark QCD

550 The theoretical underpinning of the semi-visible jet phenomenology is a dark sector with a
 551 gauge group $SU(N)_d$ leading to confinement at a scale Λ_d . For illustration, let's consider the
 552 case of an $SU(2)_d$ gauge theory, which gives rise to two dark fermionic generations $\chi_a = \chi_1, \chi_2$.
 553 Following the work of Ref [22] we can write the fundamental dark Lagrangian as:

$$\mathcal{L}_{dark} \supset -\frac{1}{2} \text{Tr} G_{\mu\nu}^d G^{d\mu\nu} - \bar{\chi}_a (i\cancel{D} - M_{d,a}) \chi_a \quad (2.1)$$

554 The first term allows for the dark gluons to self-interact, while the second term enables the dark
555 quarks to hadronize and acquire mass. The dark quarks are assumed to have a common mass M_d .

556 The coupling strength of the strongly interacting dark quarks is termed α_d . At the confinement
557 scale Λ_d , the dark quarks can form bound states. At the scale $M_d \approx \Lambda_d$ a QCD-like shower occurs.

558 The properties of the hadrons formed by the dark quarks are of particular importance to the
559 observed dark QCD dynamics. Dark-isospin number $U(1)_{1-2}$ and dark-baryon number $U(1)_{1+2}$
560 are accidental symmetries of the theory which determine the stability of the hadrons. In the case
561 of two dark flavors, six dark hadrons can be formed: four mesons ($\chi_1\bar{\chi}_1$, $\chi_2\bar{\chi}_2$, $\chi_1\bar{\chi}_2$, $\bar{\chi}_1\chi_2$) and
562 two baryons ($\bar{\chi}_1\bar{\chi}_2$, $\bar{\chi}_1\chi_2$). The mesons $\chi_1\bar{\chi}_2$ and $\bar{\chi}_1\chi_2$ are charged under dark-isospin and will be
563 stable if this symmetry is unbroken. The baryons would also be stable as they are charged under
564 the dark-baryon number. These four stable hadrons become dark matter candidates of the theory.

565 The $\chi_1\bar{\chi}_1$ and $\chi_2\bar{\chi}_2$ mesons are not charged under either symmetry and are thus expected to decay.
566 The unstable mesons can decay into stable dark mesons, or into an off-shell Z' . The off-shell Z'
567 will then decay into two DM quarks or two SM quarks, and its products will continue to shower
568 until the final state particles are stable.

569 The number of stable and unstable dark states varies substantially depending on the details
570 of the model. The model discussed above can be generalized from $SU(2)_d$ to $SU(N)_d$, with any
571 number of colors N_c or flavors N_f . This affects the ratio of possible stable to unstable mesons,
572 which can directly impact the amount of missing energy. The fraction of missing energy is a
573 variable in many dark QCD models, and is especially important in the case of semi-visible jets.

574 2.3 Semi-visible Jets

575 A “semi-visible jet” occurs when the heavy Z' messenger particle decays into dark quarks,
576 which then hadronize in a QCD-like shower. If some of the dark hadrons are stable while others
577 decay to SM quarks via the off-shell Z' , a collimated mixture of visible and dark matter is formed
578 – this is termed a semi-visible jet. If the Z' messenger particle is produced at rest, the two jets will
579 be back-to-back in the transverse plane. If there is an imbalance in the amount of invisible particles

580 between the two jets, one of the jets will be observed to be aligned with missing transverse energy.

581 While there are a myriad of HV and dark QCD models, a handful of model parameters are most
582 important in determining the observable of these showers within a particle detector. The coupling
583 strength α_d is one of the most important, as it controls the fraction of dark hadrons emitted in the
584 shower and their average p_T . The mass of the dark quarks directly impacts the jet mass. If the
585 masses of the dark quark flavors are comparable, the ratio of stable to unstable dark hadrons will
586 be approximately 1:1. However, if there is a mass splitting, stable or unstable dark hadrons may
587 be favored, which impacts the amount of missing energy observed.

588 The ratio of stable to unstable dark hadrons in the shower is a critical variable for capturing the
589 behavior of dark showers. This value is termed R_{inv} :

$$R_{inv} = \frac{\# \text{ of stable hadrons}}{\# \text{ of hadrons}} \quad (2.2)$$

590 Events containing jets aligned with missing transverse momentum are generally considered to
591 be misreconstructed by other DM searches, and therefore discarded. This class of final states is
592 therefore largely uncovered by existing DM searches. The nature of the dark hadron shower is
593 determined by the following parameters: the Z' mass $m_{Z'}$, the Z' couplings to visible and dark
594 quarks g_q and g_{q_D} , the number of dark colors and flavors, the characteristic scale of the dark sector
595 confinement Λ_D , the mass scale of the dark hadrons m_D , and the average fraction of stable hadrons
596 in the decay R_{inv} . The coupling to SM quarks determines the Z' production cross section.

597

Part II

598

Experiment

Chapter 3: The Large Hadron Collider

601 The Large Hadron Collider (LHC) is a 26.7 km circular high-energy particle accelerator, span-
602 ning the Swiss-French border near the city of Geneva, Switzerland [23]. The LHC occupies the
603 tunnel constructed in 1989 for the Large Electron-Positron (LEP) Collider, and reaches a maxi-
604 mum depth of 170m below the surface. The LHC is operated by the European Organization for
605 Nuclear Research (CERN), the largest international scientific collaboration in the world.

606 The LHC accelerates protons and heavy ions, and collides them at four interaction points
607 around the ring, with a design center-of-mass energy per collision of $\sqrt{s} = 14$ TeV. Each interaction
608 point is home to one of four detector experiments, which study the products of the collisions. The
609 largest of these experiments is the ATLAS detector, a general purpose detector designed to study
610 the Standard Model and search for new physics that could be produced in LHC collisions [24].
611 The CMS detector is another general purpose detector, designed and operated independently of the
612 ATLAS detector, but intended to probe the same range of physics [25]. The ALICE experiment is
613 a dedicated heavy ion experiment, and the LHC-b experiment is a dedicated *b*-physics experiment
614 [26] [27].

615 This chapter will cover the multi-component accelerator complex powering the LHC, the state-
616 of-the-art magnets which steer the particle beams, measurements of the intensity and number of
617 collisions produced by the LHC, and finally an overview of LHC activities in the past, present, and
618 future.

619 **3.1 Accelerator Physics**

620 **3.1.1 The Journey of a Proton**

621 From 2010 - 2018, the protons which fed the LHC started as hydrogen gas. The electrons were
622 removed from the hydrogen atoms through the use of strong electric fields. The linear accelerator
623 LINAC2 then accelerated the protons to an energy of 50 MeV. Between 2018 and 2020, LINAC2
624 was replaced with LINAC4, which instead accelerates H^- ions, hydrogen atoms with two electrons.
625 LINAC4 is capable of accelerating the H^- ions to 160 MeV. Before injection to the next part of
626 the acceleration chain, both electrons are stripped from the H^- ions, leaving just protons. From
627 here the protons enter the Proton Synchrotron booster, where they are accelerated up to 1.4 GeV of
628 energy. Subsequently they are sorted into bunches separated in time by 25 ns, where each bunch
629 contains approximately 10^{11} protons. Next the bunches pass through the Proton Synchrotron (PS)
630 and the Super Proton Synchrotron (SPS), where they reach energies of 25 GeV and 450 GeV
631 respectively. Finally they are injected into the LHC as two beams traveling in opposite direction.
632 The original design allowed each beam to be accelerated up to 7 TeV of energy. Due to limitations
633 in the performance of the superconducting LHC magnets, the highest energy actually achieved by
634 the LHC beams during Run 2 was 6.5 TeV, giving a collision center-of-mass energy of $\sqrt{s} = 13$
635 TeV [28]. Figure 3.1 shows the full LHC accelerator complex.

636 Acceleration in the LHC is performed by eight radio frequency (RF) cavities located around the
637 ring. Each RF cavity produces a 2 MV electric field oscillating at 40 MHz. The 40MHz oscillation
638 produces a point of stable equilibrium every 2.5 ns. These points of equilibrium are synchronized
639 with the occurrence of the proton bunches produced in the PS – a proton bunch occupies one out
640 of every ten points of stable equilibrium, such that the bunches maintain a 25 ns spacing [28].

641

The CERN accelerator complex Complexe des accélérateurs du CERN

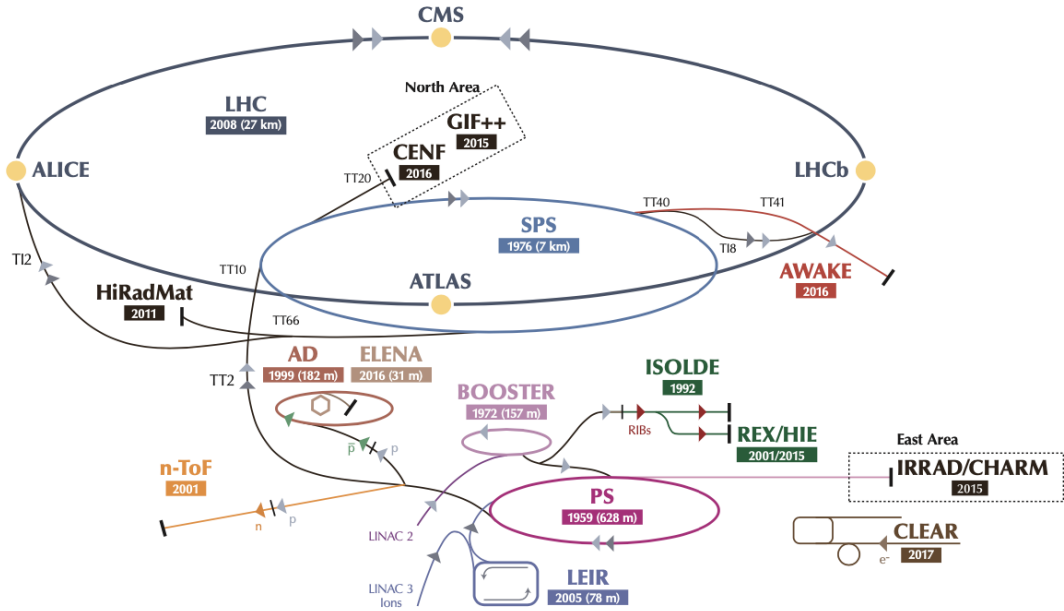


Figure 3.1: The LHC accelerator complex at CERN [29]

642 3.1.2 Magnets

643 In addition to the acceleration cavities, the LHC houses 9593 superconducting magnets which
 644 direct and focus the proton beam on its 27 kilometer journey. The magnets are comprised of super-
 645 conducting Niobium-Titanium coils cooled to 1.9K by superfluid helium. As the beams approach
 646 one of the four collision points around the ring, multipole magnets focus and squeeze the beam for
 647 optimal collisions [28].

648 The LHC is divided into sections, where each section contains an arc and a straight insertion. The arcs are composed of 1232 large dipole magnets which bend the beam
 649 to follow the roughly circular 27 km path. The main dipoles generate powerful 8.3 tesla magnetic
 650 fields to achieve this bend. Each dipole magnet is 15 meters long and weighs 35 tonnes. The
 651 dipoles work in conjunction with quadrupole magnets, which keep the particles in a focused beam,
 652 and smaller sextupole, octupole and decapole magnets which tune the magnetic field at the ends of
 653 the dipole magnets [30].

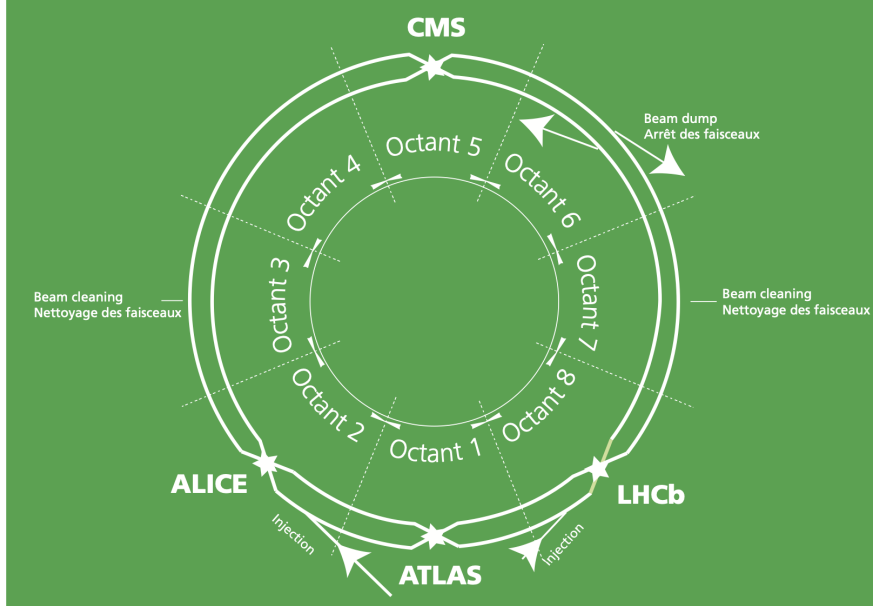


Figure 3.2: The octants of the LHC and location of various beam activities [28]. Stars indicate the locations of beam collisions, and the associated detectors recording the outcome of those collisions.

655 The straight insertion sections have different purposes depending on their location around the
 656 ring: beam collisions, beam injection, beam dumping, or beam cleaning. At the four collision
 657 points, insertion magnets squeeze the beam to ensure a highly focused collision. This is accom-
 658 plished with a triplet of quadrupole magnets, which tighten the beam from 0.2 millimeters to just
 659 16 micrometers in diameter. Insertion magnets also clean the beam, which prevents stray particles
 660 from hitting sensitive components throughout the LHC. When the LHC is ready to dispose of a
 661 beam of particles, beam dump magnets deflect the path of the beam into a straight line towards
 662 a block of concrete and graphite that stops the beam. A dilution magnet then reduces the beam
 663 intensity by a factor of 100,000 before the final stop [30]. Figure 3.2 shows the locations various
 664 beam activities.

665 3.2 Luminosity

666 Collisions at the LHC occur when the two beams of proton bunches cross at one of the four
 667 interaction points. The intensity of collisions is described by the instantaneous luminosity, the

668 formula for which is given in equation 3.1.

$$L = \frac{fN_1N_2}{4\pi\sigma_x\sigma_y} \quad (3.1)$$

669 Here f is the revolution frequency, N_1 and N_2 are the number of particle per bunch for each
670 beam, and σ_x , σ_y are the horizontal and vertical beam widths.

671 The instantaneous luminosity gives the number of the collisions that could be produced at the
672 interaction point per unit of cross-sectional area per unit of time, generally expressed in $\text{cm}^{-2}\text{s}^{-1}$.
673 The integrated luminosity is obtained by integrating the instantaneous luminosity over a given
674 block of time, and measures the total number of collisions which have occurred during that op-
675 eration period. The total integrated luminosity is directly correlated with the size of the datasets
676 collected by the LHC experiments. Total integrated luminosity for Run 2 is illustrated in Figure
677 3.3.

678 High levels of instantaneous luminosity result in multiple pp collisions per bunch crossing,
679 which leads to an effect known as *pileup*. Pileup poses a challenge for detector physics, as recon-
680 structing the products of multiple simultaneous events is far more challenging than reconstructing
681 a single event with no pileup. Pileup conditions vary from year-to-year and run-to-run of LHC op-
682 eration, and the impact of these conditions are taken into account when analyzing the data, as will
683 be discussed further in Chapter 5. Measurement of pileup conditions during Run 2 are illustrated
684 in Figure 3.3.

685 The design peak luminosity of the LHC is $1.0 \times 10^{34} \text{ cm}^{-2}\text{s}^{-1}$. During Run 1 of the LHC the
686 peak instantaneous luminosity was $0.8 \times 10^{34} \text{ cm}^{-2}\text{s}^{-1}$. Over the course of Run 1 the LHC collected
687 a total integrated luminosity of 5.46 fb^{-1} at $\sqrt{s} = 7 \text{ TeV}$, and 22.8 fb^{-1} at $\sqrt{s} = 8 \text{ TeV}$. Following the
688 first long shutdown and upgrade phase of operations, the LHC achieved a center of mass energy
689 $\sqrt{s} = 13 \text{ TeV}$ at the beginning of Run 2 in 2015. The LHC was also able to deliver 2.0×10^{34}
690 $\text{cm}^{-2}\text{s}^{-1}$ peak instantaneous luminosity, double the design value. During LHC Run 2, from 2015-
691 2018, the LHC delivered 156 fb^{-1} of integrated luminosity for proton-proton collisions. Run 3 of

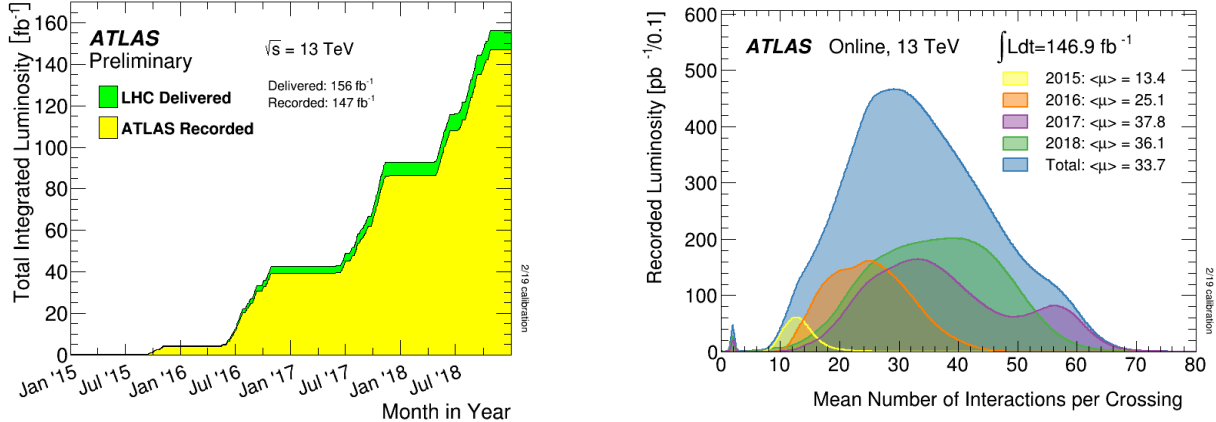


Figure 3.3: (Left) Total integrated luminosity over the course of Run 2. (Right) Average number of pp interactions per bunch crossing in Run 2. Each curve is weighted by the integrated luminosity for the year.

the LHC began in 2022, and is expected to deliver 250 fb^{-1} of integrated luminosity to the ATLAS and CMS experiments by 2026 [31].

The goal of LHC physic analyses is to find and study rare events produced by interesting physics processes. The cross section σ of a given process indicates the probability of that process occurring given the beam conditions of the LHC. Multiplying the cross section by the integrated luminosity of a dataset gives the expected number of events for that process within the dataset.

$$N_{\text{events}} = \int \sigma L(t) dt = \mathcal{L} \times \sigma \quad (3.2)$$

The cross section for most processes of interest, especially BSM processes, is several orders of magnitude below the total cross section for the LHC. Therefore maximizing the number of events produced in collisions is crucial to increase the likelihood of producing events from processes of interest. For this reason, maximizing instantaneous luminosity is a key factor in accelerator design and operation, while mitigating the resulting pileup effects is a key component in detector design and operation.

704 **3.3 LHC Timeline**

705 The first proton-proton collisions at the LHC were achieved in 2010 with a center-of-mass
706 energy of $\sqrt{s} = 7$ TeV. Run 1 of the LHC took place between 2010 and early 2013, during which
707 time the center-of-mass collision energy increased from 7 TeV to 8 TeV. Figure 3.4 shows an
708 overview of LHC activities beginning in 2011, in the midst of Run 1. The data collected during
709 Run 1 led to the discovery of the Higgs Boston in 2012 [32].

710 Between 2013 and 2015 the LHC underwent the first Long Shutdown (LS1) during which
711 time maintenance and renovation was performed on the accelerator chain, including the repair and
712 consolidation of the high-current splices which connect the super-conducting LHC magnets. Run
713 2 of the LHC took place from 2015 to 2018 and achieved a center-of-mass energy of $\sqrt{s} = 13$ TeV.
714 Analysis of data collected in Run 2 is still on going, and is the subject of study in this thesis.

715 Between 2018 and 2022 the LHC underwent the second Long Shutdown (LS2), allowing for
716 further detector and accelerator maintenance and upgrades. Key improvements to the LHC in-
717 cluded the improvement of the insulation for over 1200 diode magnets, and the upgrade from
718 LINAC2 to LINAC4 mentioned in Section 3.1.1. Run 3 of the LHC began in 2022 and achieved a
719 center-of-mass energy of $\sqrt{s} = 13.6$ TeV.

720 Run 3 is scheduled to continue through 2026, at which point the LHC machine and detectors
721 will undergo upgrades for the *high luminosity* LHC (HL-LHC). The HL-LHC will increase the
722 instantaneous machine luminosity by a factor of 5 - 7.5 with respect to the nominal LHC design.
723 The bottom panel of Figure 3.4 shows an overview of the preparation work for the HL-LHC that
724 has been going on concurrently with Run 1, 2, and 3 of the LHC [33].



Figure 3.4: Timeline of LHC and HL-LHC activities [31]. Integrated luminosity estimates are approximate, and not reflective of the exact amount delivered to each experiment.

Chapter 4: The ATLAS Detector

The ATLAS detector (**A** Toroidal **L**H**C** Apparatu**S**) is one of two general purpose physics detectors designed to study the products of proton-proton collisions at the LHC. The detector is composed of a variety of specialized subsystems, designed to fully capture a wide array of physics processes. A diagram of the detector is shown in Figure 4.1. The apparatus is 25m high, 44m in length, and weighs over 7000 tons [34]. The LHC beam pipes direct proton beams to an interaction point at the center of ATLAS, and the cylindrical detector design captures a complete 360° view of the *event*¹, tracking all particles that result from the collision.

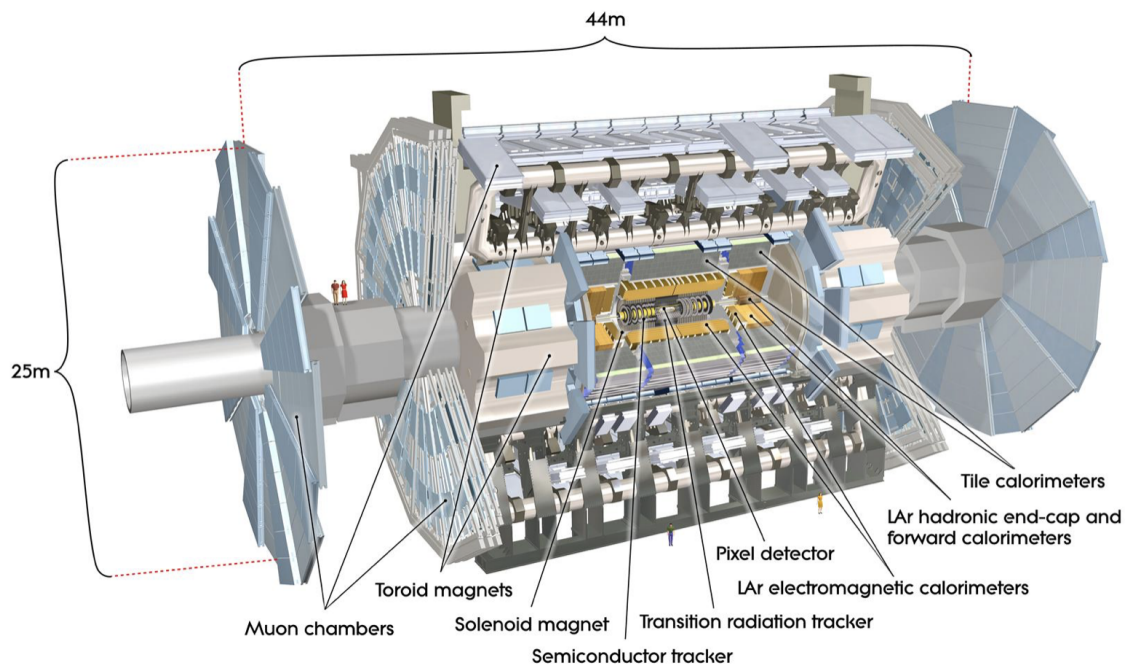


Figure 4.1: The ATLAS detector [34].

¹An ATLAS event is a snapshot of all the measurements associated to a given $p p$ collision

734 The main components of the ATLAS detector are the Inner Detector (ID) which provides high
 735 precision tracking of charged particles leaving the collision vertex, the calorimeter system which
 736 measures the energy of electromagnetic and hadronic objects, and the Muon Spectrometer (MS)
 737 which gives detailed information about muons that reach the outer radii of the detector. A summary
 738 of the resolution and angular coverage of each of these systems is presented in Table 4.1. Two
 739 magnet systems, a 2 T solenoid magnet surrounding the ID, and a 0.5-1.0 T toroid magnet system
 740 situated throughout the MS, produce magnetic fields which bend the trajectory of charged particles
 741 traversing the detector. In addition to the main detector components, dedicated forward detectors
 742 monitor beam conditions and instantaneous luminosity, and an online trigger system reduces the
 743 data rate to a manageable level for storage. Each of these components will be discussed in further
 744 detail in this chapter.

Detector component	Required resolution	η coverage	
		Measurement	Trigger
Tracking	$\sigma_{p_T}/p_T = 0.05\% p_T \oplus 1\%$	± 2.5	
EM calorimetry	$\sigma_E/E = 10\%/\sqrt{E} \oplus 0.7\%$	± 3.2	± 2.5
Hadronic calorimetry (jets)			
barrel and end-cap	$\sigma_E/E = 50\%/\sqrt{E} \oplus 3\%$	± 3.2	± 3.2
forward	$\sigma_E/E = 100\%/\sqrt{E} \oplus 10\%$	$3.1 < \eta < 4.9$	$3.1 < \eta < 4.9$
Muon spectrometer	$\sigma_{p_T}/p_T = 10\% \text{ at } p_T = 1 \text{ TeV}$	± 2.7	± 2.4

Table 4.1: General performance goals of the ATLAS detector [34].

745 4.1 Coordinate System and Geometry

746 The ATLAS detector employs a right hand cylindrical coordinate system. The z axis is aligned
 747 with the beam line, and the $x - y$ plane sits perpendicular to the beam line. The coordinate system
 748 origin is centered on the detector, such that the origin corresponds with the interaction point of the
 749 two colliding beams. The detector geometry is usually characterized by polar coordinates, where
 750 the azimuthal angle ϕ spans the $x - y$ plane. The polar angle θ represents the angle away from the
 751 beam line, or z axis. $\theta = 0$ aligns with the positive z axis, and $\phi = 0$ aligns with the positive x axis.

752 The polar coordinate θ is generally replaced by the Lorentz invariant quantity *rapidity* or y :

$$y = \frac{1}{2} \ln\left(\frac{E + p_z}{E - p_z}\right). \quad (4.1)$$

753 This substitution is advantageous because objects in the detector are traveling at highly rela-
754 tivistic speeds. The relativistic speed also means that the masses of the particles are generally small
755 compared to their total energy. In the limit of zero mass, the rapidity y reduces to the pseudorapid-
756 ity η , which can be calculated directly from the polar angle θ :

$$\eta = -\ln\left(\frac{\theta}{2}\right). \quad (4.2)$$

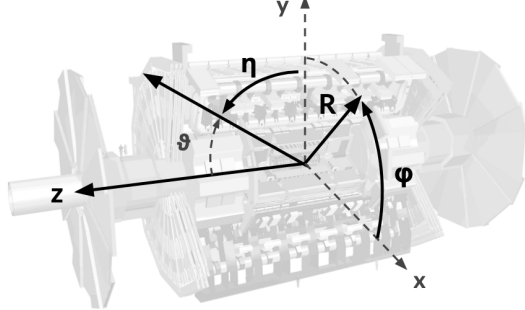
757 The distance between physics objects in the detector is generally expressed in terms of the solid
758 angle between them ΔR :

$$\Delta R = \sqrt{\Delta\phi^2 + \Delta\eta^2} \quad (4.3)$$

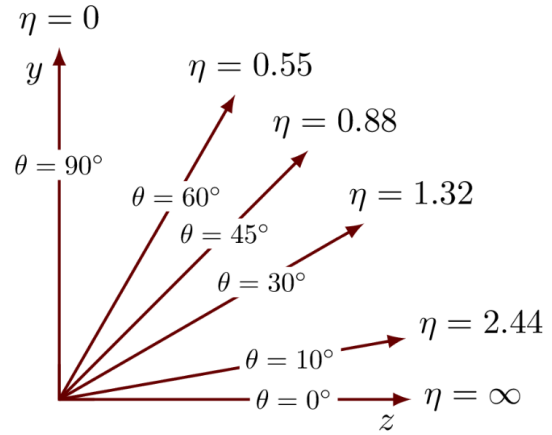
759 Figure 4.2a depicts the orientation of the coordinate system with respect to the ATLAS detector,
760 while Figure 4.2b illustrates the relationship between θ , η , and the beamline axis z . Direct or “head
761 on” proton-proton collisions are more likely to result in objects whose momentum is directed
762 along transverse plane (low $|\eta|$); glancing proton-proton collisions are more likely to result in
763 objects whose momentum is directed along the z -axis (high $|\eta|$). Due to the difference in the
764 nature of these collisions, as well as the cylindrical design of the ATLAS detector, the detector
765 is divided into regions of low and high $|\eta|$. Each subsystem has a “central” or “barrel” region
766 covering low $|\eta|$, while the “forward” or “end-cap” regions cover the area up to $|\eta| = 4.9$. Each of
767 the three main ATLAS subsystems will be discussed in the following sections.

768 **4.2 Inner Detector**

769 The Inner Detector (ID) is the ATLAS subsystem closest to the interaction point. The primary
770 purpose of the ID is to determine the charge, momentum, and trajectory of charged particles pass-



(a) The ATLAS geometry



(b) Relationship between η and θ

Figure 4.2: ATLAS coordinate system and geometry

771 ing through the detector. With this information the ID is also able to precisely determine interaction
 772 vertices.

773 The ID is composed of three sub-detectors; the Pixel Detector, the Semiconductor Tracker
 774 (SCT) and the Transition Radiation Tracker (TRT) [34]. Figure 4.3 shows the location of these
 775 three subsystems with respect to each other and the interaction point.

776 4.2.1 Pixel Detector

777 The pixel detector is the first detector encountered by particles produced in LHC collisions.
 778 The original pixel detector consists of 3 barrel layers of silicon pixels, positioned at 5 cm, 9 cm
 779 and 12 cm from the beamline. There are also 3 disks on each end-cap positioned 50 - 65 cm
 780 from the interaction point, providing full coverage for $|\eta| < 2.2$. Figure 4.4 illustrates the end-cap
 781 geometry for the ID. The layers are comprised of silicon pixels each measuring $50 \times 400 \mu\text{m}^2$,
 782 with 140 million pixels in total. The pixels are organized into modules, which each contain a set
 783 of radiation hard readout electronics chips. In 2014, the Insertable B-layer (IBL) was installed,
 784 creating a new innermost layer of the pixel detector sitting just 3.3 cm from the beamline. The
 785 pixels of the IBL measure $50 \mu\text{m}$ by $250 \mu\text{m}$, and cover a pseudo-rapidity range up to $|\eta| < 3$.
 786 The IBL upgrade enhances the pixel detector's ability to reconstruct secondary vertices associated

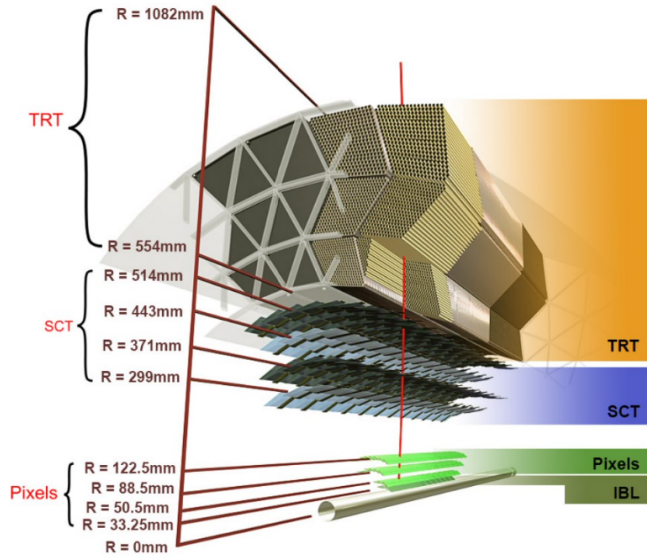


Figure 4.3: A 3D visualization of the structure of the ID in the barrel region [35]

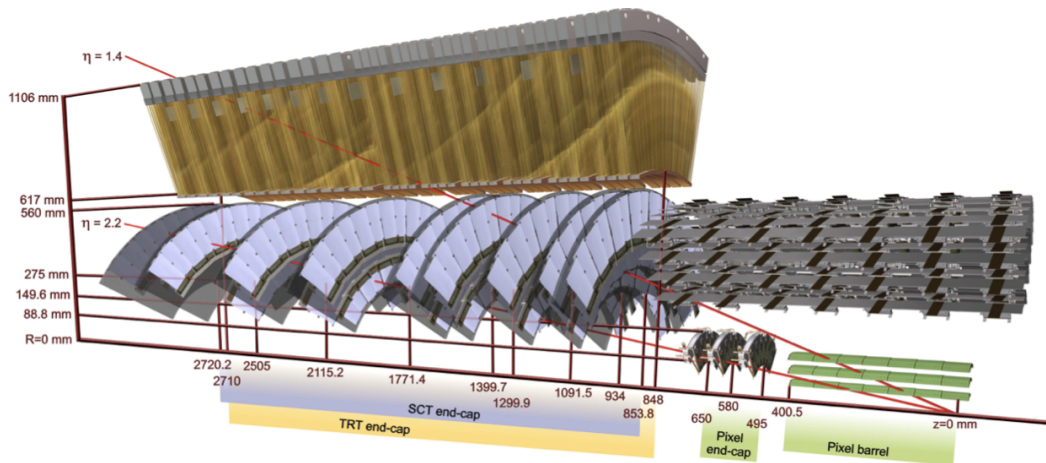


Figure 4.4: A 3D visualization of the structure of the ID end-caps [34]. The paths of two charged particles ($\eta = 1.4$ and 2.2) are illustrated.

787 with short-lived particles such as the b-quark. The improved vertex identification also helped
788 compensate for increasing pile-up in Run 2.

789 **4.2.2 Semiconductor Tracker**

790 The SCT provides at least 4 additional measurements of each charged particle. It employs the
791 same silicon technology as the Pixel Detector, but utilizes larger silicon strips which measure 80
792 μm by 12.4 cm. The SCT is composed of 4 barrel layers, located between 30 cm and 52 cm from
793 the beamline, and 9 end-cap layers on each side. The SCT can distinguish tracks that are separated
794 by at least 200 μm .

795 **4.2.3 Transition Radiation Tracker**

796 The TRT provides an additional 36 hits per particle track. The detector relies on gas filled
797 straw tubes, a technology which is intrinsically radiation hard. The straws which are each 4 mm in
798 diameter and up to 150 cm in length and filled with xenon gas. The detector is composed of about
799 50,000 barrel region straws and 640,000 end-cap straws, comprising 420,000 electronic readout
800 channels. Each channel provides a drift time measurement with a spatial resolution of 170 μm per
801 straw. As charged particles pass through the many layers of the detector, transition radiation is
802 emitted. The use of two different drift time thresholds allows the detector to distinguish between
803 tracking hits and transition radiation hits.

804 **4.3 Calorimeters**

805 The ATLAS calorimeter system is responsible for measuring the energy of electromagnetically
806 interacting and hadronically interacting particles passing through the detector. The calorimeters are
807 located just outside the central solenoid magnet, which encloses the inner detectors. The calorime-
808 ters also stop most known particles, which the exception of muons and neutrinos, preventing them
809 from traveling to the outermost layers of the detector. The ATLAS calorimetry system is composed
810 of two subsystems - the Liquid Argon (LAr) calorimeter for electromagnetic calorimetry and the

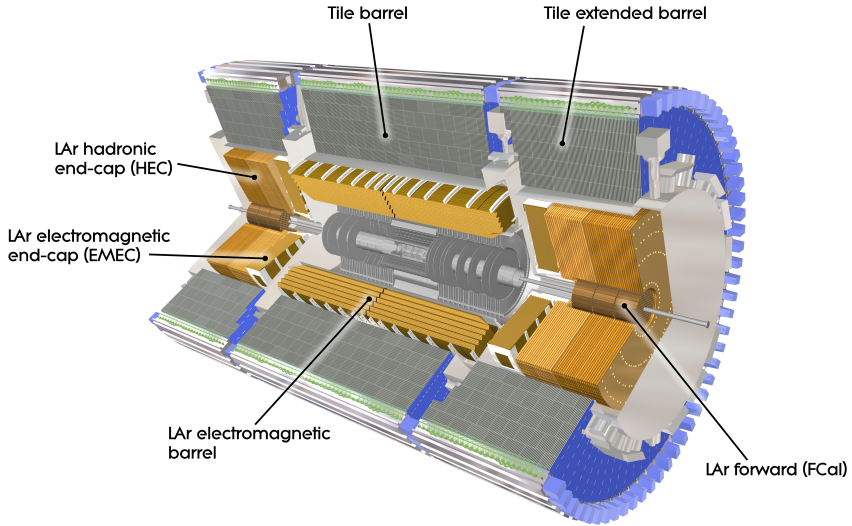


Figure 4.5: ATLAS calorimetry system [36]

811 Tile calorimeter for hadronic calorimetry. The full calorimetry system is shown in Figure 4.5.

812 4.3.1 Liquid Argon Calorimeter

813 The LAr calorimeter is a sampling calorimeter designed to trigger on and measure the ener-
814 gies of electromagnetic (EM) particles, as well as hadronic particles in the high $|\eta|$ regions [37].

815 It is divided in several regions, as shown in Figure 4.5. For the region $|\eta| < 1.4$, the electro-
816 magnetic barrel (EMB) is responsible for EM calorimetry, and provides high resolution energy,
817 timing, and position measurements for electrons and photons passing through the detector. The
818 electromagnetic end-cap (EMEC) provides additional EM calorimetry up to $|\eta| < 3.2$. In the
819 region $1.4 < |\eta| < 3.2$, the hadronic end-cap (HEC) provides hadronic calorimetry. For hadronic
820 calorimetry in the region $|\eta| < 1.4$, corresponding to a detector radii > 2.2 m, the less expensive
821 tile calorimeter (discussed in the next section) is used instead. A forward calorimeter (FCAL)
822 extends the hadronic calorimetry coverage up to $3.1 < |\eta| < 4.9$.

823 The LAr calorimeter is composed of liquid argon sandwiched between layers of absorber mate-
824 rial and electrodes. Liquid argon is advantageous as a calorimeter active medium due to its natural
825 abundance and low cost, chemical stability, radiation tolerance, and linear response over a large

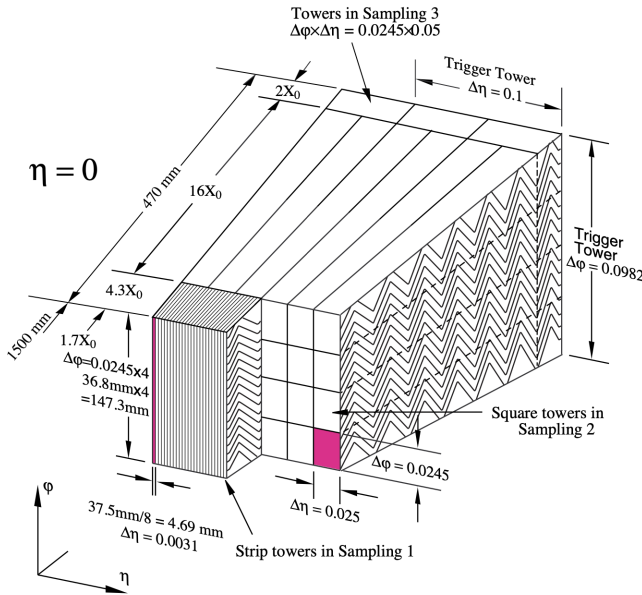


Figure 4.6: Diagram of a segment of the EMB, demonstrating the accordion plate arrangement and the cell segmentation pattern [37]. Three layers are illustrated, and the variation in the cell granularity between the front layer (Sampling Layer 1) and the back layer (Sampling Layer 3) is shown.

826 energy range [38]. The calorimeter is cooled to 87k by three cryostats: one barrel cryostat encom-
 827 passing the EMB, and two end-cap cryostats. The barrel cryostat also encloses the solenoid which
 828 produces the 2T magnetic field for the inner detector. Front-end electronics are housed outside the
 829 cryostats and are used to process, temporarily store, and transfer the calorimeter signals.

830 Electromagnetic Calorimeter

831 For the electromagnetic calorimeters, the layers of electrodes and absorber materials are ar-
 832 ranged in an accordion shape, as illustrated in Figure 4.6. The detector is divided into $\eta - \phi$ regions
 833 or *cells*, which are each read out independently. The The accordion shape ensures that each half
 834 barrel is continuous in the azimuthal angle, which is a key feature for ensuring consistent high
 835 resolution measurements. Liquid argon permeates the space between the lead absorber plates, and
 836 a multilayer copper-polymide readout board runs through the center of the liquid argon filled gap.

837 The detection principle for the LAr calorimeter is the current created by electrons which are

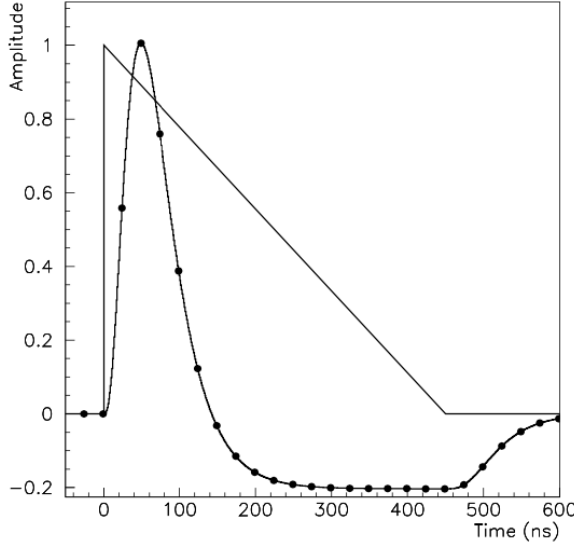


Figure 4.7: A LAr pulse as produced in the detector (triangle) and after shaping (curve) [37]

released when a charged particle ionizes the liquid argon. In the barrel region, the electrons are driven towards the center electrodes by a 2,000 V potential with a drift time of less than 450 ns [39]. In the end-caps the voltage varies as a function of the radius in order to maintain a flat response [37]. The amount of current produced by the ionized electrons is proportional to the energy of the particle creating the signal. Figure 4.7 shows the shape of the signal produced in the LAr calorimeter, before and after it undergoes shaping during the readout process. The shaping of the pulse enforces a positive peak and a negative tail, which ensures that subsequent pulses can be separated with the precision required for the 25 ns LHC bunch spacing.

Hadronic End-cap Calorimeter

The HEC sits radially beyond the EMEC. The copper absorber plates in the HEC are oriented perpendicular to the beamline, with LAr as the active medium. Each end-cap is divided into two independent wheels; the inner wheel uses 25 mm copper plates, while the outer wheel uses 50 mm plates as a cost saving measure. In each wheel, the 8.5 mm plate gap is crossed by three parallel electrodes, creating an effective drift distance of 1.8 mm. This gap is illustrated in Figure 4.8. Each wheel is divided into 32 wedge-shaped modules, each containing their own set of readout

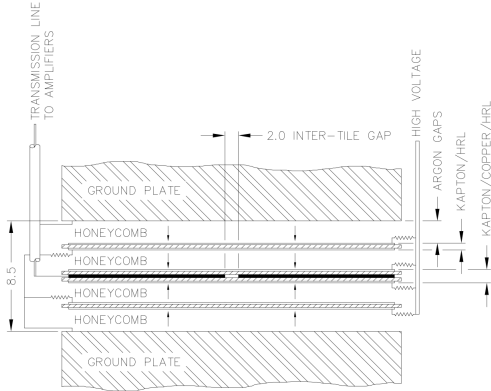


Figure 4.8: Readout gap structure in HEC [37]

853 electronics.

854 Forward Calorimeter

855 The forward range ($3.1 < |\eta| < 4.9$) is covered by the FCal, which provides both EM and
 856 hadronic calorimetry. It is composed of three active cylindrical modules; one EM module with
 857 copper absorber plates, and two hadronic modules with tungsten absorber plates [37]. The plates
 858 are oriented perpendicular to the beamline, and LAr is used as the active material throughout. The
 859 electrodes of the FCal consist of tubes that run parallel to the beam line, arranged in a honeycomb
 860 pattern. The resulting LAr gaps are as small as $250 \mu\text{m}$, which enables the FCal to handle the high
 861 particle flux in the forward region.

862 4.3.2 Tile Calorimeter

863 The Tile Calorimeter (TileCal) provides hadronic calorimetry in the region $|\eta| < 1.7$, and sur-
 864 rounds the LAr calorimeter. It is responsible for measurements of jet energy and jet substructure,
 865 and also plays an important role in electron isolation and triggering (including muons) [40]. Tile-
 866 Cal is composed of 3 sections, as shown in Figure 4.5; a barrel calorimeter sits directly outside the
 867 LAr EMB and provides coverage up to $|\eta| < 1.0$. Two extended barrel sections sit outside the LAr
 868 end-caps and cover the region $0.8 < |\eta| < 1.7$.

869 TileCal is a sampling calorimeter composed of steel and plastic scintillator plates as illustrated

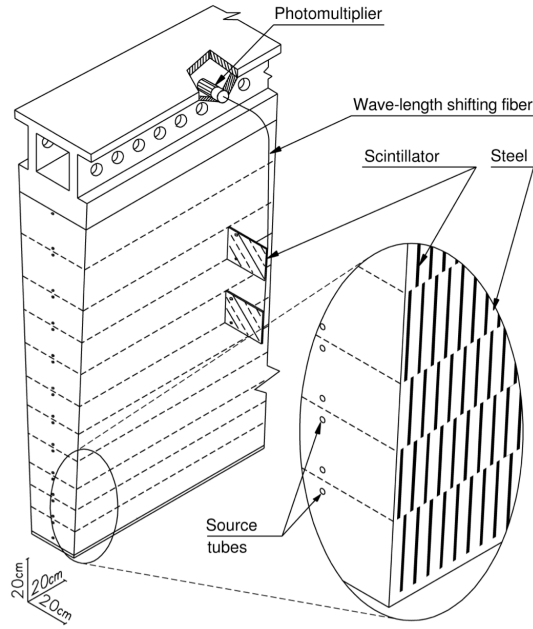


Figure 4.9: TileCal wedge module [40]

in Figure 4.9. A total of 460,000 scintillators are read out by wavelength-shifting fibers. The fibers are gathered to define cells and in turn read out by photomultiplier tubes, which amplify the scintillation light and convert it to an electrical signal. Each cell has an approximate granularity of $\Delta\eta \times \Delta\phi = 0.1 \times 0.1$. Each barrel is divided azimuthally into 64 independent modules, an example of which is show in Figure 4.9. The modules are each serviced by front-end electronic housed in a water-cooled drawer on the exterior of the module.

The detection principle of the TileCal is the production of light from hadronic particles interacting with the scintillating tiles. When a hadronic particle hits the steel plate, a shower of particles are produced. The interaction of the shower with the plastic scintillator produces photons, the number and intensity of which are proportional to the original particle's energy.

880

881 4.4 Muon Spectrometer

882 Unlike electrons, photons, and hadrons, muons interact minimally with the ATLAS calorimeters, and can pass through large amounts of detector material without stopping. The ATLAS Muon

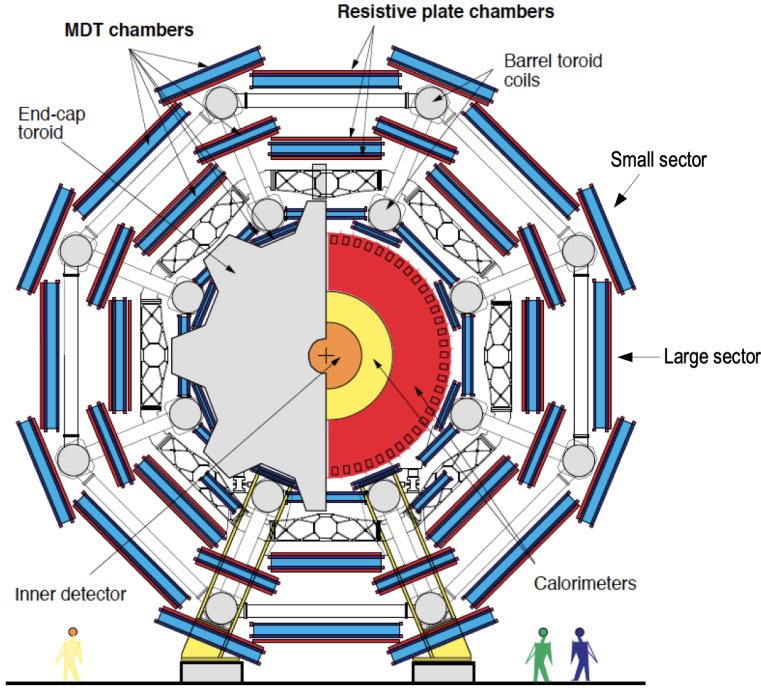


Figure 4.10: Cross section view of the muon spectrometer system [41]

884 Spectrometer (MS) provides additional tracking information to improve the identification and mea-
 885 surement of muons [41]. The MS comprises the outermost layers of the detector, and is interspersed
 886 with toroid magnets (discussed in Section 4.5), which provide a magnetic field of approximately
 887 0.5 T. The magnetic field bends the trajectory of the muons as they pass through the detector, and
 888 the degree of the bend is directly correlated with the muon momentum. The path of the muon is
 889 primarily measured by hits in three layers of Monitored Drift Tube (MDT) precision chambers,
 890 which cover the range $|\eta| < 2.7$. The barrel layout of the MS is shown in Figure 4.10.

891 Muon triggering is provided by three layers of Resistive Plate Chambers (RPC) in the barrel
 892 ($|\eta| < 1.05$), and 3 - 4 layers of Thin Gap Chambers (TGC) in the end-caps ($1.05 < |\eta| < 2.4$).
 893 RPCs and TGCs also provide muon track measurements in the non-bending coordinate (ϕ). RPCs
 894 are constructed from two parallel resistive plates separated by a 2mm gap filled with a sensitive
 895 gas mixture. This provides a total of six independent measurements for each muon track, with a
 896 spatial resolution of ~ 1 cm and a time resolution of ~ 1 ns. Time measurements from the RPCs
 897 are primarily associated to hits in the MDT precision chambers to determine the bunch crossing.

898 The time measurement is also used to reject cosmic muons, and to search for delayed signals.
899 TCGs provide triggering in the end-cap regions, and consist of parallel 30 μm wires suspended
900 in a sensitive gas mixture. TCGs provide high radiation tolerance and a fast response time, both
901 features that are necessary for handling the high flux of muons in the forward region.

902 Precision measurements of muon momentum and position are primarily achieved by MDTs.
903 The MDTs are constructed from 30 mm diameter tubes, permeated by a gas mixture of 93% Ar
904 and 7% CO₂ [42]. The average single-tube spatial resolution is 80 μm . Each chamber consists
905 of six drift tube layers, which together provide a muon track segment resolution of 35 μm . The
906 momentum of the muons can be calculated from the bend in the muon trajectory as they pass
907 through the 0.5T magnetic field provided by the toroids. For a $p_T = 1$ TeV track, the average
908 p_T resolution is 11%. In the inner most end-cap wheels, Cathode Strip Chambers (CSC) are
909 used instead of MDTs, covering the region $2.0 < |\eta| < 2.7$. CSCs are multi-wire proportional
910 chambers, with a cathode strip readout. The CSCs have a spatial resolution in the range of 50 μm ,
911 and a maximum drift time of about 30 ns, which makes them superior for handling the high flux of
912 particles in the forward region.

913 4.5 Magnet System

914 The ATLAS magnet system consists of four sets of superconducting magnets: a barrel solenoid,
915 a barrel toroid, and two end-cap toroids [43]. The solenoid magnet produces a 2T magnetic field
916 responsible for bending the trajectories of charged particles as they pass through the inner detector.
917 The three toroid magnets provide a field of 0.5 - 1 T and curve the path of muons passing through
918 the muon spectrometer.

919 The inner solenoid magnet is composed of over 9 km of niobium-titanium superconductor
920 wires, which are embedded into strengthened pure aluminum strips. The solenoid is just 4.5 cm
921 thick, which minimizes interactions between the magnet material and particles passing through the
922 detector. It is housed in the LAr cryostat, as described in section 4.3.1, which further reduces the
923 amount of non-detector material required to support the solenoid. The return yoke of the magnet

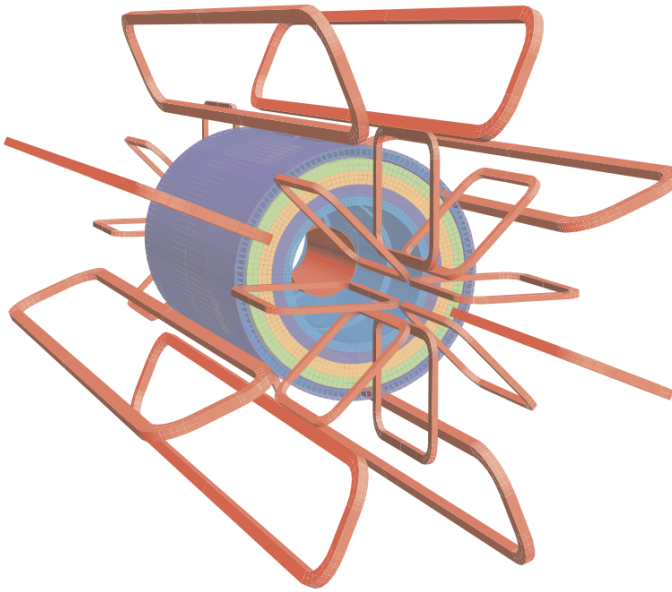


Figure 4.11: Layout of the barrel and end-cap toroid magnets [34]

924 is provided by the iron absorber of the TileCal.

925 The central ATLAS toroid magnet, providing the magnetic field for the barrel region of the
 926 MS, is the largest toroidal magnet ever constructed at 25.3 m in length [44]. The toroid is com-
 927 posed of eight individual coils, each housed in their own cryostat. The toroidal magnetic field is
 928 advantageous as the direction of the field is almost perpendicular to the path of the charged par-
 929 ticles. 56 km of aluminum stabilized niobium-titanium-copper superconductor wire compose the
 930 magnet. In each end-cap, eight smaller superconducting coils extend the toroidal magnetic field
 931 to particles leaving the detector in the forward direction [43]. Figure 4.11 shows the layout of the
 932 toroid magnets.

933 4.6 Forward Detectors

934 In addition to the inner detector, calorimeters, and muon spectrometer, three smaller detectors
 935 provide coverage in the very forward region. The innermost forward detector, at 17 m from the
 936 interaction point, is the **L**uminosity measurement using **C**erenkov **I**ntegrating **D**etector (LUCID).
 937 LUCID's primary purpose is to measure the relative online-luminosity for the ATLAS detector,

938 from inelastic $p - p$ scattering. The detector is composed of 20 aluminum Cerenkov tubes which
939 surround the beam pipe and face towards the interaction point.

940 The second forward detector is the Zero-Degree Calorimeter (ZDC), located 140 m from the
941 interaction point in both directions, at the point where the LHC beam-pipe divides into two separate
942 pipes. The ZDC's primary purpose is to detect forward neutrons from heavy ion collisions.

943 The third forward detector is the Absolute Luminosity For ATLAS (ALFA) system, located 240
944 m from the interaction point in both directions. ALFA determines luminosity by measuring elastic
945 scattering at small angles, from which luminosity can be calculated via the optical theorem. The
946 detector is built from scintillating fiber trackers. These are connected to the accelerator vacuum
947 via Roman pots, which allow the detector to come as close as 1mm to the beam without disrupting
948 the machine vacuum. The LUCID and ALFA detectors are crucial to determining the real-time
949 conditions of the beams and the total luminosity delivered to the ATLAS detector [34].

950 4.7 Trigger and Data Acquisition

951 The trigger and Data Acquisition systems (TDAQ) are responsible for selecting the most inter-
952 esting events to save for further downstream processing. Because of the high luminosities delivered
953 to the ATLAS detector, not all events recorded can be saved; the 40 MHz bunch crossing rate must
954 be reduced by 5 orders of magnitude to an event storage rate of ~ 1 kHz. The trigger system is
955 composed of three distinct levels: Level 1 (L1), Level 2 (L2) and the event filter [34]. Collectively
956 the L2 trigger and the event filter form the High Level Trigger (HLT).

957 The L1 trigger is implemented in the hardware of the ATLAS calorimeter and muon systems.
958 A block diagram of the L1 trigger is available in Figure 4.12. The primary modality of the L1 trig-
959 ger is to identify muons, electrons, photons, jets, and τ -leptons with high transverse momentum.
960 Particles with high transverse momentum are more likely to originate from direct, high energy
961 collisions, which are most likely to produce interesting physics processes. The L1 trigger also
962 identifies events with large missing transverse energy, which could be indicative of new physics.
963 The L1 muon trigger (L1Muon) relies on RPC and TGC trigger chambers in the barrel and end-

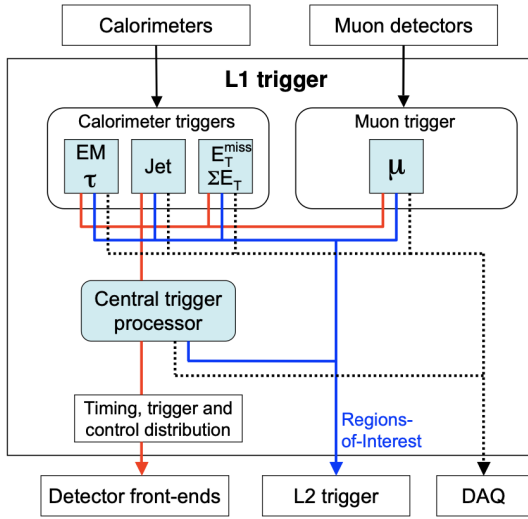


Figure 4.12: Block diagram of the L1 trigger process [34]. The overall L1 trigger decision is made by the CTP.

964 cap regions of the muon spectrometer. The L1 Calorimeter Trigger (L1Calo) uses reduced gran-
965 ularity information collected by all the calorimeter subsystems. Results from the L1Muon and
966 L1Calo triggers are combined by the Central Trigger Processor (CTP), which implements a trigger
967 ‘menu’, listing various combinations of trigger requirements. The maximum L1 acceptance rate
968 is 100 kHz, and the L1 trigger decision must reach the front-end electronics within 2.5 μ s of its
969 associated bunch-crossing.

970 The L1 trigger defines a Region-of-Interest (RoI) for each passing event. The ROI is repre-
971 sented by the η - ϕ detector region where interesting features were identified by the L1 selection
972 process. Information about the type of feature identified and the threshold which was exceeded to
973 trigger the L1 response is also recorded. The ROI data is sent to the L2 trigger, which uses all of
974 the available information within the ROI at full granularity and precision. The L2 trigger reduces
975 the event rate from 100 kHz to 3.5 kHz, with an average processing time of 40 ms. The final stage
976 of the HLT is the event filter, which reduces the event rate to 200 Hz (<1 kHz). The event filter uses
977 an offline analysis process to select fully rebuilt events which will be saved for further analysis. A
978 diagram of the full ATLAS TDAQ system is shown in Figure 4.13.

979 All levels of the ATLAS trigger system depend on specialized electronics. Each detector front-

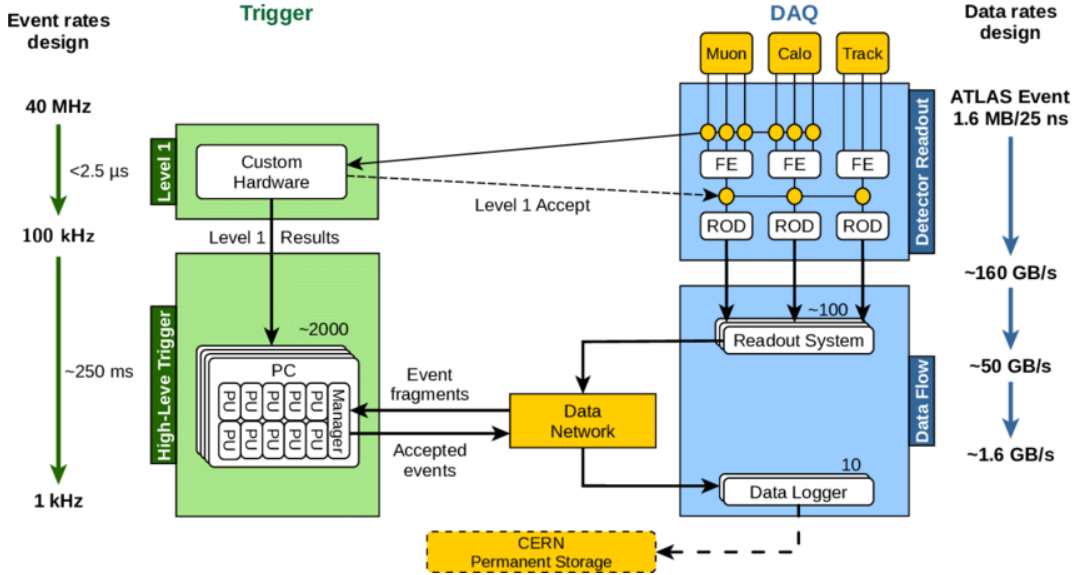


Figure 4.13: Block diagram of the trigger and data acquisition processes, including L1 and HLT processes [45].

980 end system has a specialized Readout Driver (ROD) which collects information from several front-
 981 end data streams at once. The ROD is composed of front-end analogue processing, a L1 buffer
 982 which retains the information long enough for the L1 trigger decision, and dedicated links which
 983 send the front-end L1 triggered data to Data Acquisition System (DAQ). Any digital signals are
 984 formatted as raw data before being transferred to the DAQ. The first stage of the DAQ temporarily
 985 stores the L1 data in local buffers. The ROI data is then requested by the L2 trigger, after which
 986 selected events are transferred to an event building system, before events passing the event filter
 987 are sent to the CERN computer center for permanent storage. The DAQ system not only allows
 988 for the readout of detector data, but is also responsible for the monitoring and configuration of
 989 the hardware and software components which make up the data readout system via the Detector
 990 Control System (DCS).

991 The DCS allows centralized control of all detector subsystems simultaneously. It continually
 992 monitors operational conditions, reports any abnormal behavior to the operator, and can perform
 993 both automatic and manual interventions. The DCS reports on real time detector conditions such
 994 as high or low voltage detector electronics, gas and cooling systems, magnetic field conditions,
 995 humidity and temperature. This information is continually monitored by experts in the ATLAS

996 control room, so that action can be taken immediately to correct any issues that arise. The DCS also
997 handles communication between detector systems, and other systems such as the LHC accelerator,
998 the ATLAS magnets, and CERN technical services [34].

1000 **Chapter 5: Particle Reconstruction and Identification**

1001 With a design luminosity of $1.0 \times 10^{34} \text{ cm}^{-2}\text{s}^{-1}$, and a peak Run-2 instantaneous luminosity of
 1002 $2.0 \times 10^{34} \text{ cm}^{-2}\text{s}^{-1}$, reconstructing and identifying the products of LHC $p p$ collisions is one of the
 1003 most complex tasks for each LHC experiment. The accurate reconstruction and identification of
 1004 *physics objects*¹ lays the ground work for all subsequent physics analyses, so it is also one of the
 1005 most fundamentally important tasks performed by an experiment.

1006 Reconstruction is the process of combining raw and uncalibrated hits across various subsystems
 1007 into unique objects. Two particular subsystems, the Inner Detector (ID) tracker and the calorime-
 1008 ters play particularly important roles and will be discussed in detail. Analysis of the properties of
 1009 the reconstructed objects identifies them as photon, electrons, muons, or jets. While photons, elec-
 1010 trons, and muons are fundamental particles, jets represent a collimated shower of many hadronic
 1011 particles, whose definition is more flexible. Jet reconstruction, clustering and track association are
 1012 all of particular import to jet identification, and to the later content of this thesis. Finally, recon-
 1013 struction also identifies *missing transverse energy* E_T^{miss} in events, which is a crucial variable for
 1014 BSM physics searches. Figure 5.1 shows how the physics objects listed here interact with various
 1015 systems in the ATLAS detector.

1016 **5.1 Inner Detector Tracks**

1017 As the inner most layer of the detector, the ID measures charged particles close to the interac-
 1018 tion point. The various hits of these charged particles throughout the ID are used to reconstruct
 1019 *tracks* which give the trajectories of charged particles [47]. Track reconstruction begins by clus-
 1020 tering hits in the Pixel and SCT detectors, and combining clusters from different radial layers of

¹A particle which has appeared in the ATLAS detector and whose properties have been estimated via the measurements left in various detector subsystems.

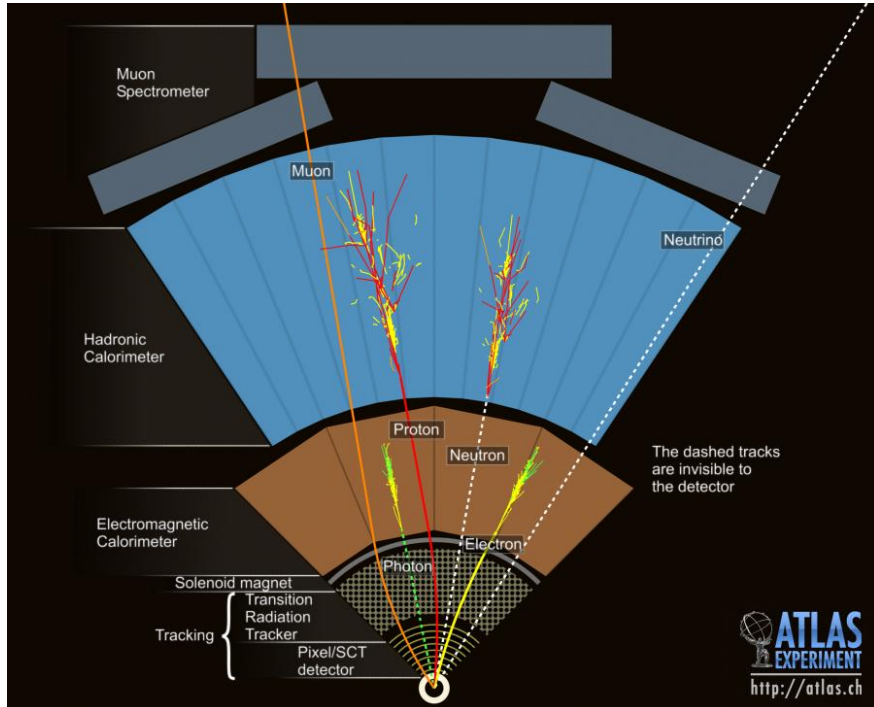


Figure 5.1: This graphic illustrates a slice of ATLAS detector barrel [46]. A photon, electron, and two jets (associated to the proton and neutron) are shown, illustrating each object's interaction with various ATLAS subsystems. The path of the charged particles is curved on account of the strong magnetic field produced by the solenoid and toroid magnets. A neutrino, generally representing the reconstruction of missing transverse energy, is also illustrated.

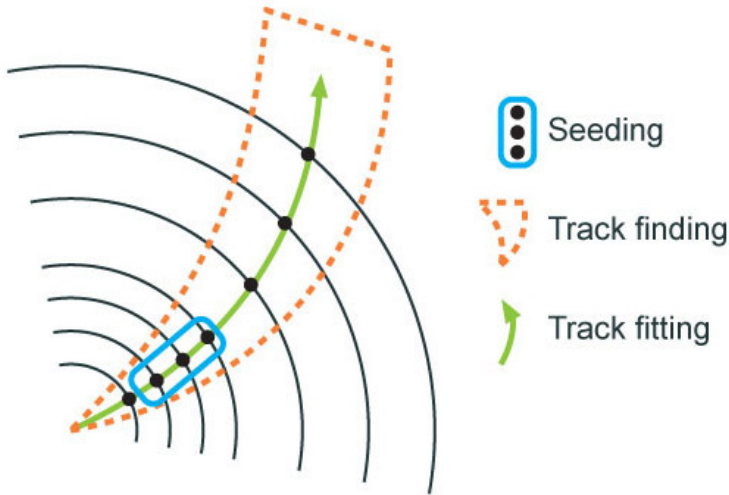


Figure 5.2: Track reconstruction seeding, finding and fitting illustration [47]

1021 these detectors. The multi-layer clusters form track *seeds*, which provide initial estimates of mea-
 1022 surements belonging to an individual track. The requirement of three points allows for a rough
 1023 estimate of the track p_T to be made by calculating the curvature of the track and accounting of the
 1024 magnetic field in the ID.

1025 Track seeds are subject to a variety of quality requirements, such as having a minimum esti-
 1026 mated p_T and passing interaction region compatibility criterion. If these requirements are satisfied,
 1027 the track seeds are passed to the track finding and fitting algorithms. The interplay of these three
 1028 track reconstruction steps is illustrated in Figure 5.2.

1029 5.2 Photons and Electrons

1030 Photons and electrons shower in the LAr calorimeter, and are identified by the energy deposits
 1031 they leave there. Energy deposits in a collection of nearby cells are termed *proto-clusters*, which
 1032 become the starting point for electron and photon reconstruction [48]. The clustering algorithm
 1033 begins when the energy deposit in a certain cell exceeds the noise threshold with a significance
 1034 of 4σ . The algorithm then collects neighboring cells which have an energy deposit exceeding the
 1035 noise threshold with a significance of 2σ , creating a *topo-cluster*². Next, these topo-clusters are

²A topological grouping of neighboring calorimeter cells based on their energy deposits

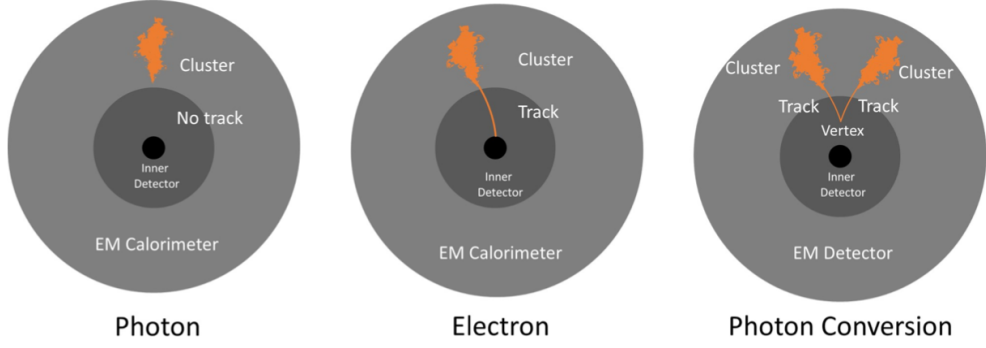


Figure 5.3: Three types of EM object candidates [49].

1036 matched to ID tracks, created as described in Section 5.1. The location of the topo-cluster defines
 1037 a region of interest (ROI) in the ID, where additional modified track reconstruction algorithms are
 1038 run in the case that no associated tracks are found. Any ID tracks associated to the topo-cluster
 1039 are retrofitted to allow for additional energy loss due to bremsstrahlung. A converted photon track
 1040 reconstruction algorithm is run to check for tracks coming from secondary vertices consistent with
 1041 converted photons. The secondary vertices are constructed from two oppositely charged tracks
 1042 consistent with a massless particle, or from one track without any hits in the innermost layer of the
 1043 ID.

1044 For electron identification, the EM cluster is required to match ID tracks that originate from
 1045 the primary vertex at the interaction point. For photon identification, the EM cluster can either be
 1046 matched to tracks coming from a secondary vertex (converted photon), or matched to no tracks
 1047 (unconverted photon). Figure 5.3 illustrates these three cases for EM object identification.

1048 *Superclusters* are built separately for photons and electrons, based on the combined topo-cluster
 1049 and ID track information. First, the EM topo-clusters are tested to see if they meet the minimum
 1050 requirements to become electron or photon seed clusters. For electrons, the cluster must have a
 1051 minimum E_T of 1 GeV, and must be matched to a track with at least 4 hits in the silicon tracking
 1052 detectors. For photons, the cluster must have an E_T greater than 1.5 GeV. If the seed cluster require-
 1053 ments are met, the algorithm searches for satellite clusters, which can arise from bremsstrahlung
 1054 radiation. If the satellite clusters pass the positional, energy and tracking requirements to be asso-

1055 ciated with the proto-cluster, they are combined into a supercluster.

1056 Electron and photon objects are identified from the superclusters after the energy calibration
1057 is applied, which accounts for the energy resolution of each subdetector measurement. Because
1058 photon and electron superclusters are built independently, some clusters can produce both a photon
1059 and an electron. In this case an ambiguity resolution procedure is applied to determine if the
1060 supercluster can be easily identified as only a photon (no tracks present) or only an electron (good
1061 tracks pointing to the primary vertex). In some cases, the identity of the cluster is still ambiguous,
1062 in which case both a photon and electron object are created for analysis and flagged as ambiguous.
1063 Energy, shower shape, and other analysis variables are calculated from the supercluster and saved
1064 with the electron or photon object.

1065 5.3 Muons

1066 Muons are identified through the tracks and energy deposits they leave in the ID, calorimeters,
1067 and Muon Spectrometer (MS). Muons experience minimum ionizing loss, meaning they do not
1068 deposit much of their energy in the calorimeters (recall Figure 5.1), and therefore reach the outer
1069 regions of the detector where the MS is housed. Muon identification begins in the Muon Drift
1070 Tube chambers by performing a straight line fit between the hits found in each layer, creating
1071 *segments*. Segments in the middle layers are then used as seeds for the track building algorithm,
1072 which searches for compatible combinations of segments based on their relative positions and
1073 angles [50]. A χ^2 fit is performed on each track candidate. Based on the χ^2 criteria, hits are
1074 removed or added such that the track contains as many hits as possible while satisfying the fit
1075 criteria.

1076 The MS track candidates are combined with track information from the ID and calorimeters
1077 according to various algorithms based on the information available from each subdetector. Four
1078 different types of muons arise from the various reconstruction algorithms:

- 1079 • Combined muon: a muon track identified through independent track reconstruction in the
1080 ID and MS, where the combined track is formed using a global refit that uses hit information

1081 from both detectors. Most muons are constructed through an outside-in procedure, in which
1082 a muon track candidate is identified in the MS and then an associated track is found in the ID.
1083 A complementary inside-out procedure is also implemented and identifies additional muons.

- 1084 • Segment-tagged muon: an ID track is identified as a muon if when extrapolated out to the
1085 MS (following the inside-out global fit procedure) it is matched to at least one local MS
1086 segment.
- 1087 • Calorimeter-tagged muon: an ID track is identified as a muon if it is matched to a calorimeter
1088 energy deposit that is compatible with a minimum-ionizing particle. This muon identifica-
1089 tion has the lowest purity, but it used in regions where the MS has only partial coverage due
1090 to cabling and service access routes.
- 1091 • Extrapolated muons: the muon is reconstruction only from the MS track and a requirement
1092 on compatibility with the primary interaction point. The muon track is required to cross at
1093 least two layers of the MS, and three layers in the forward region. These muons are mainly
1094 used to extend muon acceptance into the region $2.5 < |\eta| < 2.7$ where ID track information
1095 is not available.

1096 Figure 5.4 illustrates the four types of muon reconstruction. Overlap between reconstructed
1097 muons using ID tracks is resolved by giving preference to combined muons, then segment tagged
1098 muons, and finally calorimeter tagged muons. Overlap with extrapolated muons is resolved by
1099 giving preference to the muon with a better fit quality and higher number of tracks.

1100 All muon track candidates are required to pass a series of quality selections to be identified in
1101 the final muon collection. The primary qualities considered are the χ^2 goodness of fit for the global
1102 track, the difference in p_T measurement between the ID and MS tracks, and the ratio between the
1103 charge and momentum of the tracks. The quality requirements help reject hadrons, primarily from
1104 kaon and pion decays. Muons candidates consistent with cosmic rays are also rejected.

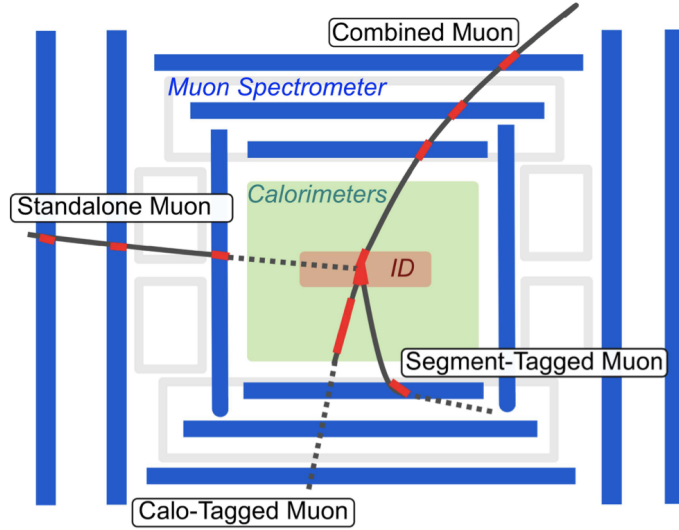


Figure 5.4: The four types of muon track candidates [51]. The red bands indicate where detector measurements for each muon track candidate are made. The dashed lines indicate the path of the muon through detectors where no measurement is made. Standalone muon is another term for an extrapolated muon.

1105 5.4 Jets

1106 The protons accelerated in the LHC are composed of quarks and gluons, and thus their colli-
 1107 sions often result in the release of energetic quarks and gluons, collectively termed *partons*. The
 1108 energetic partons can radiate additional gluons, and these gluons can pair produce quarks in a pro-
 1109 cess called *fragmentation*. Fragmentation continues until the energy drops sufficiently that color
 1110 conservation plays a dominant role. At that point, additional quarks and gluons are produced from
 1111 vacuum to create neutral color states for the fragmented collection of partons. This process is
 1112 known as *hadronization* [52]. The hadronized partons compose a collimated stream of particles,
 1113 known as a *jet*, which is then observed in the detector. The full process that produces jets is known
 1114 as a *parton shower*, and is illustrated in Figure 5.5.

1115 Jets are identified by the energy deposits they leave in the calorimeter, which are then matched
 1116 to the tracks they leave in the ID. Jet reconstruction generally begins in the calorimeters, with
 1117 the identification of *topo-clusters*. Then jet reconstruction algorithms combine calorimeter infor-
 1118 mation with tracking information. There are a variety of jet collections depending on the exact

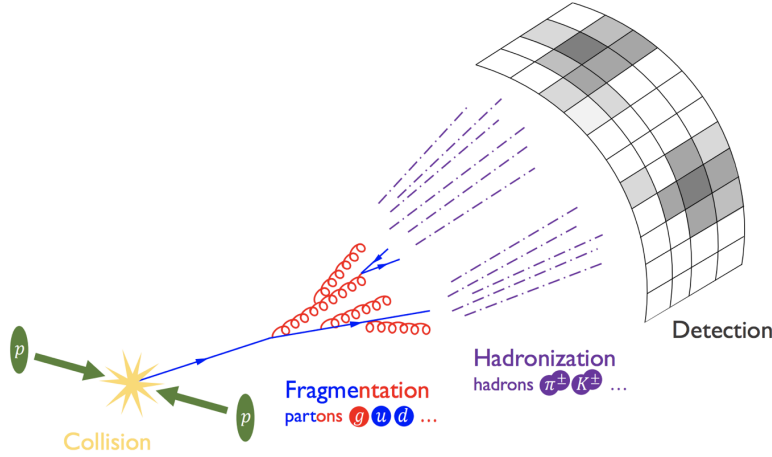


Figure 5.5: The fragmentation and hadronization processes undergone by a quark produced in a proton-proton collision [53].

1119 usage of calorimeter and tracking information in the reconstruction. Some common collections
 1120 include particle flow jets (PFlow), track calo-cluster jets (TCC), EM topo-cluster jets (EMTopo),
 1121 and unified flow object jets (UFO). Only particle flow jets will be discussed in greater detail due to
 1122 their importance in this analysis. The following sections discuss jet identification in the calorime-
 1123 ters, particle flow jet construction using the *anti- k_t algorithm*, jet clustering and jet substructure
 1124 characteristics.

1125 5.4.1 Calorimeter Clusters

1126 Jets are first identified by the energy deposits they leave in the calorimeters. As for photons
 1127 and electrons, the reconstruction of jets in ATLAS begins with the construction of topo-clusters,
 1128 which are topologically-grouped noise-suppressed clusters of calorimeter cells [54]. The topo-
 1129 cluster seed is a cell with an energy that exceeds the noise threshold for the cell with a significance
 1130 of at least 4σ . Any cells adjacent to the seed cell in three dimensions are added to the cluster if
 1131 they have an energy deposit of at least 2σ . This process is repeated, growing the cluster, until no
 1132 adjacent cells exceeding the energy deposit threshold remain. As a final step, all adjacent cells are
 1133 added to the topo-cluster, irrespective of their energy.

1134 The construction process for topo-clusters allows for the possibility that several independent

signatures are grouped into one topo-cluster. To correct for this, the topo-cluster is scanned for local maxima, defined by any cell with energy > 500 MeV, and no neighboring cells with greater energy. If more than one local maximum is identified, the topo-cluster is split among the corresponding energy peaks [55]. In the event that one cell neighbors two or more local maxima, the cell is assigned to the two highest-energy clusters that it neighbors. This means each cell is shared at most once, between at most two post-splitting topo-clusters.

Two measurements for the total energy of the topo-cluster are considered. The raw, or electromagnetic (EM), scale simply considers the sum of energy from all cells in the topo-cluster. The local cell weighting (LCW) scale first classifies clusters as electromagnetic or hadronic, and then applies appropriate corrections for hadronic interactions in the jet energy calculation [54]. The corrections are derived from Monte Carlo simulations, and account for the weaker response of ATLAS calorimeters to hadronic interactions (ATLAS calorimeters are *non-compensating*³), and hadronic energy losses due to interactions with dead material [55].

5.4.2 Particle Flow Algorithm

The calorimeters provide excellent jet energy resolution for high energy jets. However, the granularity of the hadronic calorimeter is restricted to 0.1×0.1 in $\eta \times \phi$. Combining the information from the calorimeter with tracking information provides superior angular resolution and energy resolution. The particle flow (PFlow) algorithm is one of a handful of algorithms which can perform this task.

An overview of the process is given in Figure 5.6. Tracks from the ID which are selected for the PFlow algorithm are required to have at least 9 hits in the silicon detector, and missing pixel hits in places where a hit would be expected. Additionally, the tracks have $p_T > 0.5$ GeV, and $|\eta| < 2.5$. The algorithm then attempts to match these tracks to EM scale calorimeter topo-clusters. This matching is performed using the distance metric

³The response of ATLAS calorimeters is different for EM showers and hadronic showers, since the calorimeter response to hadronic showers is energy dependent

$$\Delta R' = \sqrt{(\frac{\Delta\phi}{\sigma_\phi})^2 + (\frac{\Delta\eta}{\sigma_\eta})^2} \quad (5.1)$$

1159 where σ_η and σ_ϕ represent the angular widths of the topo-clusters, and $\Delta\eta$ and $\Delta\phi$ represent
 1160 the distance between the track (extrapolated to the second layer of the EM calorimeter) and the
 1161 barycenter of the topo-cluster [56]. The topo-cluster closest to the track as measured by $\Delta R'$ is
 1162 considered matched to the track. If no topo-cluster is found within the cone size of $\Delta R' = 1.64$, it
 1163 is assumed that particle which left the track did not form a topo-cluster in the calorimeter.

1164 The PFlow algorithm predicts the expected single topo-cluster energy for a given track, based
 1165 on the track momentum and topo-cluster position. This value is then compared to the observed
 1166 energy of the topo-cluster, and the probability that the particle energy was deposited in more than
 1167 one topo-cluster is evaluated. If necessary, the algorithm adds more topo-clusters to the track/topo-
 1168 cluster system, in order to account of the full shower energy of the track particle.

1169 To reduce the impact of double counting the energy of a given particle by including both its
 1170 tracker and calorimeter energy measurements, the calorimeter energy measurements associated to a
 1171 given track are subtracted from the total calorimeter measurement. If the expected energy deposited
 1172 by the particle exceeds the topo-cluster energy, the full topo-cluster is removed. If the expected
 1173 energy is less than the EM scale energy of all the considered topo-clusters, topo-cluster cells are
 1174 removed one by one, until the full expected energy deposit of the particle has been removed from
 1175 the calorimeter information. The resulting set of tracks and topo-clusters represent the event with
 1176 no double-counting of energy between subdetectors [56]. This information is passed to the jet-
 1177 finding algorithm.

1178 5.4.3 Jet Clustering

1179 When a parton decays in the detector, its energy deposits often result in multiple calorimeter
 1180 clusters. For physics purposes, it is useful to combine clusters that likely resulted from an individ-
 1181 ual parton decay, in order to reconstruct the parton. The process of grouping topo-clusters which
 1182 were produced by the same parton decay is *jet clustering*.

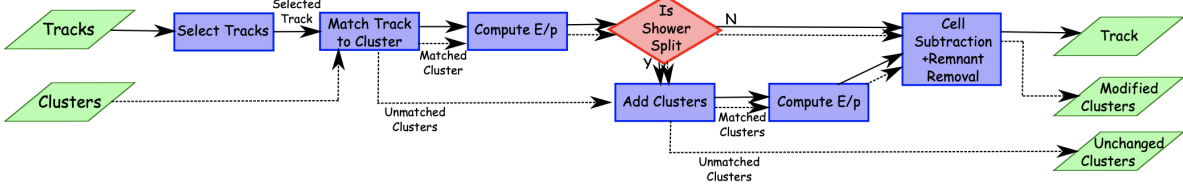


Figure 5.6: A flow chart illustrating the particle flow algorithm progression [56]. The solid lines indicate the progression of tracks through the algorithm, while the dotted lines indicate the progression of clusters. The process begins with track selection and continues until the energy associated with the tracks has been removed from the calorimeter. At the end charged particle tracks, unmodified topo-clusters, and the remnants of topo-clusters which have had part of their energy removed remain.

1183 The anti- k_t algorithm [57] as provided by the FastJet library [58] is most commonly used for
 1184 jet clustering in the ATLAS experiment, with varying reconstruction radius settings. The anti-
 1185 k_t algorithm is based on sequential recombination algorithms [59]. A sequential recombination
 1186 considers the distance d_{ij} between objects i and j (particles or pseudojets), and the distance d_{iB}
 1187 between an object i and the beam line B . If d_{ij} between two objects is the smallest distance among
 1188 those considered, i and j are combined into a pseudojet. The process continues until the smallest
 1189 distance is d_{iB} at which point the object i is determined to be a jet and removed from the objects in
 1190 consideration. The procedure is repeated with the remaining objects until there are none remaining
 1191 [57].

1192 The anti- k_t algorithm adopts this procedure, but modifies the distance measurements d_{ij} and
 1193 d_{iB} to consider the transverse momentum k_t :

$$d_{ij} = \min(k_{ti}^{2p}, k_{tj}^{2p}) \frac{\Delta_{ij}^2}{R^2}, \quad (5.2a)$$

$$d_{iB} = k_{ti}^{2p}. \quad (5.2b)$$

1194 The addition of the term p allows adjustments to algorithm which govern the relative power of
 1195 the momentum versus the geometrical scale $\Delta_{i,j}$, which is defined as $\Delta_{i,j} = (y_i - y_j)^2 + (\phi_i - \phi_j)^2$
 1196 where y_i and ϕ_i are respectively the rapidity and azimuth of particle i [57]. The radius parameter

1197 R is chosen and determines the geometric cone size [59].

1198 In the case $p = 1$ the inclusive k_t algorithm [59] is recovered, which is a standard sequential
1199 combination jet clustering algorithm. In the case $p = 0$, the Cambridge/Aachen sequential combi-
1200 nation algorithm [60] is recovered. The case $p = -1$ gives rise to the anti- k_t algorithm. The impact
1201 of this choice means that the distance d_{ij} between many soft particles is larger than between soft
1202 and hard particles. Therefore, soft particles tend to cluster with hard ones before they cluster with
1203 other soft particles. They key feature of this behavior is that soft particles do not modify the shape
1204 of the jets. This leads to the creation of circular conical jets, a desirable feature which sequen-
1205 tial combination algorithms and cone algorithms struggle to achieve. Figure 5.7 compares anti- k_t
1206 jet formation with the inclusive k_t and Cambridge/Aachen algorithms mentioned here, as well as
1207 the SIScone algorithm [61], which checks for sets of stable cones compatible with the observed
1208 radiation.

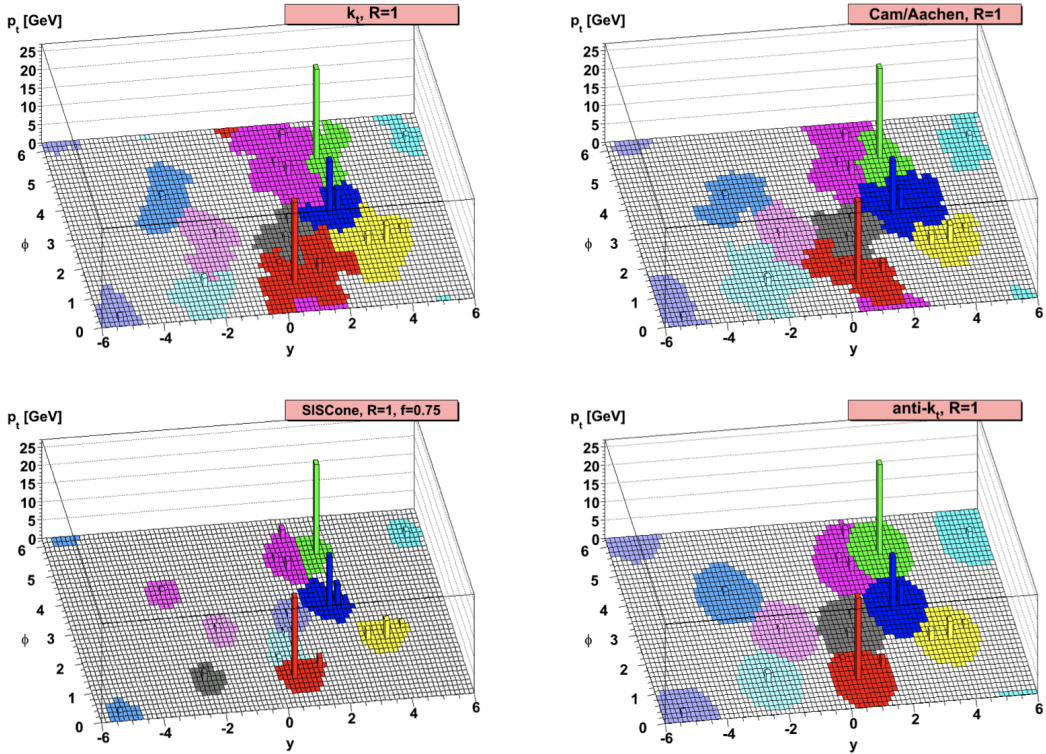


Figure 5.7: A comparison of jet clustering with four different jet algorithms. The anti- k_t algorithm is observed to create the most conical jets, where the shape of the jet is immune to the presence of soft radiation [57].

1209 Any useful jet clustering algorithm must satisfy the requirements of infrared safety and collinear
1210 (IRC) safety. Infrared safety implies that the resulting set of jets is unaltered by the presence of
1211 additional soft particles in the list of seed clusters. As explained above, the anti- k_t algorithm
1212 is naturally infrared safe. Collinear safety requires that the final set of jets is not impacted by
1213 collinear splitting of one of the jets. If the hardest particle p_1 is split into a collinear pair (p_{1a}, p_{1b})
1214 (as is common in the fragmentation process for a hard parton), the jet clustering algorithm must
1215 still recognize (p_{1a}, p_{1b}) as the hardest jet in the collision. If another softer particle p_2 with
1216 $p_{t,1a}, p_{t,1b} < p_{t,2} < p_{t,1}$ is instead considered the hardest particle in the event, a different final
1217 set of jets would be returned. Collinear safety is a requirement of perturbative QCD, to ensure
1218 non-divergent higher-order calculations [62]. The anti- k_t algorithm's tendency to cluster hard par-
1219 ticles first ensures its collinear safety. By satisfying the IRC safety requirement, anti- k_t jets can be
1220 calculated using perturbative QCD, which improves comparisons with theory.

1221 5.4.4 Ghost Track Association

1222 Once a collection of jets has been created, the jet objects can be studied at both the event-level
1223 and the jet-level. In the event-level picture, the momentum, energy, and geometric orientation of
1224 the jets within an event are considered. This yields important information about decay of any
1225 resonant heavy objects, the total energy in the event, and the distribution of energy amongst the
1226 jets. In the jet-level picture, the particle constituents of the jet are considered. The momentum,
1227 energy, and geometric orientation of the associated particle tracks provides a low-level picture of
1228 the jet, which can help determine if the properties of the jet are consistent with standard QCD, or
1229 if new physics processes might be represented within the low-level patterns. Jet-level analysis is
1230 also widely used in flavor tagging.

1231 For anti- k_t jets with a radius parameter $R = 0.4$, one way of studying the jet-level picture is
1232 through considering the ghost-associated tracks. Track association is the process of determining
1233 which tracks should be considered associated with a given jet. In the ghost association algorithm,
1234 the anti- k_t clustering algorithm is used for the collection of tracks and calorimeter clusters [63].

1235 However, the tracks are considered to have infinitesimal momentum (*ghosts*), so their addition to
1236 a jet object does not alter the four-momentum of the jet. This ensures the final jet collection is not
1237 altered by the presence of the ghost tracks in the reclustering, but information about the associated
1238 tracks for each reconstructed jet becomes available [64].

1239 Ghost tracks are of particular importance to this analysis, as a means of providing a low-level
1240 picture of the shape of $R = 0.4$ jets, and discriminating Standard Model QCD-like jets from dark
1241 QCD-like jets.

1242 5.5 Missing Transverse Energy

1243 A simple principle leveraged in ATLAS physics analyses is checking for conservation of mo-
1244 mentum among the products of any pp collisions. The initial state transverse momentum of any
1245 pp collision is always zero, so the transverse momentum of all final state particles should likewise
1246 be zero. The missing transverse energy, E_T^{miss} , is determined by the magnitude of the negative
1247 momentum vector sum of all final state objects resulting from the pp collision.

1248 Specifically, the objects considered in the E_T^{miss} calculation are photons, electrons, muons, jets,
1249 and soft terms. The first four items comprise the hard components of the E_T^{miss} calculation, and
1250 have been discussed previously in this chapter. The final item represents a collection of *soft terms*,
1251 comprising any detector signals not associated to hard detector objects. These can be based on
1252 unassociated tracks, or unassociated soft calorimeter clusters. Both are generally not used in the
1253 same calculation to avoid double counting of soft terms. In this analysis the calorimeter cluster
1254 soft terms are considered in the E_T^{miss} calculation.

1255 E_T^{miss} can arise due to non-interacting Standard Model objects such as a neutrinos, fake sources
1256 such as mis-reconstructed objects and dead detector regions, or in some theories, non-interacting
1257 BSM objects such as a dark matter candidate particles. To understand the amount of E_T^{miss} at-
1258 tributable to detector noise and mis-reconstruction, E_T^{miss} is studied in $Z \rightarrow \mu\mu$ where little real
1259 E_T^{miss} is expected [65]. As Figure 5.8 illustrates, the resolution of E_T^{miss} generally decreases as
1260 E_T^{miss} increases, due to detector resolution effects. As E_T^{miss} is an important quantity for most dark

¹²⁶¹ QCD analyses, limitations in the accuracy of the E_T^{miss} calculation must be considered.

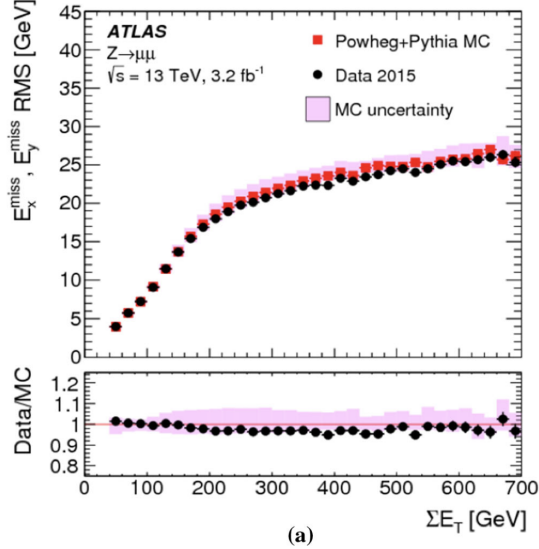


Figure 5.8: A comparison of MC simulation and data for $Z \rightarrow \mu\mu$ events where real $E_T^{\text{miss}} = 0$ [65]. The resolution of the missing energy in the transverse ($x - y$) plane is observed to increase with increasing total $\sum E_T$.

1262

Part III

1263

Search

1264

1265

Chapter 6: Monte Carlo and Data

1266 The search for semi-visible jets via s-channel production presented in the following chapters is
1267 performed with 139 fb^{-1} of proton-proton collision data collected by the ATLAS detector during
1268 Run 2 (2015 - 2018). The full Run-2 dataset is used for the final interpretation. Monte Carlo
1269 (MC) simulations of background processes and the semi-visible jet signal process are used in the
1270 development of the analysis strategy, and in the final interpretation to set limits on the observed
1271 cross-section of the signal model. This chapter will provide details about the full Run-2 dataset,
1272 and the background MC simulations, and the signal MC simulations used in this search.

1273 **6.1 Data**

1274 The 139 fb^{-1} of proton-proton collision data is selected according to the *good runs list* (GRL),
1275 which identify runs with good detector conditions that are suitable for physics evaluation. Events
1276 are further selected to pass a single-jet trigger selection, where events are required to have a jet at
1277 trigger-level with a p_T that exceeds a certain value. The lowest p_T unprescaled single jet trigger
1278 threshold for each period is as follows:

- 1279 • 2015: $p_T \geq 360 \text{ GeV}$
- 1280 • 2016 & 2017: $p_T \geq 380 \text{ GeV}$
- 1281 • 2017: $p_T \geq 380 \text{ GeV}$
- 1282 • 2017 & 2018: $p_T \geq 420 \text{ GeV}$

1283 A post-trigger selection of jet $p_T > 450 \text{ GeV}$ ensures all these triggers are fully within their
1284 efficiency plateaus. The jet collection used is anti- k_t EM particle flow jets with a radius parameter
1285 of $R = 0.4$, also referred to as small-R jets.

1286 Due to the variance in visible and invisible momenta due to the R_{inv} parameter of the signal
1287 model, many signals also have significant E_T^{miss} . The use of a E_T^{miss} trigger to select events was
1288 considered, and the single jet approach described here was found to preserve more signal events
1289 across the grid, particularly in the high resonance mass and low R_{inv} region of phase space. These
1290 studies are documented in Appendix A.

1291 The data are subject to a blinding strategy throughout the analysis design so as to mitigate
1292 analyzer-induced bias. Blinded and unblinded region definitions are described further in Sec-
1293 tion 8.1.

1294 6.2 Simulation

1295 Simulated events are generated with a variety of Monte Carlo (MC) generator processes that
1296 run in stages. The pp hard scatter physics process is simulated, and the final state particles are
1297 subsequently showered and decayed. This full description of the event is then propagated through
1298 a detailed detector simulation based on GEANT4 [66]. The MC simulation is weighted to match
1299 the distribution of the average number of interactions per bunch crossing μ observed in collision
1300 data.

1301 All simulated samples included in this analysis were produced with three different campaigns:
1302 `mc20a` corresponds to 2015-2016 data-taking conditions, `mc20d` to 2017, and `mc20e` to 2018.
1303 These three campaigns are weighted to the integrated luminosities of their respective data-taking
1304 periods and combined to produce simulation for the entire Run 2 dataset. Simulated events are
1305 reconstructed with the same algorithms run on collision data.

1306 6.2.1 Simulated Backgrounds

1307 Though the final background estimation is data-driven, background MC is studied for analysis
1308 optimization and machine learning tool development.

1309 Dijet QCD is the dominant background process. QCD is simulated with PYTHIA8 [67], and
1310 generated in approximate slices of p_T , to ensure high statistics across the momentum spectrum.

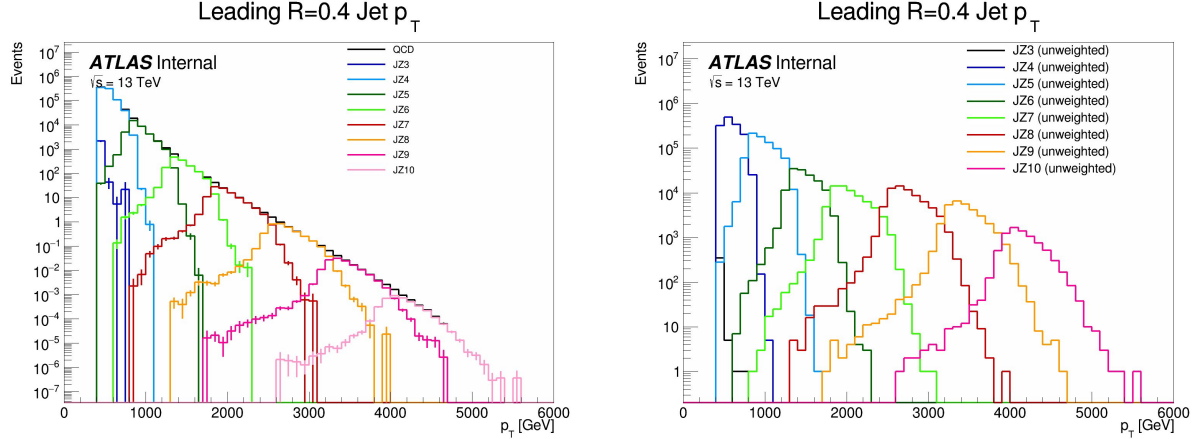


Figure 6.1: The transverse momentum slices of the QCD MC simulation, overlayed to show how they come together to create a smooth distribution (left) once weighted properly. The original unweighted distribution is shown on the right, illustrating the enhanced statistics for the high p_T range.

1311 The slices are then reweighted using MC generated event weights to create a physical distribution.

1312 Figure 6.1 illustrates the 8 momentum slices used in this analysis.

1313 Due to presence of E_T^{miss} in the SVJ signals, additional MC background processes are required
 1314 to create a full picture of the relevant background. The $Z \rightarrow vv$ process contributes to the back-
 1315 ground due to its high missing energy. Leptonic W/Z decays and W/Z+jets are also included as
 1316 they can contribute both additional missing energy and significant hadronic activity. Single top
 1317 and $t\bar{t}$ processes are also considered for their contribution to hadronic activity,. The background
 1318 composition in the selected region (discussed in Section 8.1) is 76% QCD, 12% W/Z+jets, 8%
 1319 top and $t\bar{t}$ processes, and 4% $Z \rightarrow vv$. Figure 6.2 illustrates the background composition for the
 1320 analysis.

1321 6.2.2 Signal Simulation

1322 The Hidden Valley signal model implementation is based on Ref [22]. The s-channel semi-
 1323 visible jet model is governed by a number of parameters. The mass of the mediator $m_{Z'}$ can be set,
 1324 together with the couplings of the Z' to the visible and dark quarks g_q and g_{q_D} . The dark sector
 1325 shower is governed by the number of dark colors N_{c_D} , the number of dark flavors N_{f_D} , and the

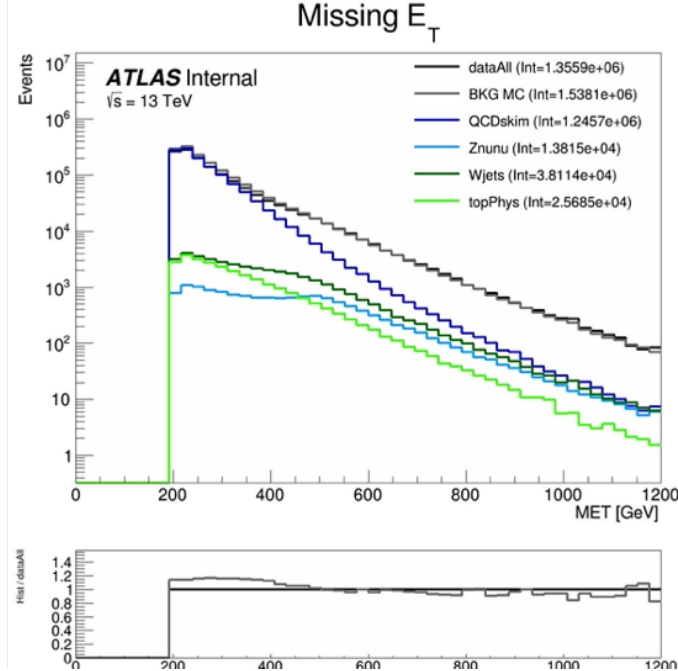


Figure 6.2: Background processes relevant to the SVJ signal. The agreement between the black line (data) and grey line (all MC processes combined) illustrates that this collection of background processes is sufficient to model the expected E_T^{miss} in the selected data events.

1326 dark sector confinement scale Λ_D . There is also the characteristic scale of the dark hadrons m_D ,
 1327 which determines the mass of the dark hadrons, which can be pseudoscalars m_{π_D} or vectors m_{ρ_D} .
 1328 Finally, the average fraction of invisible particles in the final state jet is dictated by R_{inv} .

1329 The chosen parameters for this model were carefully selected in collaboration with theorists to
 1330 be compatible with the new benchmarks established in the 2021 Snowmass process [21]. These pa-
 1331 rameters reflect extensive communication with the Snowmass, CMS, and theory teams. The signal
 1332 generation allows for up to two initial state radiation jets, and uses an MLM merging scheme [67]
 1333 to match jets to the original partons.

1334 The choices of fixed parameters for the Pythia8 HV model are summarized in Table 6.1. A
 1335 detailed discussion of these parameters and their implications on the dark shower topology can be
 1336 found in Ref. [21]. The mass choices for the dark quark and the dark hadrons are also summarized
 1337 in Table 6.2.

1338 Note that the number of dark flavors differs from the Snowmass recommendation of $N_{f_D} = 4$.
 1339 This change is minimal in impact because R_{inv} is set explicitly (rather than allowing it to arise

Parameter	Value
HiddenValley:Ngauge	3
HiddenValley:alphaOrder	1
HiddenValley:Lambda	10.0
HiddenValley:nFlav	2
HiddenValley:spinFv	0
HiddenValley:FSR	on
HiddenValley:fragment	on
HiddenValley:pTminFSR	1.1
HiddenValley:probVector	0.58

Table 6.1: Fixed parameters in the Pythia8 HV model

Parameter	Value [GeV]
m_{π_D}	17
m_{ρ_D}	31.77
m_{q_D}	10

Table 6.2: Values for m_{dark}

naturally from the HV theory), and allows us to remain more comparable with the CMS semi-visible jets analysis and the ATLAS t-channel analysis.

The mediator mass $m_{Z'}$ and the fraction of invisible particles in the final state R_{inv} vary, and are used to define the search grid. $m_{Z'}$ varies between 2.0 TeV and 5.0 TeV, while R_{inv} varies from 0.2 to 0.8. R_{inv} values of 0.2, 0.4, 0.6, and 0.8 are generated for each $m_{Z'}$ mass point. Table 6.3 illustrates the signal grid and the associated cross-section for each signal.

Samples are generated using MADGRAPH5 [68] version 2.9.9 interfaced to PYTHIA8.244P3 [67] for shower and hadronization with NNPDF23LO PDF [69] and the ATLAS A14 [70] to tune the underlying event data.

$m_{Z'}$ (GeV)	Cross section (fb)
2000	2.52e+2
2500	7.42e+1
3000	2.45e+1
3500	8.83e+0
4000	3.49e+0
5000	7.57e-1

Table 6.3: Mass points and cross sections of the SVJ search signal grid

Chapter 7: Machine Learning Tools

1351 7.1 Introduction

1352 The search for semi-visible jets presents an opportunity to use novel machine learning (ML)
 1353 tools to uncover patterns in the behavior of dark QCD. The subtlety of the shower differences be-
 1354 tween dark and SM QCD motivates a complex model that can accept high-dimensional low-level
 1355 inputs to best understand key differences between signal and background correlations. Addition-
 1356 ally, the large number of theory parameters which can be chosen arbitrarily and affect the shape of
 1357 the dark QCD shower motivate exploring a data-driven machine learning approach, which could
 1358 be sensitive to a wider variety of dark QCD behavior.

1359 To this end, two machine learning approaches are developed for this search, which are used
 1360 in tandem. The first is a supervised ML method where the ML algorithm is built to maximize
 1361 exclusion sensitivity to the specific generated SVJ signal models used in this analysis. Here, su-
 1362 pervised refers to the use of full and correct labels for all events considered during model training,
 1363 which necessitates training over simulated data. The second is a semi-supervised method, where
 1364 training of the model is data-driven and labels are only partially provided during training. The
 1365 semi-supervised ML algorithm broadens the discovery sensitivity of the search, and reduces the
 1366 dependence on the exact theory parameters chosen for signal model simulation.

1367 The two different ML algorithms used in this approach will be explained in the following
 1368 sections, along with their application in the SVJ analysis strategy.

1369 7.1.1 Particle Flow Network (Supervised)

1370 **Architecture Fundamentals**

1371 A Particle Flow Network (PFN) [71] architecture is selected for two reasons: *permutation in-*
1372 *variant input modeling* to best describe the events consisting of an unordered set of particles, and a
1373 *low-level input modeling* using tracks to take advantage of the available high-dimensional informa-
1374 tion to best exploit available correlations within the event. Permutation invariant input modeling
1375 is an architecture priority as ordered input modeling has been observed to bias the performance of
1376 low-level modeling tools as in [72]. Low-level input modeling is an architecture priority to capture
1377 the intricacies of dark QCD showers which may not express themselves in higher level variables,
1378 as explored in [22]. A comparison to a high-level *boosted decision tree* (BDT) is available in
1379 Appendix B.3.

1380 The PFN is used to model input events as an unordered set of tracks. Given the inherently
1381 unordered and variable-length nature of particles in an event, this choice of modeling as a *set*
1382 can enable the model to better learn the salient features of the dataset that enable a signal-to-
1383 background classification. Constructing the PFN involves the creation of new basis variables \oplus
1384 for each particle in the event. Permutation invariance is enforced by summing over the \oplus basis for
1385 every particle in the event to create a new permutation invariant latent space basis O . Finally the
1386 classifier F is a function of the sum over this new basis. The creation of the latent space basis O
1387 from M particles \vec{p} with d features each can be expressed as:

$$O(\{\vec{p}_1, \dots, \vec{p}_M\}) = \sum_{i=1}^M \Phi_i(\vec{p}_i) \quad (7.1)$$

1388 where $\Phi : \mathbb{R}^d \rightarrow \mathbb{R}^l$ is a per particle mapping, with l being the dimension of the new basis O .
1389 Figure 7.1 gives a graphical representation of the use of summation in the PFN over per-particle
1390 information to create a permutation-invariant event representation.

1391 Figure 7.2 provides an annotated diagram of the PFN architecture as used in this analysis.

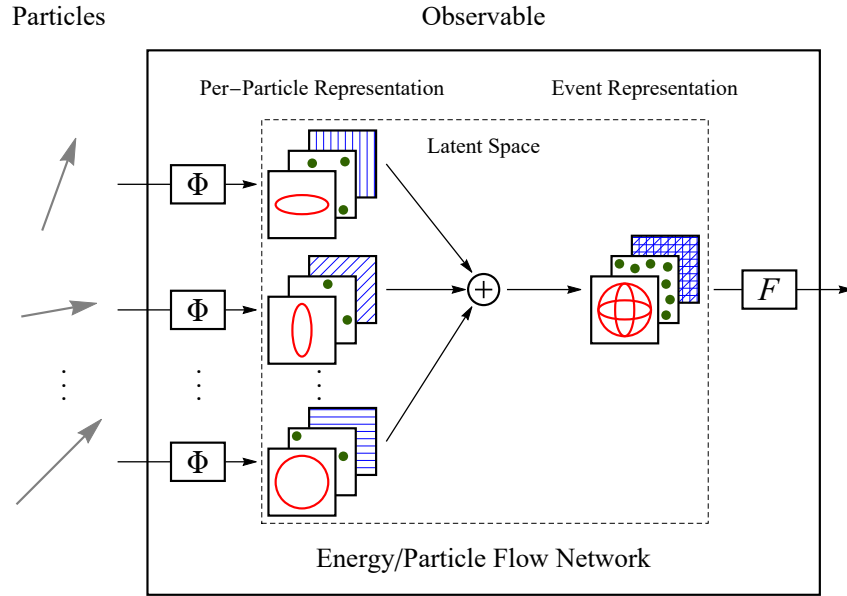


Figure 7.1: The Energy/Particle Flow Network concept, from Ref. [71].

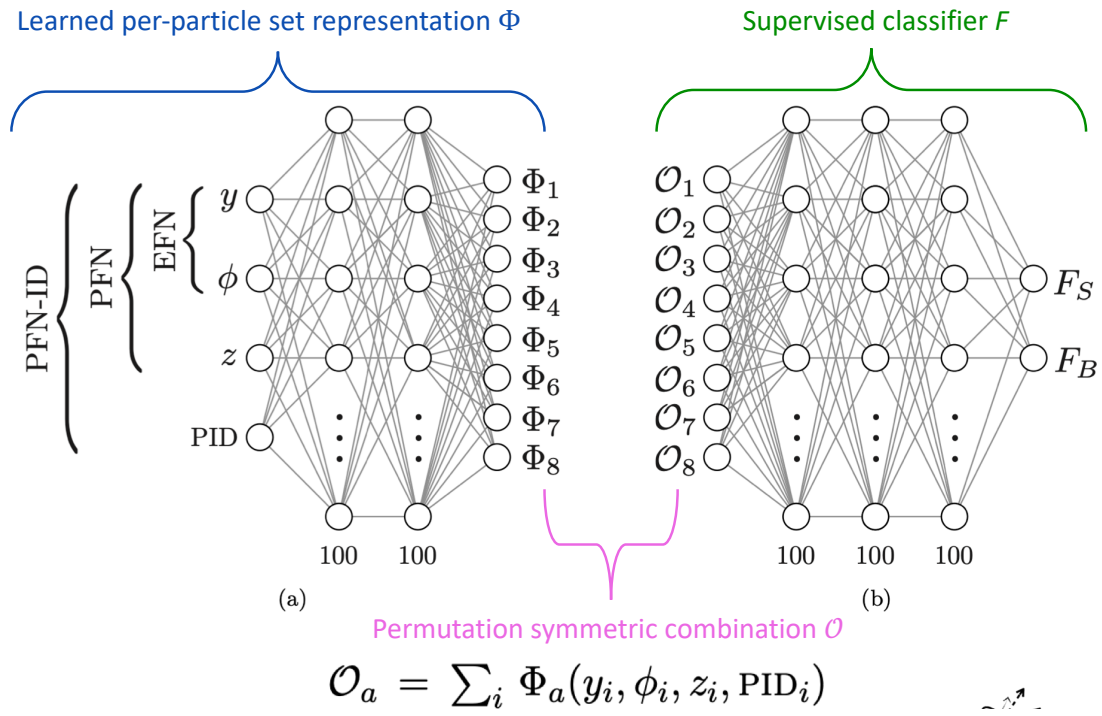


Figure 7.2: An annotated diagram of the PFN architecture. y and ϕ represent geometric information for the input particles, z represents energy information, and PID encompasses any other particle ID information in the input.

1392 **Input Modeling, Scaling, and Rotation**

1393 In this implementation, the particle input information comes from all tracks associated to the
1394 leading and subleading jets. The track association method is Ghost association, as discussed in
1395 Section 5.4.4. A single jet tagger strategy was also considered, but utilizing tracks from both
1396 leading jets creates a complete low-level picture of the event, which both focuses on the objects
1397 most likely to be associated to the decay of the dark quark (as will be justified in Chapter 8)
1398 and the relationship between those objects. If we consider the dijet topology of semi-visible jets
1399 as illustrated in Figure 7.3, the advantage of modeling both leading jets simultaneously becomes
1400 clear. In the semi-visible jet model presented in [22], E_T^{miss} in the event is expected to arise due to
1401 an imbalance in the number of visible tracks of the two jets associated to the dark quark decay.

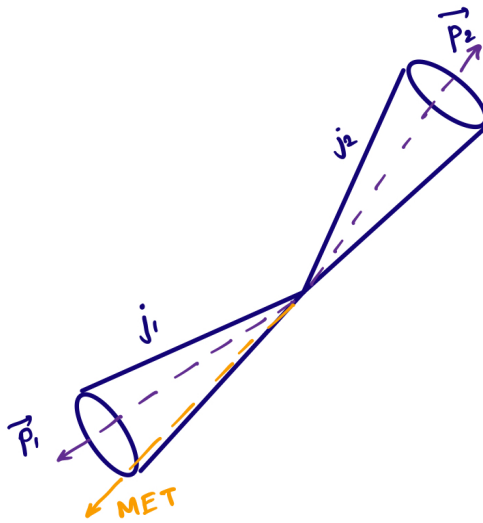


Figure 7.3: A illustration of the expected dijet behavior of semi-visible jets, where one jet is closely aligned with E_T^{miss} .

1402 Each track is described using six variables: the four-vector of the track (p_T , η , ϕ , E), and the
1403 track displacement parameters d_0 and z_0 , where d_0 measures displacement in the radial direction
1404 from the beamline and z_0 measures displacement along the beamline from the primary interac-
1405 tion point. Figure 7.4 illustrates these coordinates. Up to 80 tracks per jet are allowed, which is
1406 a threshold chosen to generally include all the tracks in the jet, which leads to maximal perfor-

1407 mance. Figure 7.5 shows the track multiplicity in the leading and subleading jet for the signal and
 1408 background samples used in training.

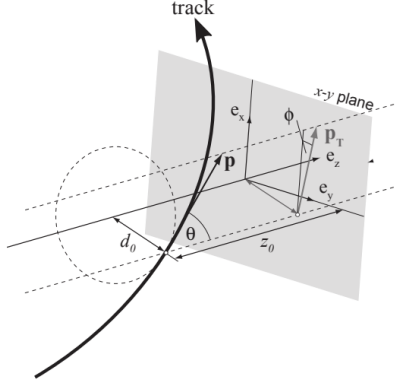


Figure 7.4: Illustration of track coordinates d_0 and z_0 .

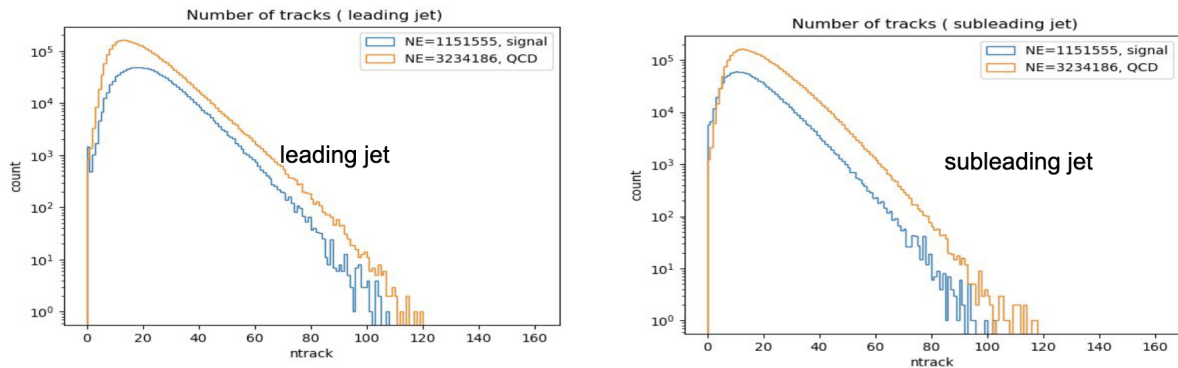


Figure 7.5: Distributions of the track multiplicity in the leading and subleading jets, comparing signal and background PFN training samples.

1409 These tracks (up to 160 total) are the input to the PFN. Referencing Equation 7.1, this corre-
 1410 sponds to $M = 160$ and $d = 6$. The two leading jets and their associated tracks are rotated so
 1411 that the center of the system is aligned with $(\eta, \phi) = (0, 0)$. Each track is normalized to its relative
 1412 fraction of the total dijet system energy and transverse momentum- this enforces agnosticism to the
 1413 total energy and transverse momentum of the event. The rotation and scaling are motivated by the
 1414 procedures described in [71] to improve the optimality of the PFN learning. Figure 7.6 illustrates
 1415 the rotation process.

1416 Finally, each of the 6 track variables is scaled so that its range is $[0,1]$. This is a common

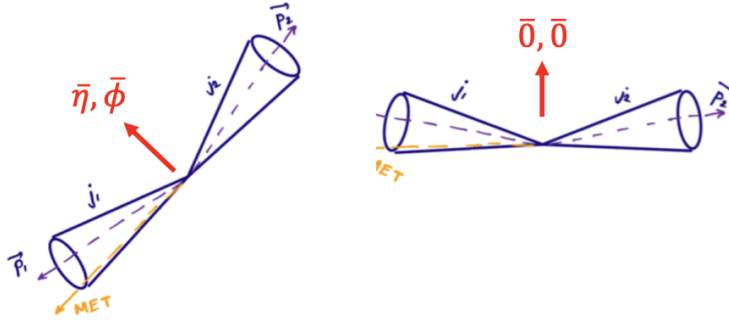


Figure 7.6: A diagram demonstrating how the two jet system is rotated in (ϕ, η) .

1417 preprocessing step that ensures the input data is bounded over a similar range, so that arbitrarily
 1418 large values don't develop an outsized impact on the model. Figure 7.7 show each of 6 track
 1419 variables before and after scaling and rotation have been applied, demonstrating the impact of
 1420 these procedures, as well as the track level similarities differences between the background SM
 1421 QCD processes and the signal SVJ processes. Figure 7.8 illustrates that the data is well modeled
 1422 by the MC at track level.

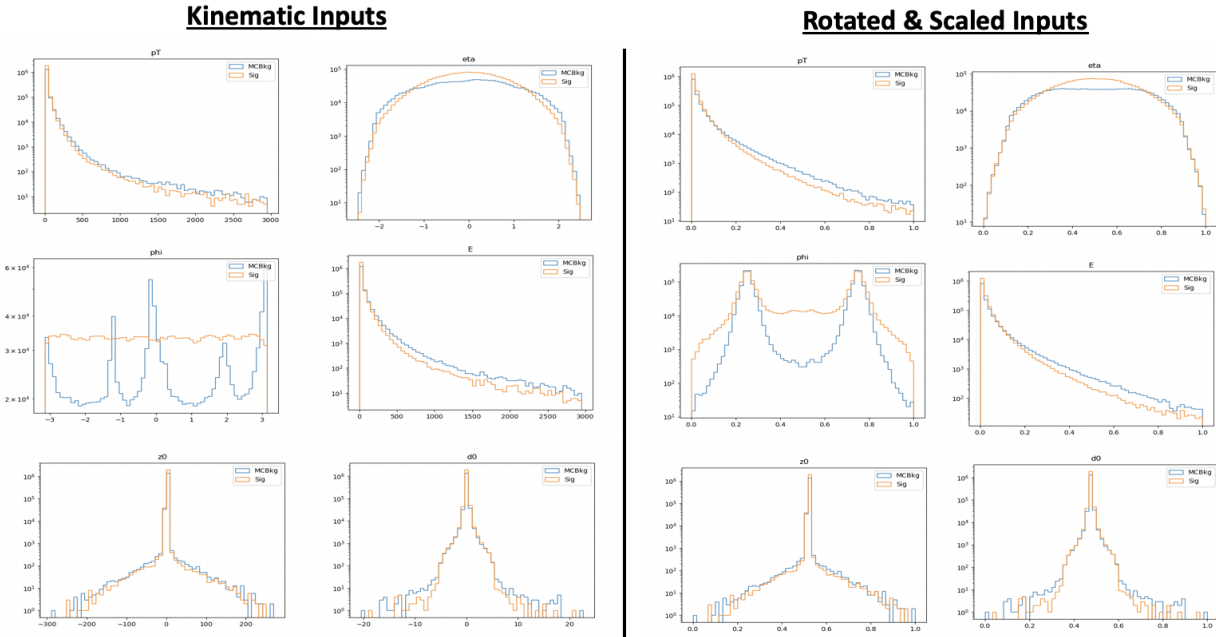


Figure 7.7: The 6 PFN track variables in background MC and signal MC. There are some differences between signal and background, but the track kinematics are largely similar.

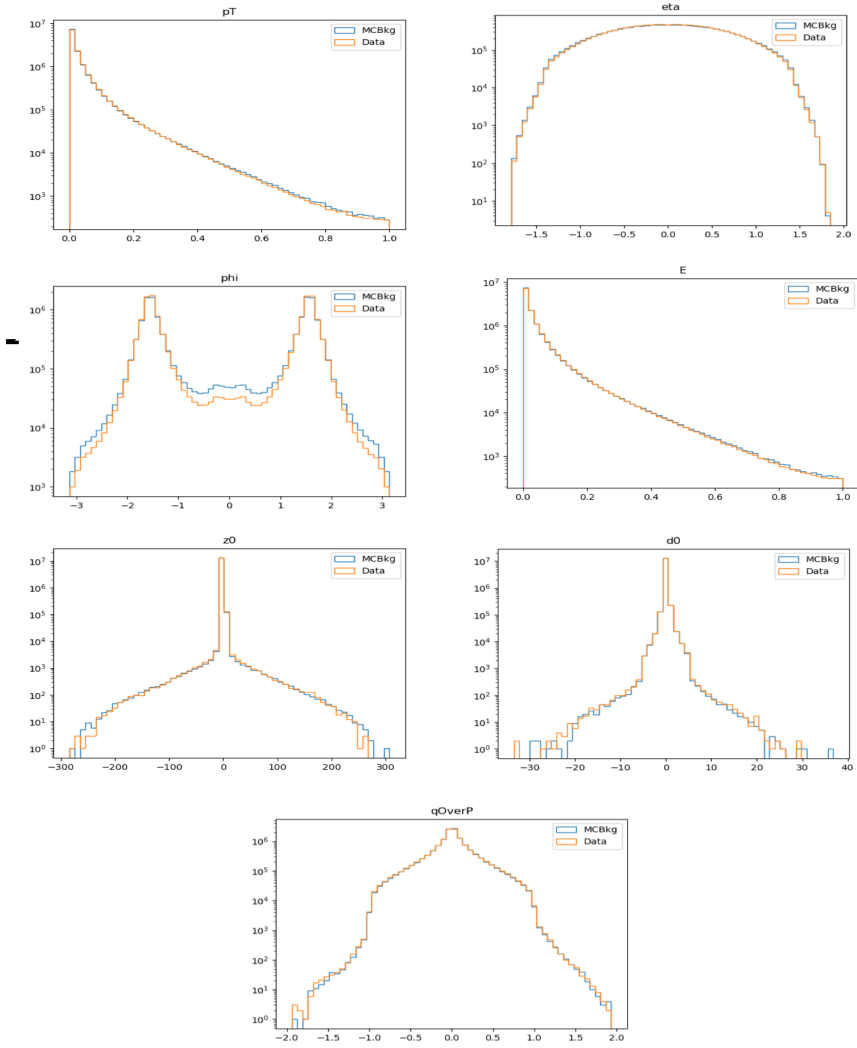


Figure 7.8: The 6 PFN track variables in data and background MC, after the scaling and rotation procedure is applied. There is excellent modeling of the data by the MC within the track variables. The slight discrepancy in the ϕ distribution is due to the modeling of dead TileCal cells by the QCD MC, which will be discussed in Chapter 8. The level of discrepancy is determined to be within tolerance given that the final result will be data driven and the QCD model is used in the PFN training only.

1423 **Training**

1424 As seen in Figure 7.2, two separate architectures are defined and combined to do the super-
1425 vised training. The PFN uses a masking layer to suppress any zero-padded inputs, making the
1426 architecture length agnostic. The masking layer ignores any all-zero inputs in the summation layer.
1427 Additionally, The summation layer in the PFN enforces permutation invariance, so the network is
1428 unordered. The Φ network has 3 dense layers of dimensionality 75 with RELU activation, with
1429 27.5k trainable parameters and an output Φ latent space dimension of 64.

1430 The classifier F network similarly has 3 dense layers with 75 nodes with RELU activation, and
1431 a final softmax layer to determine the event-level classification with a categorical cross-entropy
1432 loss. The Adam optimizer is used with an initial learning rate of 0.001.

1433 The PFN is trained in a fully supervised way using SVJ signal MC and QCD MC events. Al-
1434 though several SM processes are expected to contaminate the SR (see Chapter 8), QCD is the dom-
1435 inant background. Training against a QCD-only sample is determined to produced better results
1436 than training on a more complete background - when training with a background which repre-
1437 sents samples that are more enriched in E_T^{miss} , the ability of the PFN to identify high E_T^{miss} signals
1438 is reduced. When training with a QCD-only background, there is greater contamination from
1439 E_T^{miss} enhanced backgrounds in the final SR - however the increased signal acceptance means that
1440 overall sensitivity is still higher with a QCD-only training. This can be seen in the comparison of
1441 output classifier distributions in Figure 7.9.

1442 500k events from both background and signal are used in training, where the signal is a com-
1443 bined file of all simulated signal points and the full QCD background which is sampled according
1444 to it's MC weights to produce the proper p_T input shape. A study was done to check the optimality
1445 of the inclusive signal model PFN as compared to one trained on high and low R_{inv} points sepa-
1446 rately, to better capture the differences in high and low E_T^{miss} across signals and backgrounds, but
1447 a small effect is found and the decision is taken to keep the inclusive model (Appendix B.2).

1448 The network is trained for 100 epochs. A train/test/validation split of 78%, 20%, and 2% is used
1449 for the final PFN training. Figure 7.10 shows the loss during training, which is stable and flattens

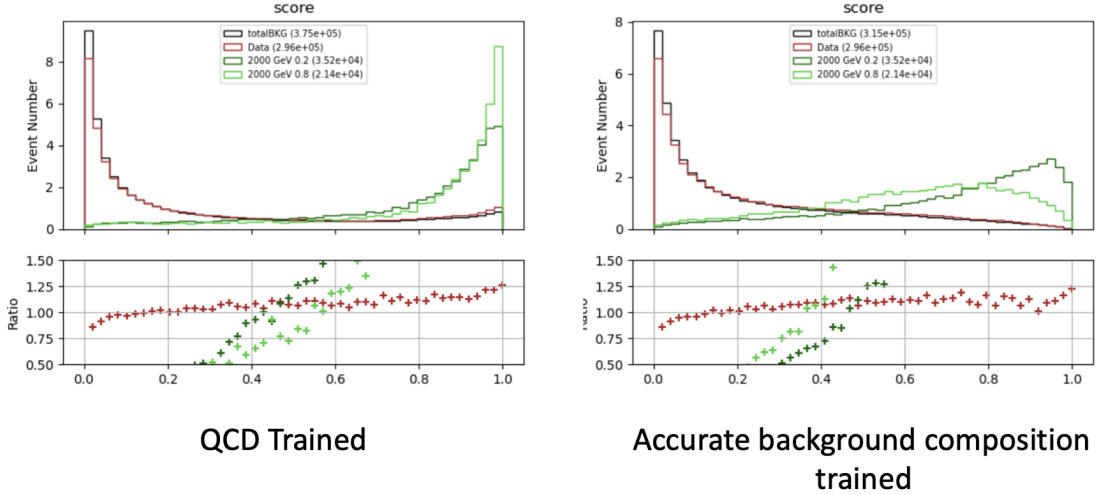


Figure 7.9: PFN score for background MC, data, and signal, comparing a PFN training on QCD-only vs all-background MC samples. The average AUC for the QCD-only training (left) is 0.93, while the average AUC for the mixed background training (right) is 0.84. The sensitivity estimate across the grid is better for the QCD-only training - from the distribution we can conclude that this is because the sensitivity to MET enhanced signals is greatly reduced.

1450 by the end of training, and the final evaluated losses that provide signal-background discrimination
 1451 over the test set.

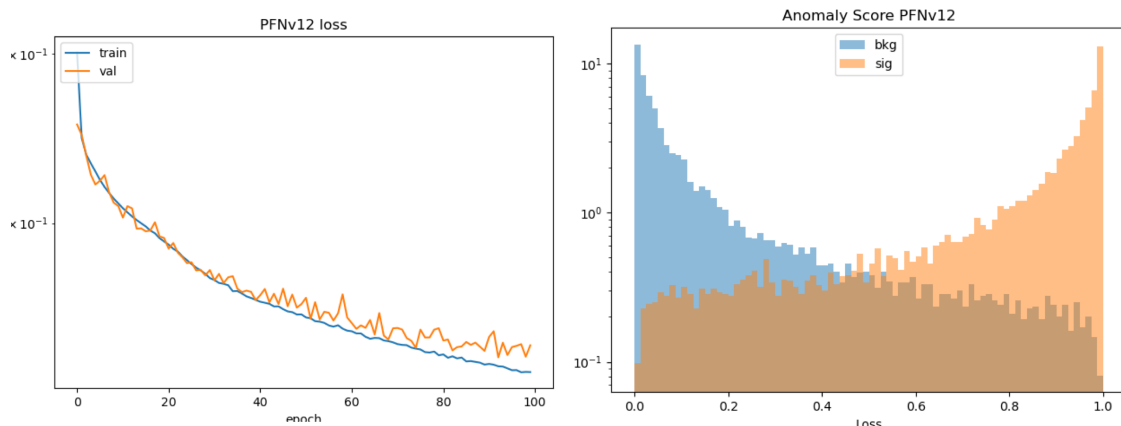


Figure 7.10: PFN architecture loss during training as a function of epoch (left) and the evaluated loss over the signal and background (right).

1452 Optimization studies were performed on the PFN, varying the number of training epochs, num-
 1453 ber of training events, batch size, learning rate, number of neurons, and dimension of the Φ space.
 1454 A summary of these studies is presented in Appendix B.2. The model presented here represents an
 1455 optimal choice across these parameters.

1456 **Performance**

1457 The performance of the PFN can be assessed via the area-under-curve (AUC) of the receiver
1458 operating characteristic (ROC) associated to evaluating the PFN on the test set of signal and back-
1459 ground events. Figure 7.11 shows the ROC curve of the PFN when classifying the QCD back-
1460 ground from the combined signal, with an AUC of 0.93. Figure 7.12 shows the AUC of the PFN
1461 across the SVJ signal grid, demonstrating strong discrimination capability even in the varying cor-
1462 ners of phase space. Figure 7.13 shows the output score distribution in two signals, data, and the
1463 total background MC. A selection of PFN score > 0.6 for all SR events is chosen to maximize
signal sensitivity across the grid.

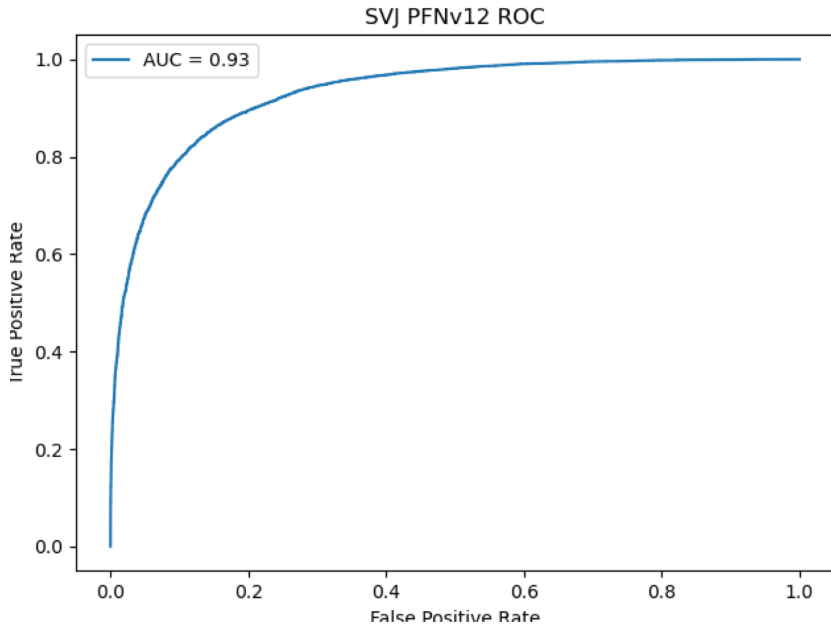


Figure 7.11: ROC the PFN score for combined signal (true positive) and QCD background (false positive).

1464

1465 Another supervised approach was studied using a BDT as the primary selection tool, trained
1466 over high-level variables describing each event. Studies comparing the PFN and BDT approaches
1467 are provided in Appendix B.3. Ultimately the low-level high-dimensional approach offered by the
1468 PFN was selected for its increased performance and lessened kinematic dependence.

1469 Appendix B shows more studies on the ML methods and comparisons of varying approaches.

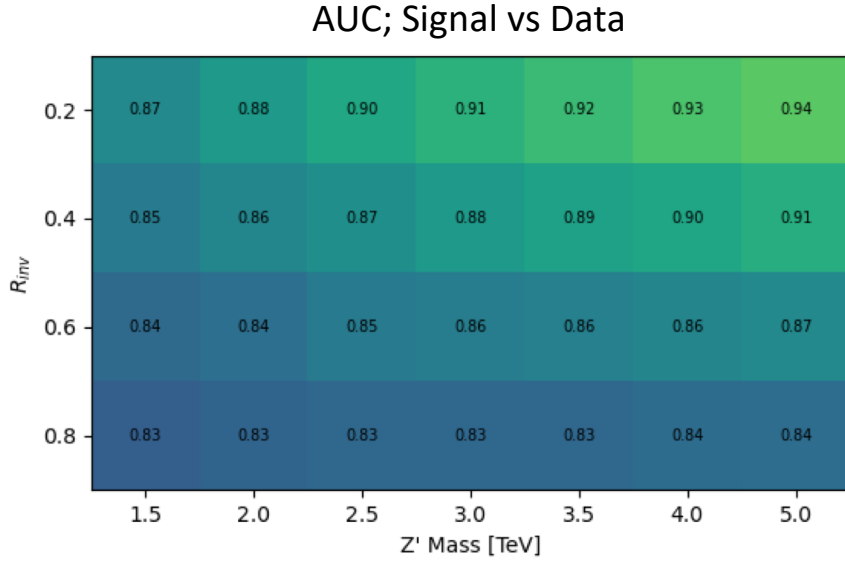


Figure 7.12: AUC from the PFN score for each signal in the SVJ grid, shown versus the QCD-only training sample.

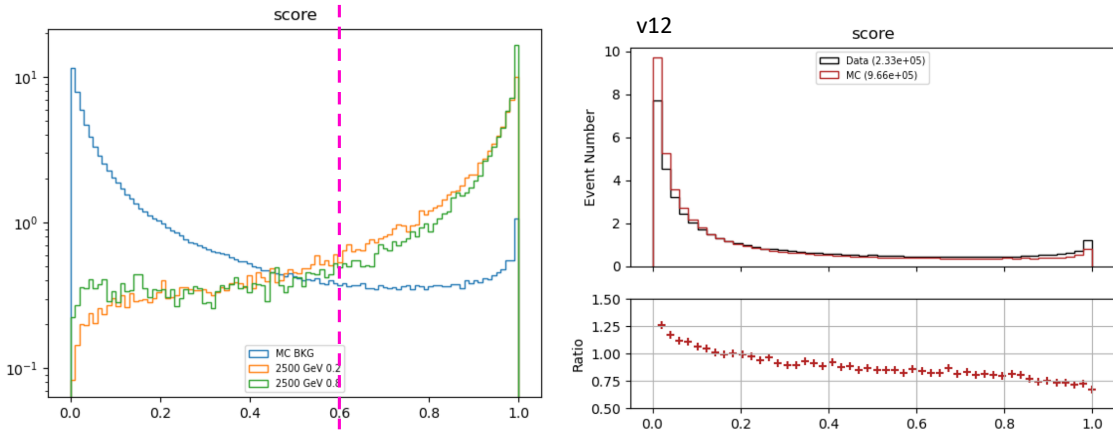


Figure 7.13: PFN score for two signals and the total background MC (top), and between data and MC (bottom). The difference between data and MC efficiency is minimal (< 5%).

1470 7.1.2 ANTELOPE (Semi-supervised)

1471 The semi-supervised analysis approach broadens the discovery sensitivity of the search through
1472 the use of semi-supervised ML, where training of the model is data-driven and labels are only
1473 partially provided during training. While broad sensitivity is a general key goal of LHC searches,
1474 it is particularly motivated in the case of dark QCD models, which can lead to widely varying
1475 topologies depending on the values of model parameters. In the case of SVJs, the R_{inv} fraction in
1476 the jet can dramatically vary the E_T^{miss} , shower shape, and other key features, making it difficult to
1477 find a single standard analysis variable that can distinguish all signal topologies from QCD.

1478 **Architecture Fundamentals**

1479 The model-independent search region of this analysis is implemented with a novel ML ap-
1480 proach that builds on the ANTELOPE architecture to construct a tool that is capable of performing
1481 low-level anomaly detection with permutation-invariant inputs. This tool, referred to as **ANomaly**
1482 **deTEction on particLe flOw latent sPacE (ANTELOPE)**, is a custom solution designed for this
1483 analysis.

1484 ANTELOPE uses the supervised signal vs. background training of the PFN network described
1485 in the previous section to generate a permutation invariant latent space that is representative of the
1486 original input variables, encodes the input events into these latent space variables O , and trains a
1487 *variational autoencoder* (VAE) over the events modeled as PFN latent space variables. A VAE
1488 is a common architecture used for anomaly detection and data-driven ML training. It has been
1489 used in previous ATLAS searched to model jet level information, such as the search presented
1490 in [73] using the recurrent architecture described in [72]. One of the limitations of a recurrent
1491 architecture is the need to order the low level inputs, which affects the performance of the tool. Jet
1492 constituent information is intrinsically unordered, and therefore a permutation invariant approach
1493 removes this element of arbitrary decision making from the modeling process. A visual example
1494 of the ANTELOPE inputs is given in Figure 7.14.

1495 The input to the model is the same 6 track variables for the leading 160 tracks of the leading

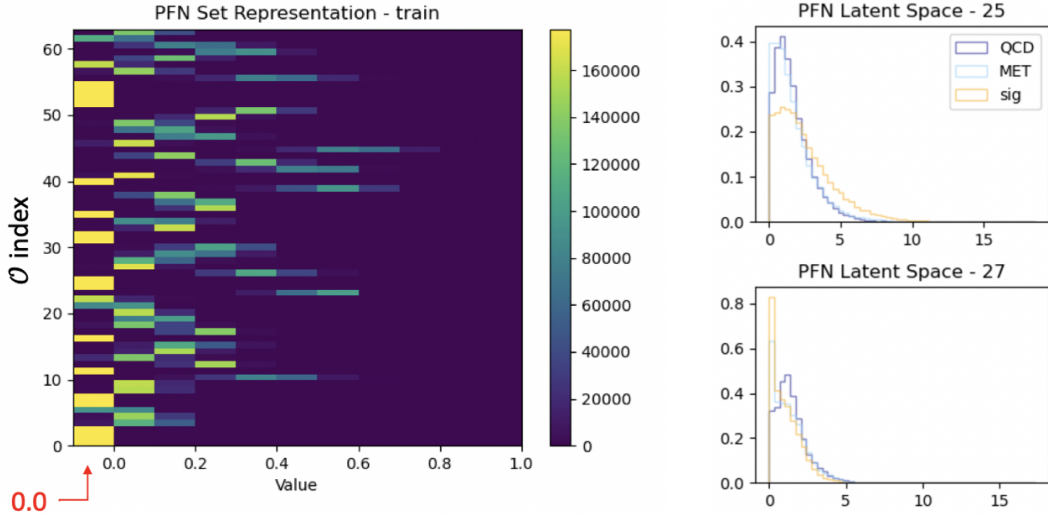


Figure 7.14: A visual representation of the 64 PFN latent space variables which create the input of the VAE component of ANTELOPE. The left shows a 2D histogram of the PFN latent space index (0-63) versus the value assumed by that index. The right shows 1D histograms of two particular PFN latent space variables.

1496 two jets, as presented in Section 7.1.1. The track information is encoded to the PFN Φ latent
 1497 space using the pre-trained Φ network (trained according to the steps outline in Section 7.1.1. The
 1498 resulting Φ basis is summed to created the fixed length symmetric representation O . The VAE is
 1499 then trained in an unsupervised way using inputs encoded to O from data events only. The VAE is
 1500 given no knowledge of the signal model during training. It is able to perform anomaly detection
 1501 through an encoder stage which does a lossy compression on the input to a lower-dimensional
 1502 latent space, and a decoder stage that samples from that latent space and generates an output of the
 1503 original dimensionality. By using the reconstruction error as a loss, this process enables the VAE
 1504 to develop a knowledge of the underlying data structure, thereby isolating new out-of-distribution
 1505 events by their high reconstruction error. This strategy is semi-supervised because the tool has
 1506 some knowledge of correct labels (eg. through the PFN latent space embedding) but is followed
 1507 by a data-driven unsupervised stage.

1508 Figure 7.15 provides a diagram of the ANTELOPE architecture.

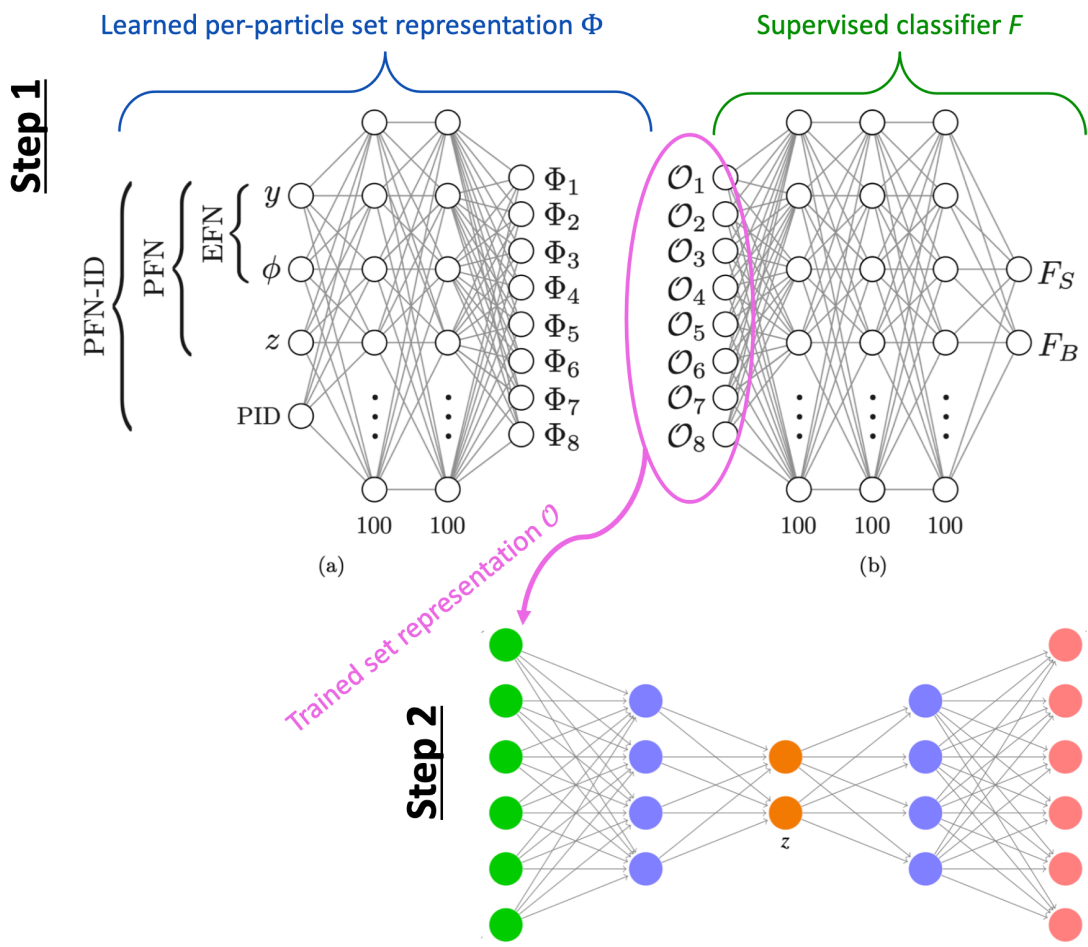


Figure 7.15: An annotated diagram of the ANTELOPE architecture.

1509 **Training**

1510 The VAE stage of the ANTELOPE network is trained directly over a subset of data events
1511 at preselection (6.7 million available, 500,000 used, with a 80% / 20% training/test split). The
1512 input dimensionality of the VAE has to match the encoded Φ dimension of the PFN, in this case
1513 64. The encoder has an encoding layer that brings the dimensionality to 32, and a final layer that
1514 compresses to the latent space dimension of 12. The network is trained for 50 epochs, with a
1515 learning rate of 0.00001. The loss \mathcal{L} is the sum of two terms, the mean-squared error (MSE) of
1516 input-output reconstruction, and the Kullback-Leibler divergence (KLD).

$$\mathcal{L} = \sum_i L_i = \sum_i |\Phi_i^2 - \Phi'_{\ell i}|^2 + \lambda D_{\text{KL}} \quad (7.2)$$

1517 As the PFN inputs are sufficiently normalized to remove any spurious information from train-
1518 ing, no additional normalization is applied to the PFN encoded inputs. The final ANTELOPE score
1519 used in the analysis is produced by applying a log + sigmoid transformation function to the total
1520 evaluated loss \mathcal{L} .

Figure 7.16 shows the loss during training.

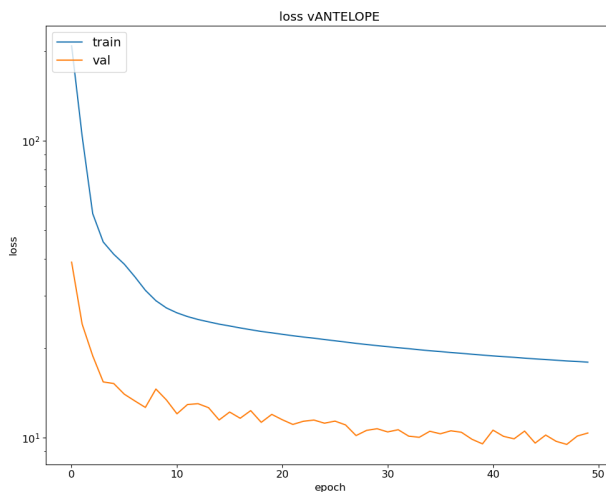


Figure 7.16: ANTELOPE architecture loss during training as a function of epoch.

1521

1522 **Performance**

1523 As with the PFN, the ANTELOPE performance is assessed via the area-under-curve (AUC) of
1524 the receiver operating characteristic (ROC) associated to evaluating the ANTELOPE on the test
1525 set of signal and background events. Figure 7.17 shows the output score distribution in data and
1526 total background MC, showing a very flat ratio and motivating the use of MC for studies of the
1527 ANTELOPE score.

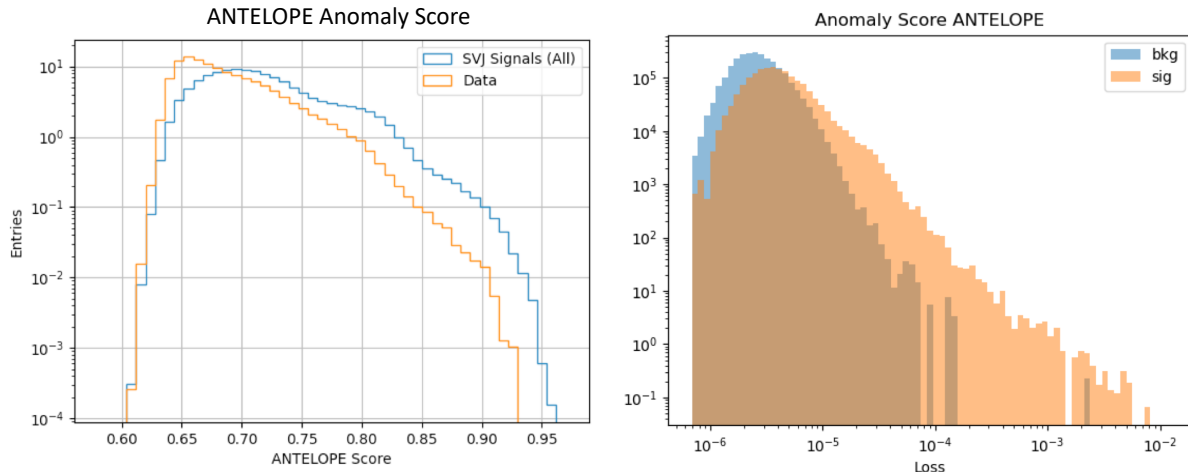


Figure 7.17: ANTELOPE score distribution comparing data and the total background MC (left), with good agreement observed between data and simulated background, and comparing all background MC to signals (right), revealing good discrimination power.

1528 Figure 7.18 shows the AUC of the ANTELOPE across the SVJ signal grid, demonstrating
1529 strong discrimination capability even in the varying corners of phase space. Compared to the
1530 supervised PFN method, the ANTELOPE is not as performant (as expected due to the absence of
1531 signal model in training). However, a selection on events with high ANTELOPE score nonetheless
1532 provides a 10-40% increase in signal significance by removing background and isolating the long
1533 tail of anomalous events.

1534 **Model Independence** The unsupervised component of training the ANTELOPE network is ex-
1535 pected to give it a more generalized sensitivity to new physics with E_T^{miss} and jet activity, beyond
1536 the scope of the SVJ grid. To assess this, alternative signal models are evaluated with the trained

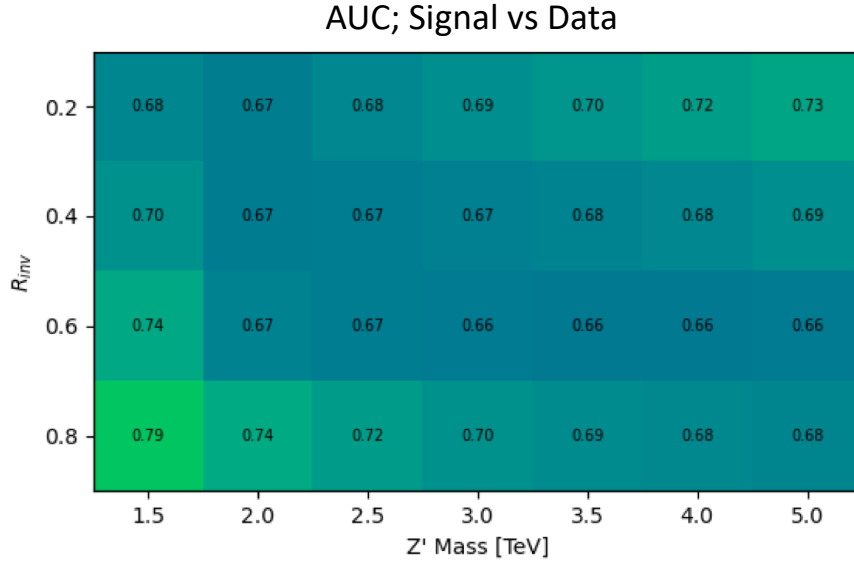


Figure 7.18: AUC from the ANTELOPE score for each signal in the SVJ grid.

1537 ANTELOPE network, as optimized for the SVJ grid, and their sensitivity in the analysis selection
 1538 is evaluated.

1539 The following alternate signal models were considered:

- 1540 • $Z' \rightarrow t\bar{t}$
 1541 • $W' \rightarrow WZ$
 1542 • Gluino pair production \rightarrow R-hadron + LSP (E_T^{miss}) with gluino masses 2000/3000 GeV, LSP
 1543 mass 100 GeV, and lifetime 0.03 ns (LSP = *lightest supersymmetric particle*)
 1544 • Emerging jets s-channel with mass 1000 GeV and lifetime 1ns

1545 Figure 7.19 shows the distribution of these signals in the PFN score and the ANTELOPE score.
 1546 This comparison reveals that ANTELOPE is sensitive to E_T^{miss} in the event; it classifies signals
 1547 with no real E_T^{miss} , like the all-hadronic Z' and W' decays (given our imposed lepton veto) as
 1548 data-like, but the distributions for signals with E_T^{miss} such as SVJs, R-hadrons, and emerging jets
 1549 have distributions with higher anomaly score tails.

1550 Figure 7.20 shows a comparison of the sensitivity of the PFN and ANTELOPE regions across
 1551 a variety of signals, including the combined SVJ signal used to train the PFN. The benefit of the

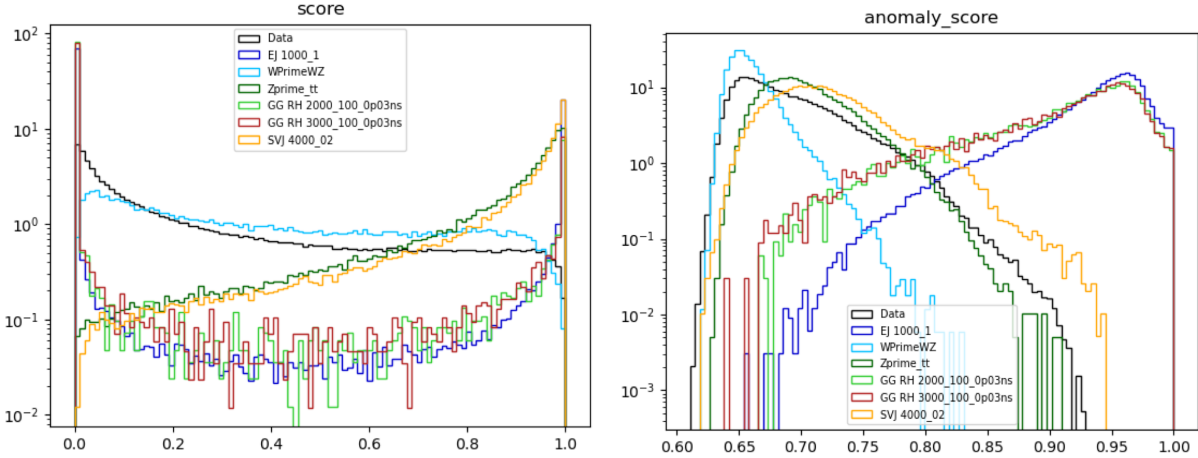


Figure 7.19: Comparing data and the alternate signal models for the PFN score (left) and ANTELOPE score (right). The emerging jet signal is an example of the gain of the model-independent ANTELOPE approach, where it has a bimodal shape in PFN score but is clearly tagged as anomalous by ANTELOPE.

1552 unsupervised stage of ANTELOPE in enhancing model independence is clearly seen through the
 1553 boost in performance for other signal models, namely the gluino and emerging jet signals, which
 1554 have more E_T^{miss} than the W' and Z' signals (all-hadronic) that were also tested. As commented
 1555 above, the PFN outperforms ANTELOPE as expected, because it was designed explicitly for the
 1556 task of classifying SVJs from background, demonstrating the power of supervised learning for the
 1557 model-specific approach.

$\text{sig eff} / \sqrt{\text{bkg eff}}$ for respective score cut (0.6 PFN, 0.7 ANTELOPE)

	EJ 1000	WprimeWZ	Zprime tt	GG RH 2000	GG RH 3000	SVJ
PFN	0.57	0.65	1.92	0.30	0.32	1.97
ANTELOPE	1.73	0.07	0.84	1.72	1.72	1.13

Figure 7.20: Comparing data and the alternate signal models in terms of sensitivity (S/\sqrt{B}) for the PFN and ANTELOPE tools, applying the selection that is used in the analysis. The ANTELOPE network is found to provide significant added sensitivity to alternate signals such as the gluino→R-hadron and emerging jets, which have higher E_T^{miss} than the SVJs.

1558 Studies on the ANTELOPE architecture and comparisons to other methods can be found in
 1559 Appendix B.1.

1560

1561

Chapter 8: Analysis Strategy

1562 This chapter will present the strategies used to isolate ATLAS data events most consistent with
1563 the SVJ model and to estimate the relevant background. The data and MC samples discussed in
1564 Chapter 6 are studied to create the analysis strategy, and the ML scores discussed in Chapter 7
1565 are used to isolate the most signal like events. A *preselection* selects events consistent with the
1566 SVJ topology based on basic features of the jets and E_T^{miss} . Preselected events are then split into
1567 a *control region* (CR), *validation region* (VR), and *signal region* (SR). The CR is used to estimate
1568 the estimate the background and the VR is used to validate that estimation. The SR is blinded
1569 during the development of the analysis strategy, and only unblinded to make the final measurements
1570 presented in Chapter 9. The final result is a polynomial fit of the *transverse mass* (m_T) spectrum
1571 in the SR. The preselection, region definitions, and polynomial fit will be discussed in detail in the
1572 following sections.

1573 **8.1 Preselection**

1574 The preselection isolates the phase space of events that most closely match the SVJ signal
1575 topology. Each cut was determined to reduced the background and enhance signal sensitivity. The
1576 list of preselection cuts and the motivation behind each cut are as follows. Here “jets” refer to
1577 anti- k_t R=0.4 jets, as discussed in Chapter 5.

- 1578 • At least 2 jets; in order to reconstruct the resonance mass
- 1579 • Leading jet $p_T > 450$ GeV; to ensure the use of the trigger in its efficiency plateau
- 1580 • Subleading jet $p_T > 150$ GeV; to mitigate the presence of non-collision background (Ap-
1581 pendix B.6.1)

- 1582 • $|\eta_{j1,j2}| < 2.1$; to ensure jets are fully within the tracker
- 1583 • $\Delta Y < 2.8$ (difference in rapidity between the two leading jets); to ensure central production
1584 associated to hard scatter
- 1585 • $E_T^{\text{miss}} > 200 \text{ GeV}$; to focus phase space on events with dark particles
- 1586 • $m_T > 1.2 \text{ TeV}$, to ensure a smoothly falling m_T distribution for fitting (Section 8.4)
- 1587 • At least 3 tracks for each of the two leading jets; to ensure good modeling
- 1588 • $\Delta\Phi(j_1, j_2) > 0.8$; to mitigate the presence of non-collision background (Appendix B.6.1).

A cutflow showing the impact of these cuts in data and signal is shown in Figure 8.1.

Data			Signals - All		
Cut	Statistics	Rel. Efficiency	Cut	Statistics	Rel. Efficiency
Initial	1.71E+10		Init	6.66E+05	
Trigger	3.45E+08	0.0202	Trigger	2.83E+05	0.4245
N. jets ≥ 2	2.84E+08	0.8233	N. jets ≥ 2	2.80E+05	0.9896
Leading Jet Pt $> 450 \text{ GeV}$	1.49E+08	0.5235	Leading Jet Pt $> 450 \text{ GeV}$	2.21E+05	0.7900
Lead Jet Eta < 2.1	1.42E+08	0.9528	Lead Jet Eta < 2.1	2.19E+05	0.9922
Subleading Jet Eta < 2.1	1.33E+08	0.9432	Subleading Jet Eta < 2.1	2.12E+05	0.9661
$dY < 2.8$	1.29E+08	0.9628	$dY < 2.8$	2.11E+05	0.9934
MET > 200	7.07E+05	0.0055	MET > 200	1.13E+05	0.5370
$mT > 1200$	5.38E+05	0.7613	$mT > 1200$	7.94E+04	0.7019
Jet2 pT > 150	5.03E+05	0.9343	Jet2 pT > 150	6.14E+04	0.7739
$d\Phi(j_1, j_2) > 0.8$	4.97E+05	0.9890	$d\Phi(j_1, j_2) > 0.8$	5.83E+04	0.9494

Figure 8.1: Preselection cutflow for data (left) and signal (right).

1589
1590 With the exception of the cuts necessary to reduce the non-collision background, all cuts were
1591 verified to enhance signal sensitivity by improving s/\sqrt{b} , a standard estimate of discovery sensi-
1592 tivity, where s is the number of signal events and b is the number of background events. The cuts
1593 on ΔY and E_T^{miss} were optimized to enhance s/\sqrt{b} , and the other cuts were informed by the physics
1594 motivations provided above.

1595 Vetos are applied to reject any events where an error for a subdetector is flagged. This covers
1596 Tile/LAr calorimeter errors, single event upsets in the SCT, and incomplete events. To reject non-
1597 collision backgrounds (NCB), such as calorimeter noise, beam halo interactions, or cosmic rays,

1598 the standard ATLAS event cleaning procedure is applied. As this analysis is very dependent on
1599 E_T^{miss} associated to jets, the TIGHT event cleaning working point is applied. Tight cleaning requires
1600 jets to pass a stricter set of quality requirements compare to the LOOSE cleaning option. Due to
1601 the alignment between jets and E_T^{miss} in this phase space, it was found that two additional cuts
1602 (indicated above) are needed to remove NCB. The process for selecting these cuts is presented in
1603 Appendix B.6.1.

1604 The two leading in p_T jets in the event are considered as the dark quark candidates. This choice
1605 was determined by truth studies matching the dark quark to reconstructed jets in simulation, which
1606 indicate that the leading p_T assignment allows for high accuracy in ΔR matching to dark quarks.
1607 These studies can be found in Appendix C.

1608 Figure 8.2 and Figure 8.3 show the distribution of signal and background MC in several key
1609 analysis variables after preselection is applied.

1610 **8.2 SVJ Fit and Discovery Analysis Strategies**

1611 As was introduced in Chapter 7 this analysis is interested in achieving dual goals: to make
1612 the best possible measurement of the SVJ signal model generated for this analysis, and to broadly
1613 search for any signals consistent with dark QCD behavior and inconsistent with a Standard-Model-
1614 only background hypothesis. To this end, two parallel analysis strategies are developed.

1615 The SVJ Fit strategy uses the supervised PFN ML score in defining the signal region. Recall,
1616 the PFN is trained over simulated MC background and a combination of all MC SVJ signals. This
1617 gives this ML tool high sensitivity to the particular nuances of the SVJ shower predicted by the
1618 modeled theory. In addition to using the supervised ML tool, the SVJ Fit analysis strategy sets
1619 limits on the expected cross-section of each signal point in the SVJ signal grid. To achieve this, the
1620 shape of the SVJ signals are considered in the final fit, as will be elaborated on Section 8.5.1. The
1621 combination of the supervised PFN ML score and the signal-shape sensitive fitting strategy allows
1622 for the greatest possible sensitivity to the modeled signal process, thus allowing the analysis the
1623 best chance at discovery of this model, or enabling the analysis to set the best possible limits on

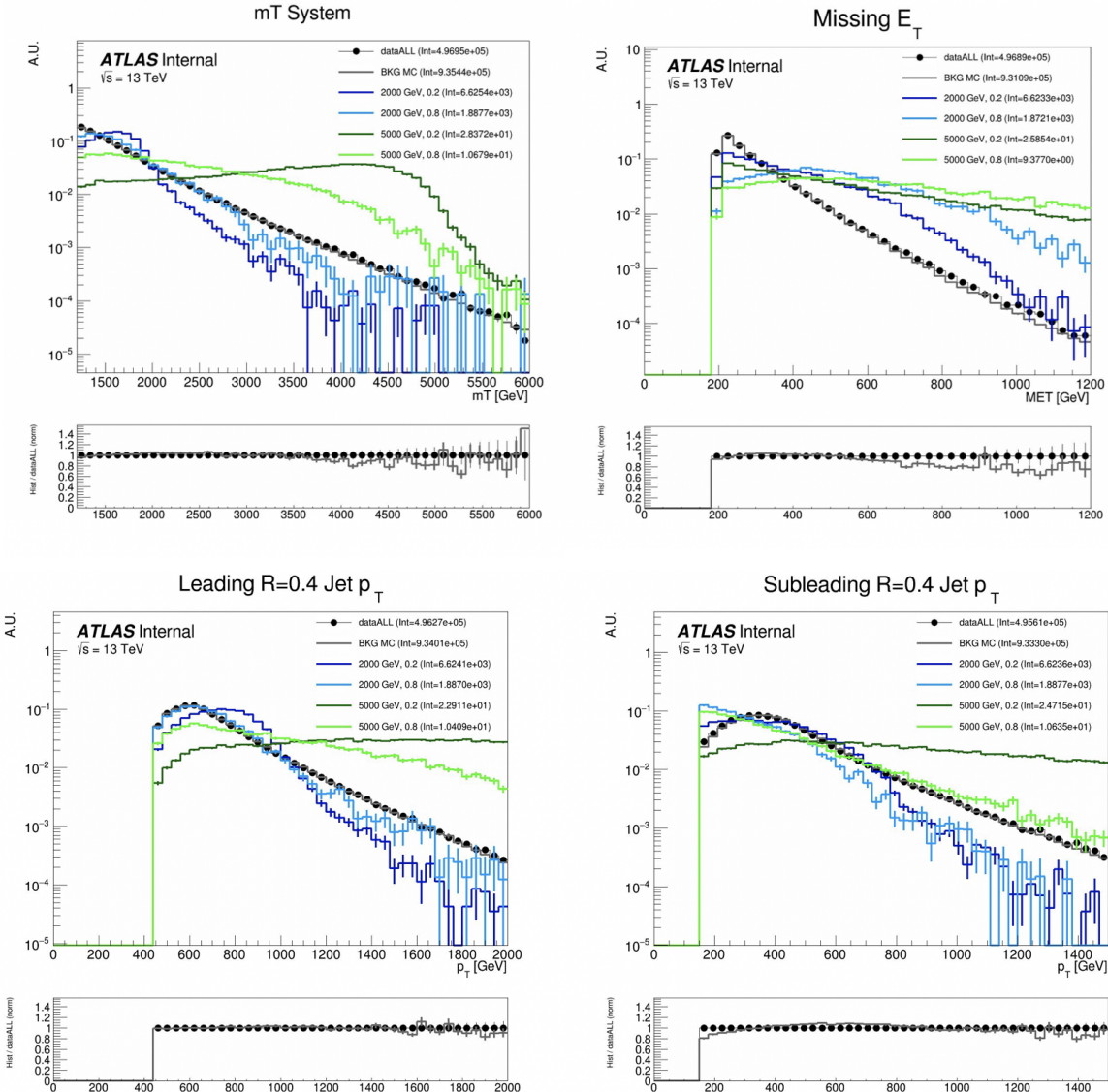


Figure 8.2: Energy and momentum analysis variables at preselection, for data, all background MC and representative signal models. m_T is the key fit variable, and this plot illustrates the smoothly falling background in comparison to the resonant shape of the signals. m_T is further illustrated in Figure 8.9.

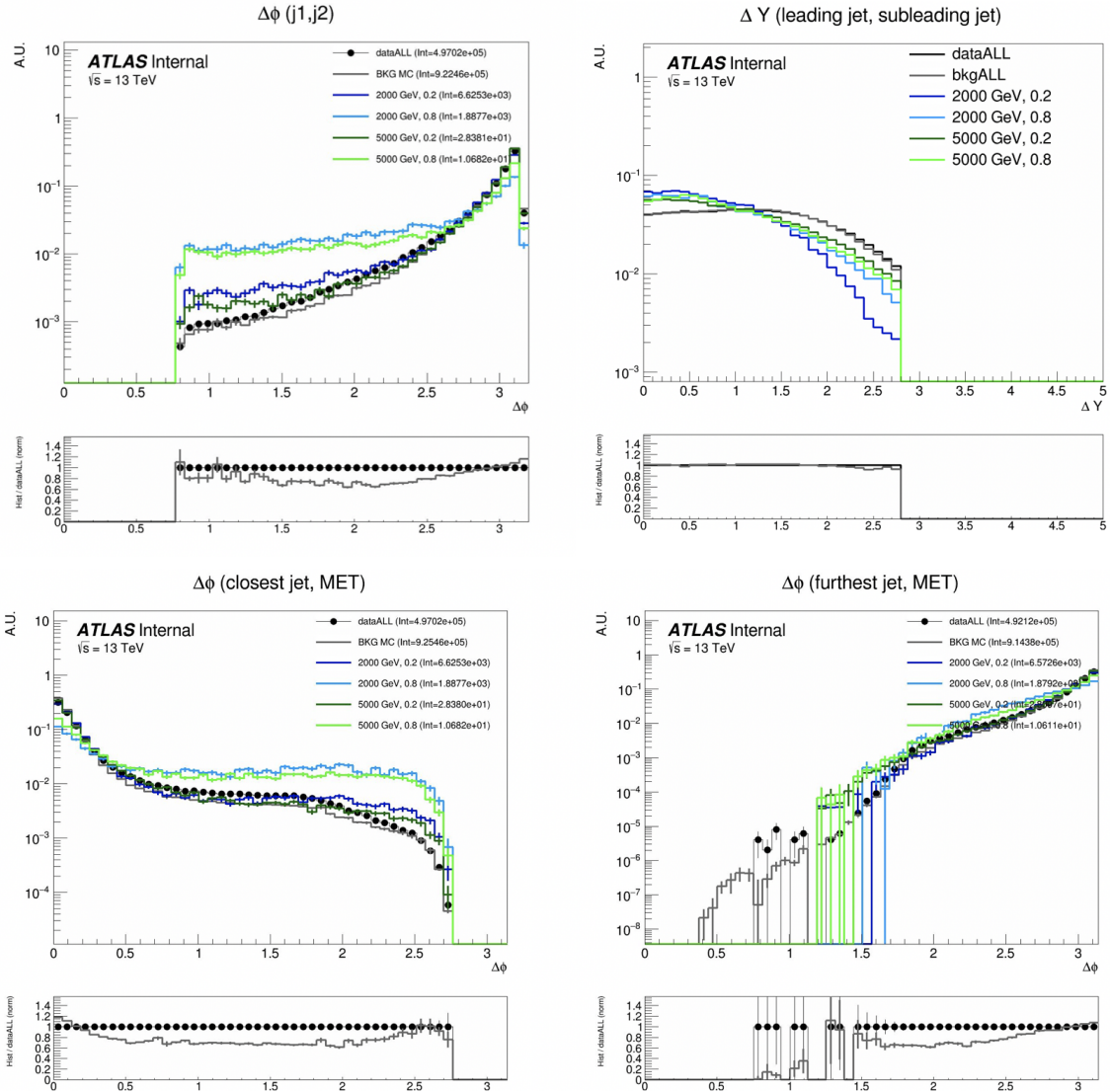


Figure 8.3: Orientation analysis variables at preselection, for data, all background MC and representative signal models. While $\Delta\phi(E_T^{\text{miss}}, j)$ variables are not used explicitly in the analysis flow, they help create a picture of the event.

1624 the observed cross-section.

1625 In contrast, the Discovery analysis strategy attempts to design a more general search, which
1626 could be sensitive to SVJs, but also to other possible hidden valley dark QCD models, such as
1627 fully dark jets or emerging jets [21]. The Discovery analysis strategy uses the semi-supervised
1628 ANTELOPE ML score in defining the signal region. Recall, the ANTELOPE is trained over AT-
1629 LAS data only, with no explicit knowledge of the SVJ signal behavior. The Discovery fit strategy
1630 is also signal model agnostic, by employing a bump hunt [74] strategy, which searches a smoothly
1631 falling template for any bumps inconsistent with a background only hypothesis. Therefore any
1632 signal which could present a resonant signature in m_T could show up as an excess in this strategy.

1633 The details of both strategies will be explored in the follow sections which detail the design
1634 of the signal regions and fit strategies. A diagram demonstrating the analysis flows can be seen in
Figure 8.4. Details on each selection and region can be found in the following subsections.

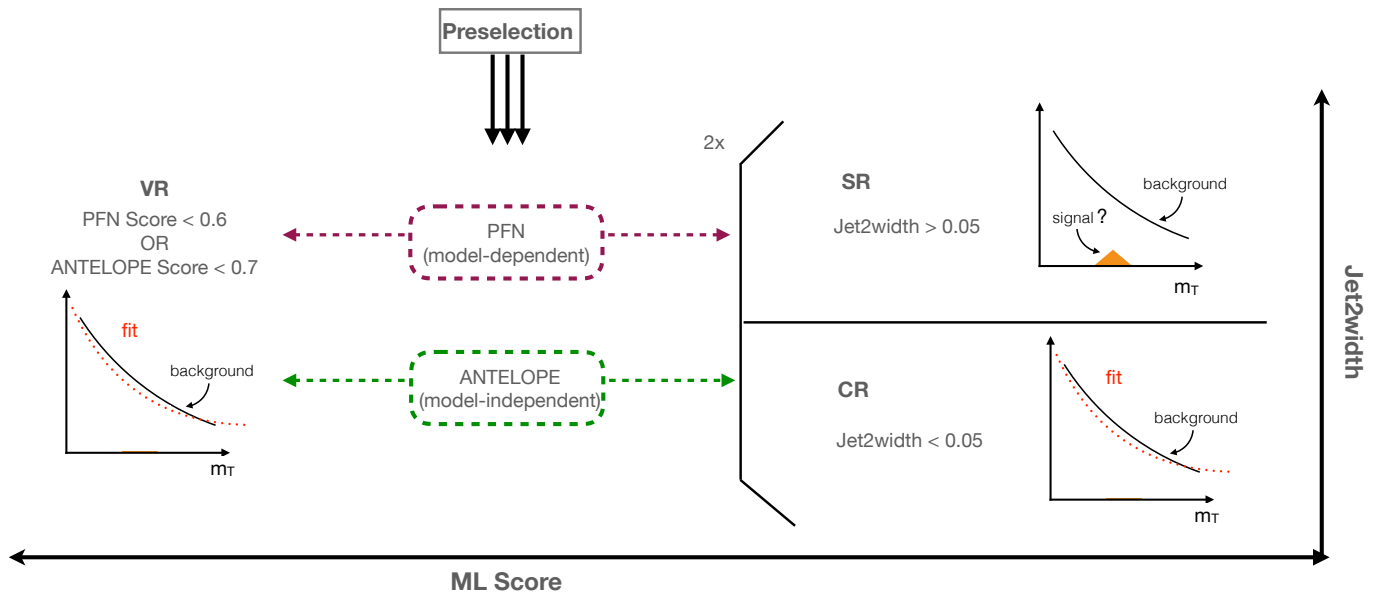


Figure 8.4: Flow of analysis selections, regions, and background estimation/validation fitting strategy. TODO: diagram needs to be corrected

1635

1636 **8.3 Analysis Regions**

1637 **8.3.1 Control and Validation Regions**

1638 The final background estimation will come from a polynomial fit to the m_T distribution in the
 1639 signal region. The control and validation regions are needed to develop and test this fit in data.

1640 To define the CR selection, a variable is needed that isolates background from all signals across
 1641 the (R_{inv}, m_Z) grid, which is challenging due to the varying nature of the signal models in quantities
 1642 such as E_T^{miss} and p_T balance, as illustrated in Figure 8.2. The variable *jet width* is chosen, which
 1643 is the calorimeter measurement of the width of a small-R jet as defined by the distance between
 1644 the cluster and the jet axis scaled by the jet energy [75]. Figure 8.5 shows this variable specifically
 1645 for the subleading jet width, in data, background MC and signal at preselection. The leading jet
 1646 width, which was determined to be less useful for isolating signal from background is also shown.
 1647 The subleading jet is more likely to be the jet aligned with MET, which is why the signal jet width
 1648 is consistently wider in the subleading jet, but not the leading jet. A selection of $\text{width}_{j2} < 0.05$ is
 1649 chosen for the CR, with the VR and SR therefore having a selection of $\text{width}_{j2} \geq 0.05$.

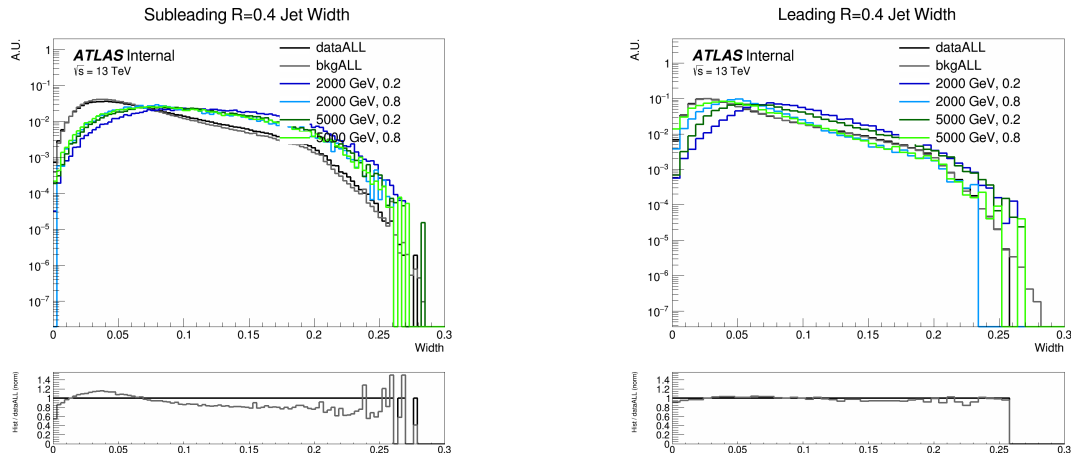


Figure 8.5: Distributions of the subleading jet width width_{j2} (left) and leading jet width width_{j1} (right) in data, background MC and signals at preselection. All SVJ signals are seen to be wider than the background in width_{j2} . The same is not true for width_{j1} , where some signals are observed to closely match the background.

1650 While the CR was used to develop the polynomial strategy, and is the primary region used in

many of the fit studies, a validation region is used as an additional check of the estimation strategy
 in data. The VR is defined using the region of events with low ML score by either the PFN or
 ANTELOPE networks. Here the analysis strategy splits into the two parallel strategies presented
 in Section 8.2: the SVJ fit strategy and the Discovery strategy. A selection of [PFN score ≤ 0.6
 & $\text{width}_{j2} \geq 0.05$] defines the SVJ Fit VR, while [ANTELOPE score ≤ 0.7 & $\text{width}_{j2} \geq 0.05$]
 defines the discovery VR.

There are therefore three variables that are crucial to the analysis strategy: width_{j2} , ML score,
 and m_T . Figure 8.6 shows the correlations of all three variables to one another. Any outstanding
 correlations are shown in Figure 8.7 to not sculpt the m_T distribution and only affect its slope,
 making these variables trustworthy for extrapolation across background/signal regions and final
 fitting procedures.

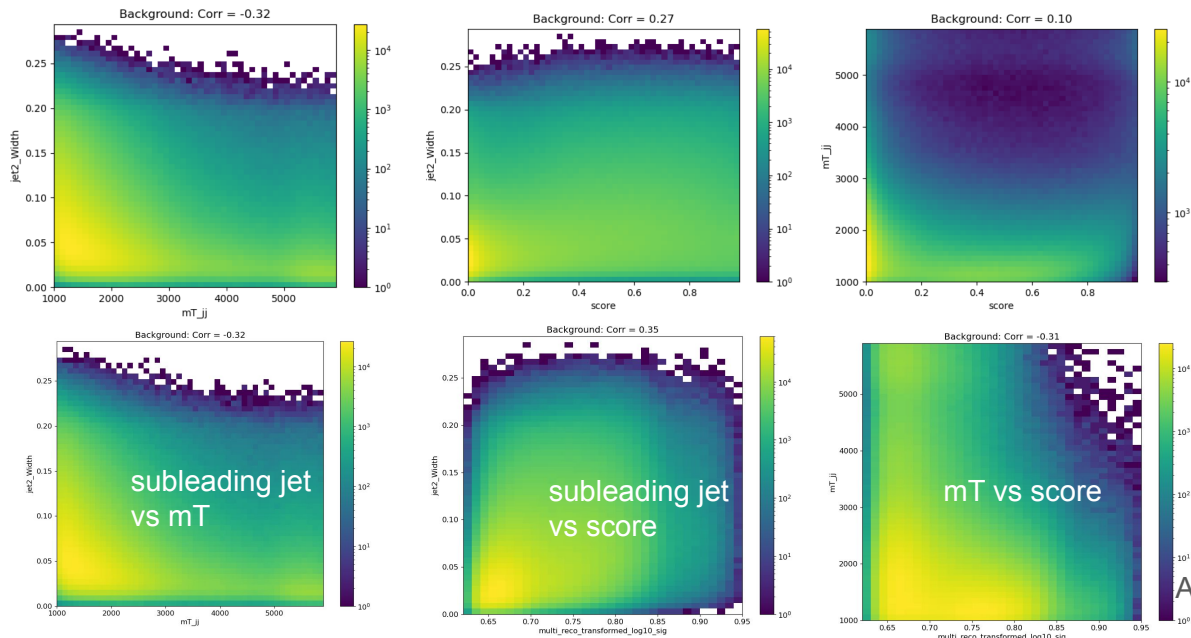


Figure 8.6: 2D plots revealing correlations between width_{j2} and m_T (left), width_{j2} and ML score (middle), and m_T with ML score (right). For the top row, the ML score is the PFN score, and for the bottom three, the ML score is the ANTELOPE score. Minimal correlations are observed and are shown to not sculpt m_T , validating these variables for analysis region construction and statistical treatment.

The most important variable for shape robustness across the CR, VR, and SR is m_T , as this
 is the variable that is fit for the statistical results. Figure 8.7 shows the distribution of m_T across

1664 the CR, VR, and SR, for both the PFN (supervised) and ANTELOPE (semi-supervised) strategies.
 1665 Some slope is observed in the ratio of the CR to the VR/SR shapes; however, the chosen back-
 1666 ground estimation strategy of polynomial fitting is expected to accommodate this slope. Further,
 1667 the ability of the background polynomial to fit both tail shapes will flex the fit framework in a
 1668 way that will generate higher confidence in the final ability to fit the SR. No significant bumps or
 sculpting are observed.

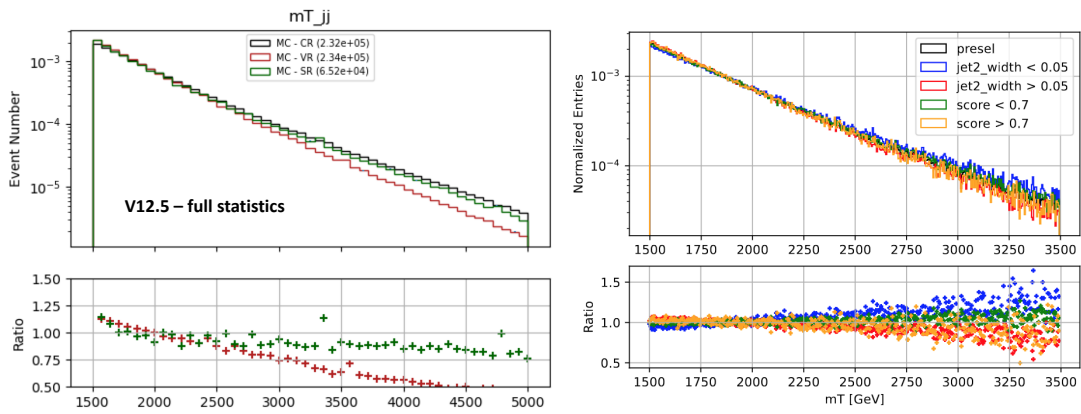


Figure 8.7: m_T in simulation across the CR, VR, and SR for both PFN (left) and ANTELOPE (right) selections.

1669

1670 8.3.2 Signal Region

1671 A selection of PFN score > 0.6 in the SVJ Fit region and ANTELOPE score > 0.7 in the
 1672 Discovery region is made to provide the primary signal-to-background enrichment, as motivated
 1673 by Section 7.1.1. These values are determined to maximize s/\sqrt{b} in each region. The additional
 1674 selection of $\text{width}_{j2} \geq 0.05$ orthogonalizes the SR to the CR. Note that the PFN and ANTELOPE
 1675 regions are not orthogonal; this is because the two analysis flows serve different purposes, their
 1676 statistical treatments are different, and they will not be combined.

1677 A summary of the SR, CR, and VR definitions can be seen in Figure 8.8, along with the relative
 1678 data statistics in each region.

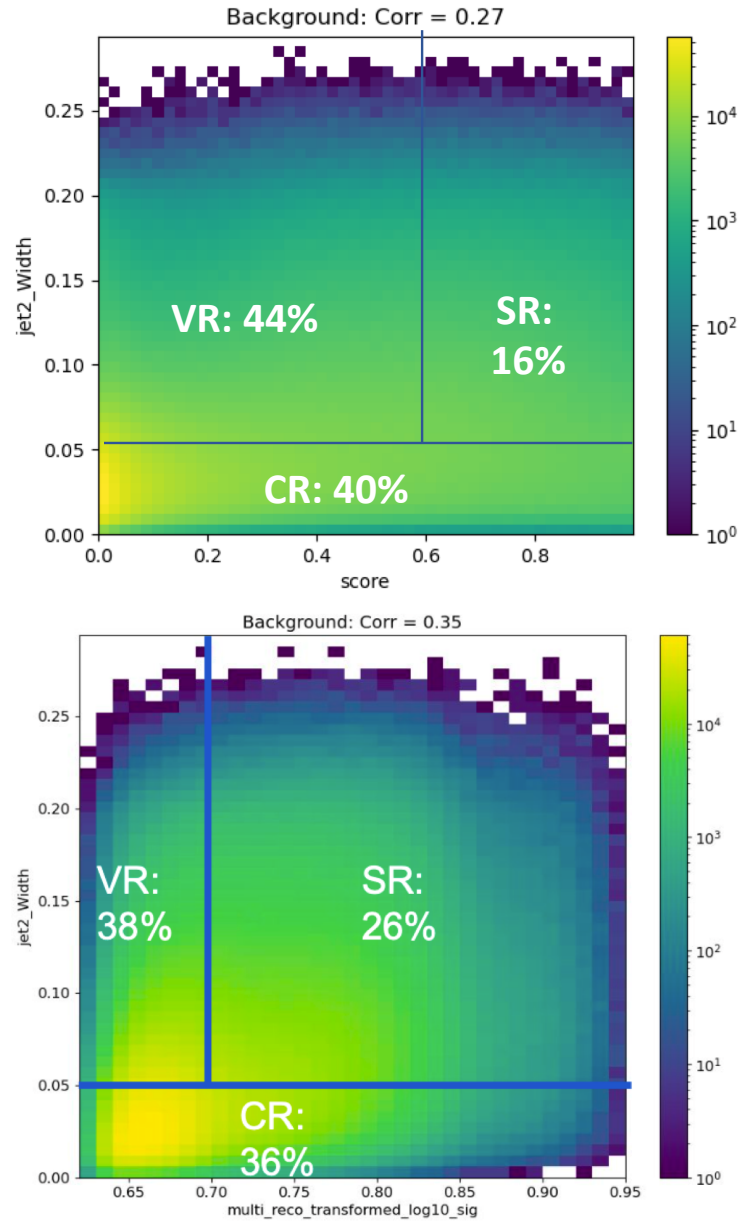


Figure 8.8: Definition of CR, VR, and SR regions using width_{j2} and the ML score, along with the population of each region in data statistics. The SVJ Fit region is shown on top with the PFN score on the x-axis, and Discovery region is shown on the bottom, with the ANTELOPE score on the x-axis.

1679 8.4 Background Estimation

1680 The transverse mass m_T is chosen as the search variable due to the potential for the SVJ signal
 1681 to create a resonant shape around the mass of the Z' . m_T is the total transverse mass of the two
 1682 leading jets and the E_T^{miss} , expressed in Equation 8.1 as:

$$1683 m_T^2 = [E_{T,jj} + E_T^{\text{miss}}]^2 - [\vec{p}_{T,jj} + \vec{p}_T^{\text{miss}}]^2 \quad (8.1)$$

1683 where $E_{T,jj}$ is the transverse energy of the dijet system. We take $E_{T,jj} = m_{jj}^2 + |\vec{p}_{T,jj}|^2$, where
 1684 m_{jj}^2 is the invariant mass of the two leading jets, and $\vec{p}_{T,jj}$ is the vector sum of the p_T of the two
 1685 leading jets. m_T is selected as the search variable in place of simpler invariant mass m_{jj} because
 1686 substantial energy from the Z' decay is captured in the E_T^{miss} . Therefore incorporating E_T^{miss} into
 1687 m_T improves the resonance around the mass of the Z' .

Figure 8.9 illustrates the resonance in m_T of the SVJ signals.

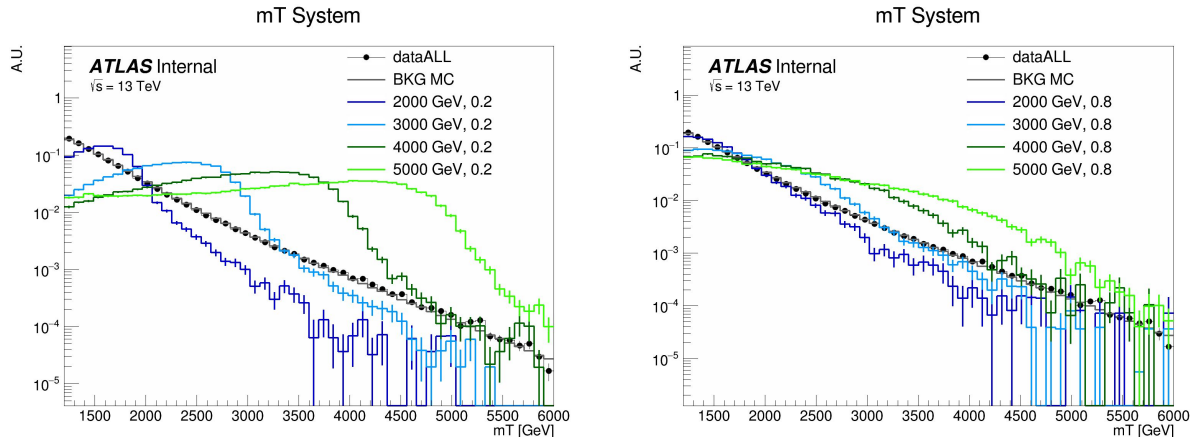


Figure 8.9: The resonant shape of the SVJ signals in m_T , in contrast to the smoothly falling m_T background. The high R_{inv} signals (right) boast a wider shape, making them more difficult to detect, while the low R_{inv} signals (left) produce a more narrow resonance in m_T .

1688
 1689 The SM background in the SR is predominantly composed of QCD events, and due to the poor
 1690 modeling of QCD at high energies by MC, it is estimated in a fully data-driven way. An empirical
 1691 functional form is used for the background shape of m_T . The ability of this function to model
 1692 the background behavior is tested both the CR and the VR for each analysis strategy. The shape

1693 parameters are left free in all the fits.

1694 The fits are performed for $1500 \text{ GeV} < m_T < 6000 \text{ GeV}$. The polynomial chosen is a standard
1695 5-parameter function used in several similar dijet search analyses such as [76] [77] [78] and shown
1696 in Equation 8.2:

$$f(x) = p_1(1 - x)^{p_2}x^{p_3+p_4\ln x+p_5\ln^2 x} \quad (8.2)$$

1697 Here $x = m_{jj}/\sqrt{s}$ and the p_i are free parameters. The fit function is required to be fully positive, and
1698 the m_T distribution is fit to 90 even-width bins. The resulting fit shape is used as the background
1699 estimation for both the SVJ Fit strategy and the Discovery strategy. Validation of the fit and its
1700 ability to both model the background and detect signal are shown in Section 8.5. Higher order
1701 polynomials were also considered, but an F-test was performed and the five parameter function
1702 was determined to be adequate and optimal for capturing the shape of the background.

1703 **8.5 Fit Strategy and Validation**

1704 The steps taken to validate the fitting approach for both the SVJ Fit strategy and the Discovery
1705 strategy will be outlined in the following sections. The signal region fits which comprise the final
1706 result will be presented in Chapter 9.

1707 **8.5.1 SVJ Fit Strategy**

1708 The ability of the five parameter fit function to capture the shape of the background is studied
1709 extensively, using data from the CR and VR. Signal injection tests are performed to determine the
1710 ability of the fit to recover and quantify any SVJ signal excess. Estimates of the expected sensitivity
1711 and the ability to set upper limits on the cross-section of the signal process are also verified.

1712 **Background Only Fits**

1713 Three validations are used for the background fit polynomial: MC across all analysis regions,
1714 data in the CR and VR, and pseudo-data in the CR and VR.

1715 Figure 8.10 shows the ability of this polynomial to fit the smoothly falling m_T background in
 1716 simulation across all 3 analysis regions (CR, VR, SR). The m_T spectrum is fit in 90 even bins.
 1717 These distributions are obtained by downsampling the MC statistics to match the relevant statis-
 1718 tics of the data region, in accordance with the MC weights. The high background-only p -value
 indicates a good fit.

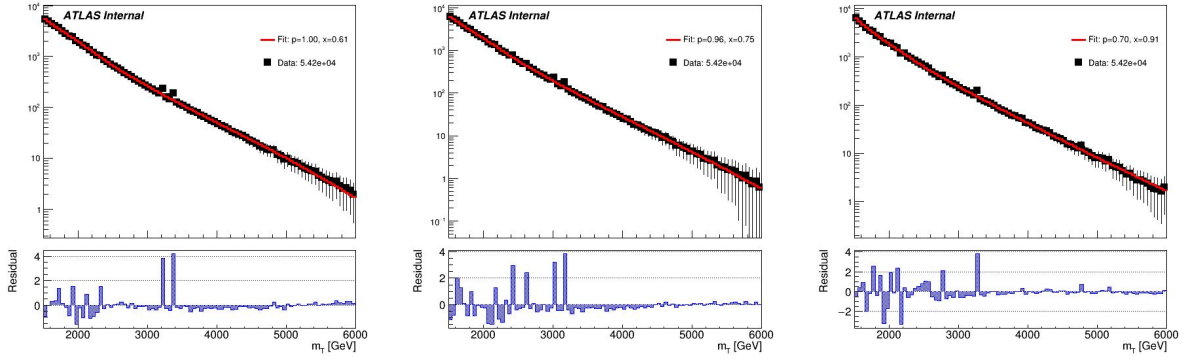


Figure 8.10: Background-only m_T fits using representative MC in the CR (left), VR (middle), and SR (right).

1719
 1720 A slight sinusoidal pattern in the residuals may be observed. This arises due to the “stitching”
 1721 of the p_T slices for the QCD MC (as shown in Figure 6.1), which is picked up by the fit. For this
 1722 reason, fitting to MC is only checked to verify that the differences in the slope of m_T between the
 1723 three regions (as shown in Figure 8.7) do not pose a problem for the fitting strategy.

1724 The nature of the functional fitting method allows it to easily adapt to changes in slope of a
 1725 smoothly falling distribution. Thus validation of the fit can be performed in data using the CR and
 1726 the VR distributions to model the expected behavior in the SR. Figure 8.11 shows the a successful
 1727 fit performed on the full statistics CR and VR regions.

1728 Figure 8.12 shows the post-fit values of the fit parameters and their uncertainties for each fit.

1729 To further validate the fit stability of the fit against potential statistical fluctuations, *pseudo-data*
 1730 (also known as *toy datasets*) are created from the CR data distribution. The pseudo-data is created
 1731 following an *Asimov* prescription [79], using a template to generate a set of toys representing
 1732 different possible statistical fluctuations. When studied as a group, the performance of the pseudo-
 1733 data collection represents the range of possible behavior for an unknown distribution (the SR data

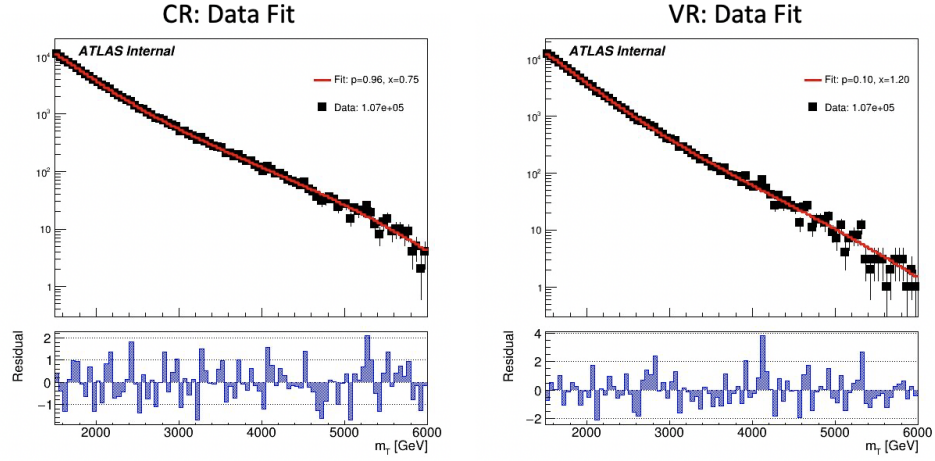


Figure 8.11: Background-only m_T fits using data in the full statistics CR and VR regions.

Parameter	CR		VR	
	Value	Error	Value	Error
p1	1.0716e+05	4.64e+02	1.0686e+05	4.63e+02
p2	4.2479e+01	2.97e+00	3.4279e+01	3.71e+00
p3	5.3888e+01	3.81e+00	4.0798e+01	4.50e+00
p4	2.3804e+01	1.47e+00	1.9424e+01	1.71e+00
p5	3.6683e+00	2.18e-01	3.1583e+00	2.51e-01

Figure 8.12: Post-fit parameters for the PFN CR and VR. p_1 can also be considered N_{bkg} or the normalization factor.

1734 in this case), given its statistical uncertainties.

1735 The template used to generate the pseudo-data is a *smoothed* and *scaled* version of the CR.

1736 The smoothing applied follows the procedure for functional decomposition described in Ref. [80].

Figure 8.13 shows the impact of smoothing on the source data distribution in the CR.

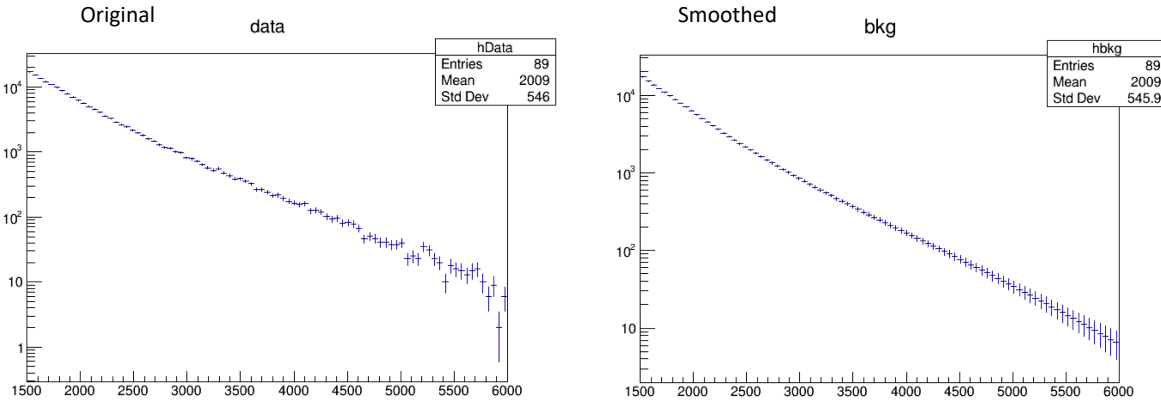


Figure 8.13: m_T distribution in the data CR, before (left) and after (right) smoothing.

1737

1738 The scaling adjusts the statistics of the smoothed template to the expected statistics of the SR.

1739 Recall Figure 8.8, which illustrates that the statistics of the CR and the VR are almost 3x the

1740 expected statistics of the SR. The polynomial fitting strategy is sensitive to the statistics of the

1741 fitted template, so its performance can very substantially depending on the statistical power of the

1742 fitted distribution. To mitigate this, the smoothed template is scaled to the expected statistics of

1743 the SR. Toys are then generated from the smoothed distribution, by varying each bin within its

1744 statistical uncertainty according to a Poisson distribution. Each toy has the same statistical power

1745 as the SR, within statistical uncertainty.

1746 Figure 8.14 shows example fits to three such toy datasets. Figure 8.15 shows the resulting

1747 p-values after an ensemble of 100 Asimov pseudo-datasets are each individually fit. This test

1748 determines the likelihood of exceptionally good (high p-value) or poor (low p-value) fits due to

1749 randoms statistical fluctuations in the data. A flat distribution is observed, indicating good statisti-

1750 cal behavior.

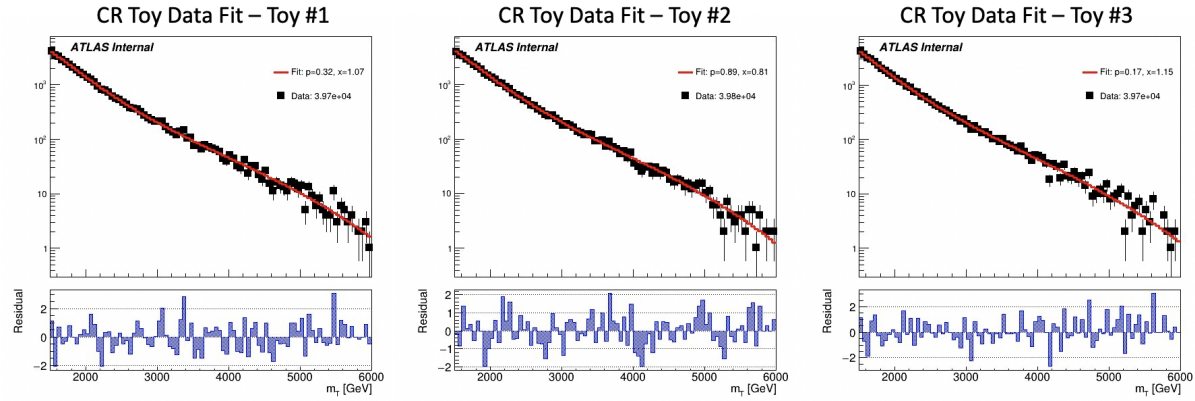


Figure 8.14: Background-only m_T fits using pseudo-data from the CR template.

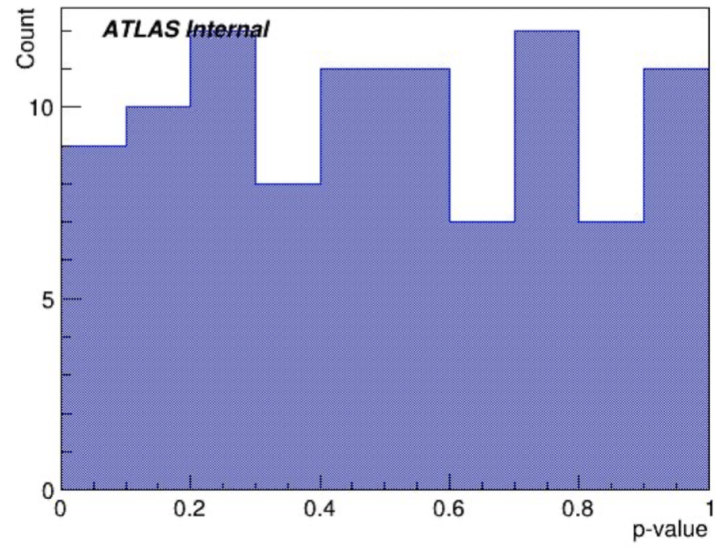


Figure 8.15: p -value histograms from 100 fits to Asimov data in the CR.

1751 **Signal + Background Fits**

1752 Figure 8.16 shows an example of an injected signal into the exclusion region m_T spectrum, and
the ability of the fit framework to accurately fit the number of signal events.

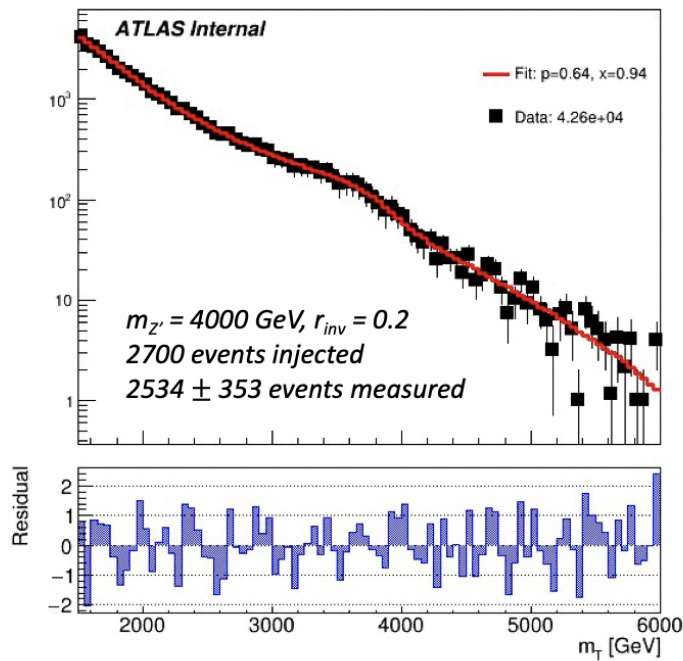


Figure 8.16: Example S+B fit on a background m_T spectrum with injected signal from the point (4000 GeV , $R_{inv}=0.2$).

1753

1754 Signal injection tests demonstrate the a linear relationship between the amount of signal in-
1755 jected and the amount of signal measured by the fit. The signal injection tests are performed in
1756 Asimov datasets to counter the impact of statistical fluctuations in any given template. 50 Asimov
1757 trials are run for all signal points across Z' mass and R_{inv} .

1758 Figure 8.17 provides the results of these tests. The uncertainty of the measurement varies
1759 according to the Z' mass, due to the larger relative background for lower mass points. However,
1760 a strong linear relationship between amount of signal injected and amount of signal measured is
1761 observed for all signal points, which is the key feature.

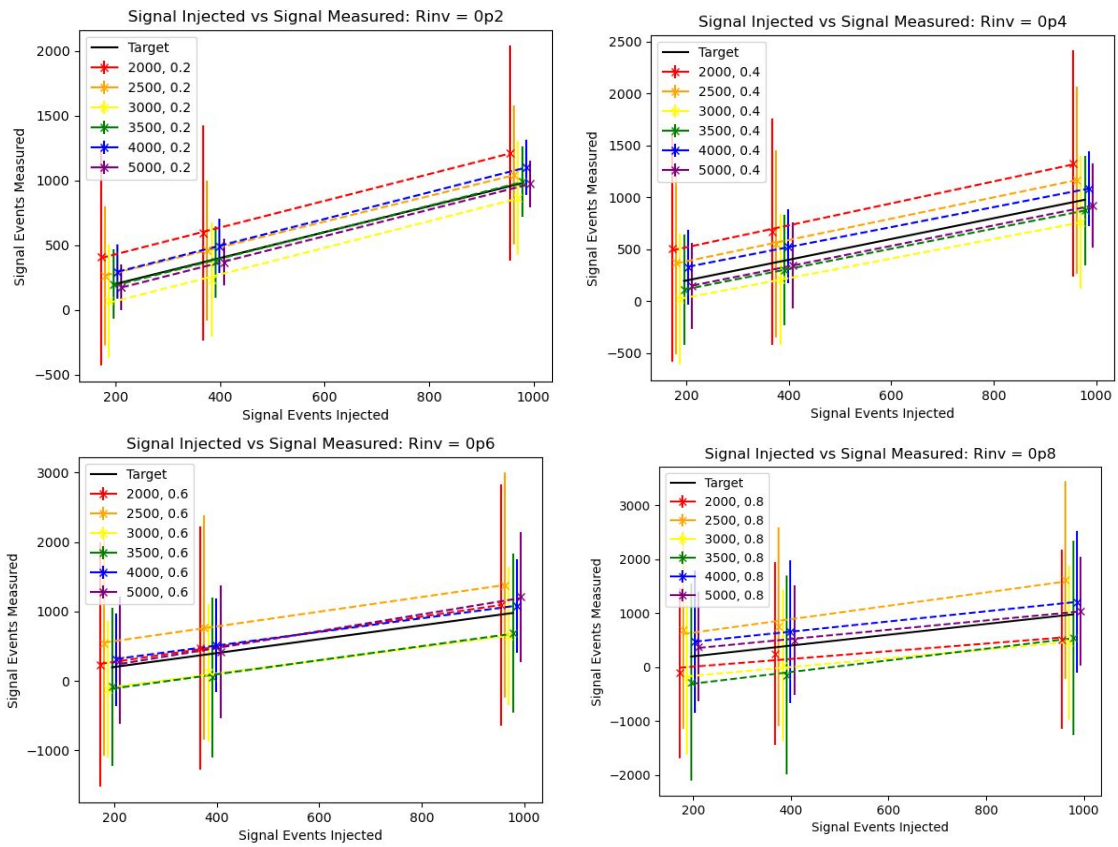


Figure 8.17: Measured signal at a variety of injected values ($1x$, $2x$, and $5x\sqrt{b}$), for all signal points in the grid, $R_{inv}=0.2$ (top left), 0.4 (top right), 0.6 (bottom left), and 0.8 (bottom right).

1762 **Expected Sensitivity**

1763 Limits on the signal process are obtained by determining the cross section of the signal that can
 1764 be excluded to 95% confidence. Figure 8.18 shows the expected limits obtained from an average
 1765 of 50 Asimov data fits. The limits shown do not include systematics uncertainties in the fit, the
 1766 impacts of which are discussed in Chapter 9.

1767 Considerable exclusion power is predicted for low R_{inv} signal points and lower mass points.
 1768 Higher R_{inv} points present more difficulty due to the very broad signal bump. Higher Z' mass
 1769 points are more difficult to exclude due to the low theory cross-sections.

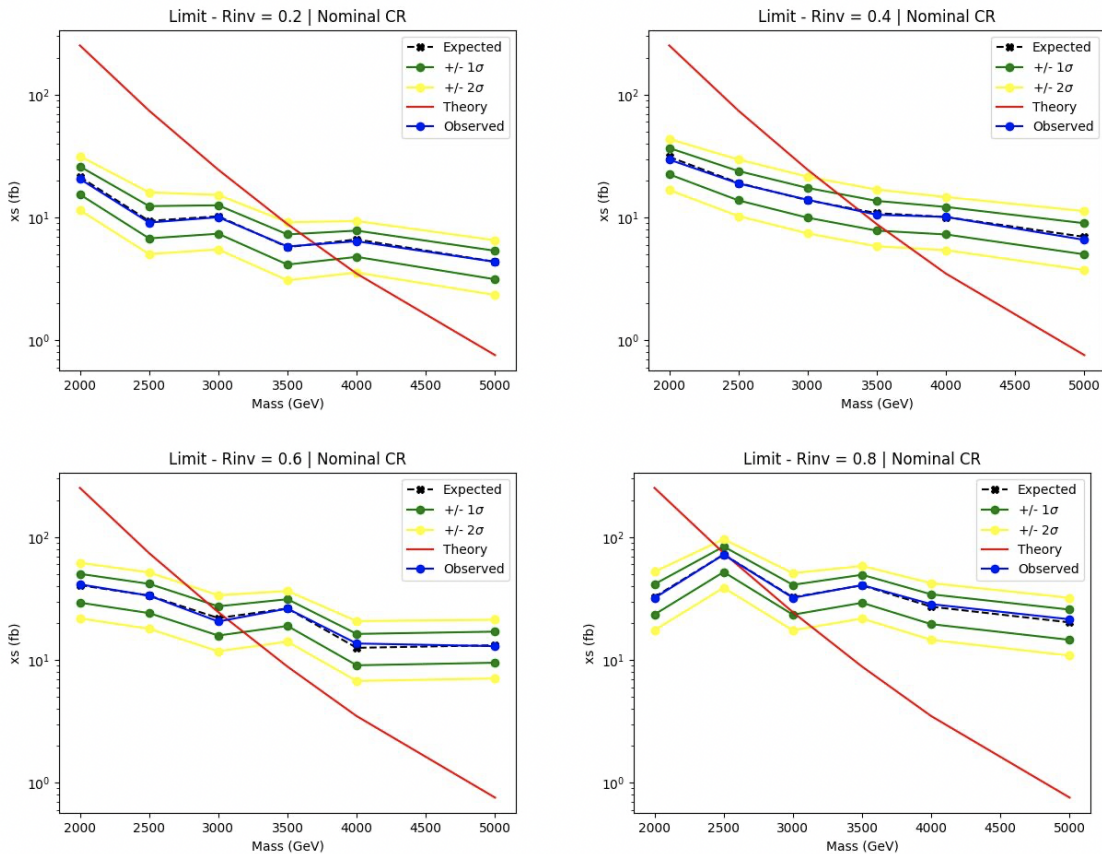


Figure 8.18: 95% C.L. upper limits for signal models across Z' mass, for four different R_{inv} fractions, from the CR region (without systematics). TODO - ATLAS style

1770 The ability of the fit to identify a significant excess is tested by calculating the limits on
 1771 signal injected toys. 2σ and 5σ of signal is injected for each signal point into 50 Asimov data

1772 toys. Figure 8.19 demonstrates the impact of this signal injection on the limit for $R_{inv} = 0.2$.
 1773 The observed limit rises as more signal is injected, indicating the ability of the fit to identify a
 1774 significant signal excess.

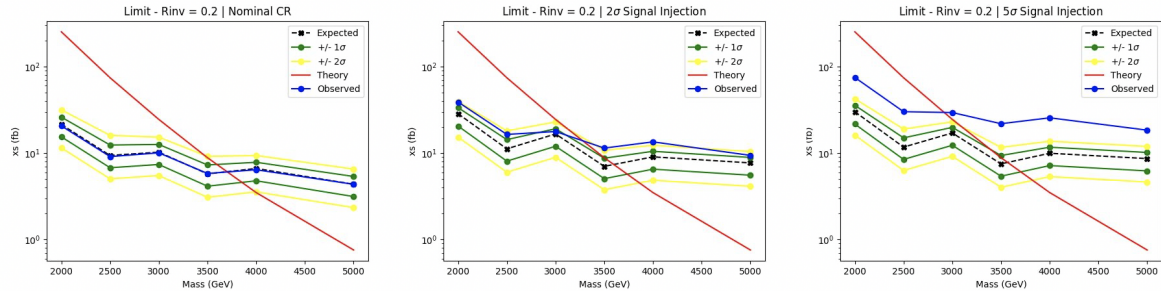


Figure 8.19: 95% C.L. upper limits and observed limit for signal models across Z' mass, with varying amounts of signal injected. TODO - ATLAS style

1775 8.5.2 Discovery Strategy

1776 Model-independent fits for the discovery region are performed using PYBUMPHUNTER [74].
 1777 The strategy consists of comparing the data in a given m_T spectrum of interest to a background
 1778 estimation derived by performing the polynomial fit and sampling from the post-fit function into a
 1779 histogram.

1780 The polynomial fit is done to an m_T distribution with 180 bins (25 GeV wide), half the width
 1781 of the fits in the SVJ Fit region (50 GeV wide). The narrower bins allow for rebinning based on
 1782 the *signal mass resolution* of the SVJ signals. The binning strategy is outlined in Appendix D.1.

1783 Figure 8.20 shows the fit and residuals with of the polynomial with the narrower binning in the
 1784 CR and the Discovery VR data. Figure 8.21 shows the post-fit values of the fit parameters and their
 1785 uncertainties for the CR and VR. These results indicate good ability of the 5-parameter polynomial
 1786 to model the ANTELOPE selected data.

1787 The studies shown in Section 8.5.1 validate the robustness of the background polynomial fit.
 1788 The narrower bins are the only difference for polynomial fitting between the SVJ Fit and Discovery
 1789 Fit strategies, and they are not observed to reduce the quality or consistency of the fit.

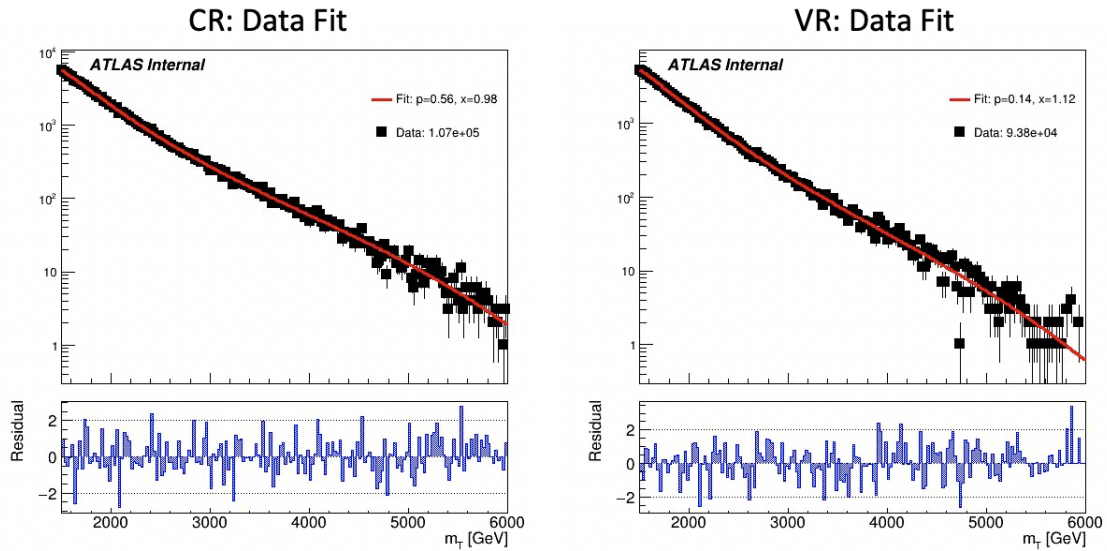


Figure 8.20: Post-fit function and residuals for the ANTELOPE CR and VR.

Parameter	CR		VR	
	Value	Error	Value	Error
p1	1.0709e+05	4.65e+02	9.3776e+04	4.34e+02
p2	4.5945e+01	3.03e+00	4.5787e+01	3.78e+00
p3	5.8566e+01	3.88e+00	5.6014e+01	4.58e+00
p4	2.5593e+01	1.50e+00	2.4914e+01	1.73e+00
p5	3.9196e+00	2.22e-01	3.8809e+00	2.53e-01

Figure 8.21: Post-fit parameters for the ANTELOPE CR and VR.

1790 **BumpHunter Fits**

1791 The signal mass resolution binning strategy described in Appendix D.1 creates a monotonically
1792 increasing set of bins. While the SVJ signals help inform the binning, the binning is still broadly
1793 applicable to a variety of potential signal models. The mass resolution of any resonant signal
1794 generally widens as the mass of the mediator particle increases. A similar strategy and binning
1795 was used in the generic heavy resonance search presented in Ref. [73]. The resulting set of 15 bins
1796 to be used in the BumpHunter fits varies in width from 100 GeV at the m_T core to 925 GV in the
1797 m_T tail.

1798 Figure 8.22 shows the result of running BumpHunter over the rebinned CR and VR m_T spectra.
1799 The background estimation is given by polynomial fit function. The high p-values (>0.01) indicate
good agreement with the background estimation.

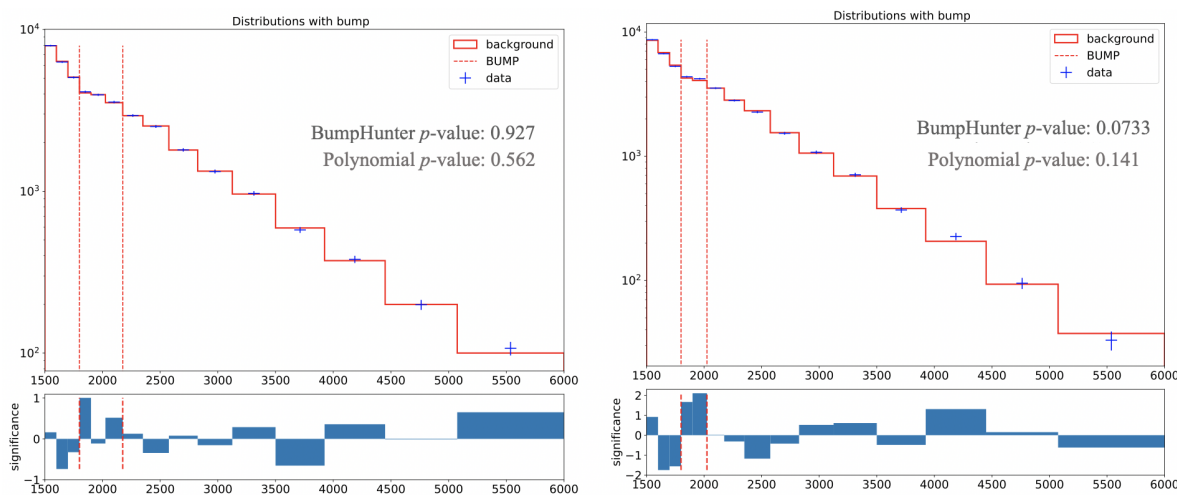


Figure 8.22: BumpHunter fits on the ANTELOPE m_T spectra for both the CR (left) and VR (right). In a signal-depleted region, good agreement with the background estimation is observed.

1800
1801 Figure 8.23 shows BumpHunter p-values over 100 Asimov trials, where each toy is scaled to
1802 the statistics of the SR. The agreement is generally very good, as the p-values trend towards higher
1803 values. No fits with a *spurious signal* are found. A spurious signal would be indicated by a fit with
1804 a p-value < 0.01 , indicating a bump of at least 2σ significance.

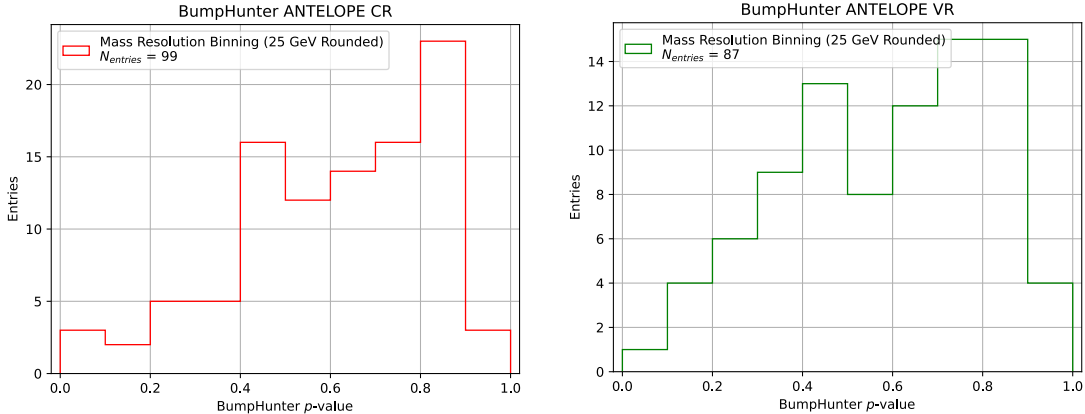


Figure 8.23: BumpHunter p-values extracted for 100 Asimov toys for both the ANTELOPE CR (left) and VR (right).

1805 BumpHunter Signal Injection

1806 To explore a model independent signal hypothesis, signal injection tests in the ANTELOPE re-
 1807 gion are done with generic Gaussian shapes. Two Gaussian models are built with a mean ranging
 1808 from 2000 GeV to 5000 GeV and a standard deviation equal to 10 or 20% the mean value. Fig-
 1809 ure 8.24 illustrates an injected Gaussian and its effect on the m_T distribution. The 20% gaussian
 1810 represents the widest possible signals we might be sensitive to with a BH strategy, while the 10%
 1811 injection represents a narrower signal peak.

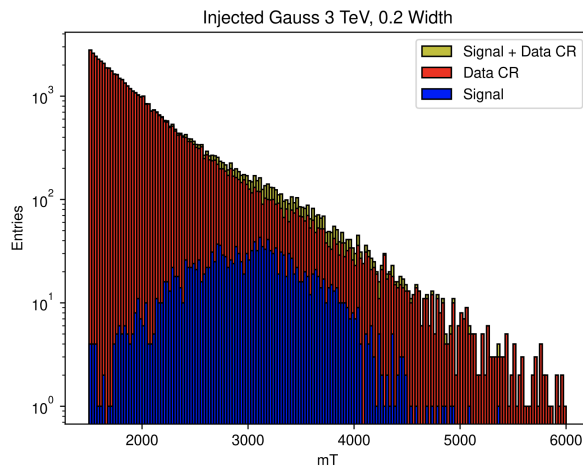


Figure 8.24: Example injected gaussian signal.

1812 An estimated 5σ of signal is injected for these tests. The estimate is derived from the polyno-

1813 mial fitting framework, and is therefore an underestimate, as the flexibility of the polynomial fit
1814 absorbs some of the signal. Therefore we do not expect to measure 5σ significance with the BH
1815 approach, but rather hope to see that some level of signal (at least $\geq 2\sigma$ significance) is observed
1816 by the BumpHunter framework.

1817 Results are obtained by averaging over 100 toys for each injection. Figure 8.25 shows the
1818 resulting max local significance (in an m_T bin) and the location of the determined bump, indicating
1819 a good response of the BumpHunter framework for detecting generic m_T resonances at the right
1820 location. Only the 5000 GeV 20% width point is not properly identified by the framework. While
1821 some sensitivity is lost due to the flexible nature of the fitting framework, the ability to identify a
1822 bump with substantial local significance in the correct location is observed. Figure 8.26 shows an
1823 example of the identified bump.

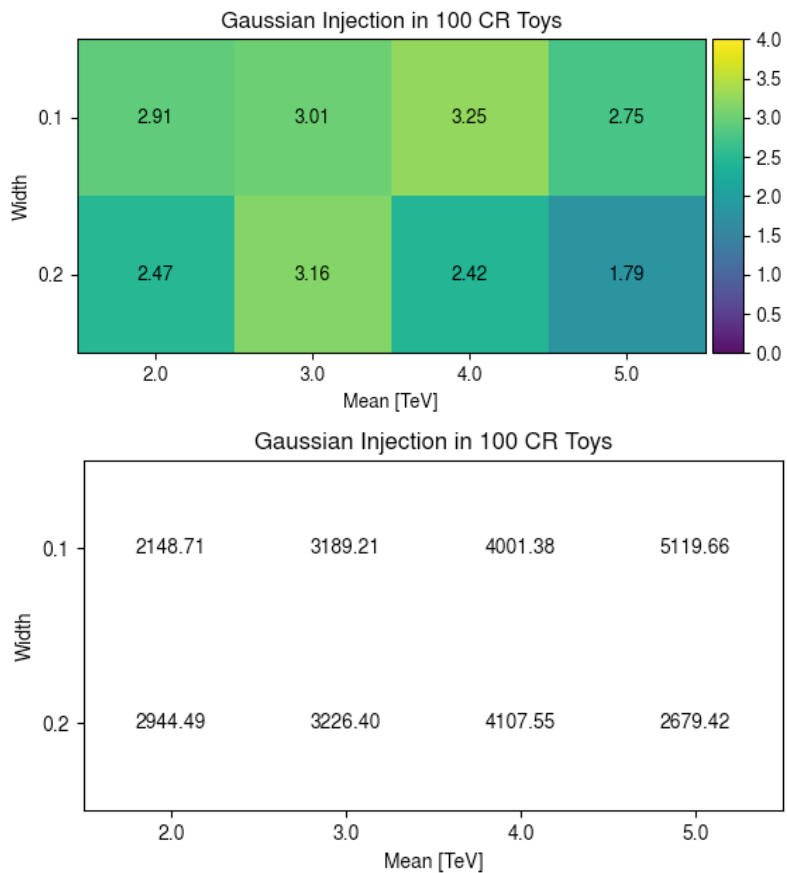


Figure 8.25: Response of the BumpHunter framework to signal injection of 5σ significance to the model-dependent polynomial fit framework. The local significance (top) and bump location (bottom) are shown.

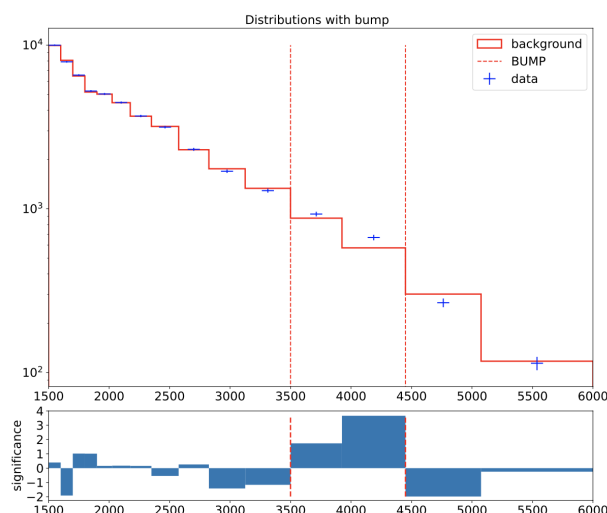


Figure 8.26: Example BH response to gaussian signal injection at 4000 GeV with width of 10%.

1824

1825

Chapter 9: Results

1826

Conclusion or Epilogue

1827 Use this page for your epilogue or conclusion if applicable; please use only one of the titles
1828 for this page. Otherwise, you may delete it. Use this page for your epilogue or conclusion if
1829 applicable; please use only one of the titles for this page. Otherwise, you may delete it. Use this
1830 page for your epilogue or conclusion if applicable; please use only one of the titles for this page.
1831 Otherwise, you may delete it. Use this page for your epilogue or conclusion if applicable; please
1832 use only one of the titles for this page. Otherwise, you may delete it. Use this page for your
1833 epilogue or conclusion if applicable; please use only one of the titles for this page. Otherwise,
1834 you may delete it. Use this page for your epilogue or conclusion if applicable; please use only one
1835 of the titles for this page. Otherwise, you may delete it. Use this page for your epilogue or
1836 conclusion if applicable; please use only one of the titles for this page. Otherwise, you may delete
1837 it. Use this page for your epilogue or conclusion if applicable; please use only one of the titles for
1838 this page. Otherwise, you may delete it. Use this page for your epilogue or conclusion if
1839 applicable; please use only one of the titles for this page. Otherwise, you may delete it. Use this
1840 page for your epilogue or conclusion if applicable; please use only one of the titles for this page.
1841 Otherwise, you may delete it. Use this page for your epilogue or conclusion if applicable; please
1842 use only one of the titles for this page. Otherwise, you may delete it. Use this page for your
1843 epilogue or conclusion if applicable; please use only one of the titles for this page. Otherwise,
1844 you may delete it. Use this page for your epilogue or conclusion if applicable; please use only one
1845 of the titles for this page. Otherwise, you may delete it. Use this page for your epilogue or
1846 conclusion if applicable; please use only one of the titles for this page. Otherwise, you may delete

1847 it. Use this page for your epilogue or conclusion if applicable; please use only one of the titles for
1848 this page. Otherwise, you may delete it. Use this page for your epilogue or conclusion if
1849 applicable; please use only one of the titles for this page. Otherwise, you may delete it. Use this
1850 page for your epilogue or conclusion if applicable; please use only one of the titles for this page.
1851 Otherwise, you may delete it. Use this page for your epilogue or conclusion if applicable; please
1852 use only one of the titles for this page. Otherwise, you may delete it. Use this page for your
1853 epilogue or conclusion if applicable; please use only one of the titles for this page. Otherwise,
1854 you may delete it. Use this page for your epilogue or conclusion if applicable; please use only one
1855 of the titles for this page. Otherwise, you may delete it. Use this page for your epilogue or
1856 conclusion if applicable; please use only one of the titles for this page. Otherwise, you may delete
1857 it. Use this page for your epilogue or conclusion if applicable; please use only one of the titles for
1858 this page. Otherwise, you may delete it. Use this page for your epilogue or conclusion if
1859 applicable; please use only one of the titles for this page. Otherwise, you may delete it. Use this
1860 page for your epilogue or conclusion if applicable; please use only one of the titles for this page.
1861 Otherwise, you may delete it. Use this page for your epilogue or conclusion if applicable; please
1862 use only one of the titles for this page. Otherwise, you may delete it. Use this page for your
1863 epilogue or conclusion if applicable; please use only one of the titles for this page. Otherwise,
1864 you may delete it. Use this page for your epilogue or conclusion if applicable; please use only one
1865 of the titles for this page. Otherwise, you may delete it. Use this page for your epilogue or
1866 conclusion if applicable; please use only one of the titles for this page. Otherwise, you may delete
1867 it. Use this page for your epilogue or conclusion if applicable; please use only one of the titles for
1868 this page. Otherwise, you may delete it. Use this page for your epilogue or conclusion if
1869 applicable; please use only one of the titles for this page. Otherwise, you may delete it. Use this
1870 page for your epilogue or conclusion if applicable; please use only one of the titles for this page.
1871 Otherwise, you may delete it. Use this page for your epilogue or conclusion if applicable; please
1872 use only one of the titles for this page. Otherwise, you may delete it. Use this page for your
1873 epilogue or conclusion if applicable; please use only one of the titles for this page. Otherwise,

1874 you may delete it. Use this page for your epilogue or conclusion if applicable; please use only one
1875 of the titles for this page. Otherwise, you may delete it. Use this page for your epilogue or
1876 conclusion if applicable; please use only one of the titles for this page. Otherwise, you may delete
1877 it. Use this page for your epilogue or conclusion if applicable; please use only one of the titles for
1878 this page. Otherwise, you may delete it. Use this page for your epilogue or conclusion if
1879 applicable; please use only one of the titles for this page. Otherwise, you may delete it. Use this
1880 page for your epilogue or conclusion if applicable; please use only one of the titles for this page.
1881 Otherwise, you may delete it. Use this page for your epilogue or conclusion if applicable; please
1882 use only one of the titles for this page. Otherwise, you may delete it. Use this page for your
1883 epilogue or conclusion if applicable; please use only one of the titles for this page. Otherwise,
1884 you may delete it. Use this page for your epilogue or conclusion if applicable; please use only one
1885 of the titles for this page. Otherwise, you may delete it. Use this page for your epilogue or
1886 conclusion if applicable; please use only one of the titles for this page. Otherwise, you may delete
1887 it. Use this page for your epilogue or conclusion if applicable; please use only one of the titles for
1888 this page. Otherwise, you may delete it. Use this page for your epilogue or conclusion if
1889 applicable; please use only one of the titles for this page. Otherwise, you may delete it. Use this
1890 page for your epilogue or conclusion if applicable; please use only one of the titles for this page.
1891 Otherwise, you may delete it. Use this page for your epilogue or conclusion if applicable; please
1892 use only one of the titles for this page. Otherwise, you may delete it. Use this page for your
1893 epilogue or conclusion if applicable; please use only one of the titles for this page. Otherwise,
1894 you may delete it. Use this page for your epilogue or conclusion if applicable; please use only one
1895 of the titles for this page. Otherwise, you may delete it. Use this page for your epilogue or
1896 conclusion if applicable; please use only one of the titles for this page. Otherwise, you may delete
1897 it. Use this page for your epilogue or conclusion if applicable; please use only one of the titles for
1898 this page. Otherwise, you may delete it. Use this page for your epilogue or conclusion if
1899 applicable; please use only one of the titles for this page. Otherwise, you may delete it. Use this
1900 page for your epilogue or conclusion if applicable; please use only one of the titles for this page.

1901 Otherwise, you may delete it. Use this page for your epilogue or conclusion if applicable; please
1902 use only one of the titles for this page. Otherwise, you may delete it. Use this page for your
1903 epilogue or conclusion if applicable; please use only one of the titles for this page. Otherwise,
1904 you may delete it. Use this page for your epilogue or conclusion if applicable; please use only one
1905 of the titles for this page. Otherwise, you may delete it. Use this page for your epilogue or
1906 conclusion if applicable; please use only one of the titles for this page. Otherwise, you may delete
1907 it. Use this page for your epilogue or conclusion if applicable; please use only one of the titles for
1908 this page. Otherwise, you may delete it. Use this page for your epilogue or conclusion if
1909 applicable; please use only one of the titles for this page. Otherwise, you may delete it. Use this
1910 page for your epilogue or conclusion if applicable; please use only one of the titles for this page.
1911 Otherwise, you may delete it. Use this page for your epilogue or conclusion if applicable; please
1912 use only one of the titles for this page. Otherwise, you may delete it. Use this page for your
1913 epilogue or conclusion if applicable; please use only one of the titles for this page. Otherwise,
1914 you may delete it. Use this page for your epilogue or conclusion if applicable; please use only one
1915 of the titles for this page. Otherwise, you may delete it. Use this page for your epilogue or
1916 conclusion if applicable; please use only one of the titles for this page. Otherwise, you may delete
1917 it. Use this page for your epilogue or conclusion if applicable; please use only one of the titles for
1918 this page. Otherwise, you may delete it. Use this page for your epilogue or conclusion if
1919 applicable; please use only one of the titles for this page. Otherwise, you may delete it. Use this
1920 page for your epilogue or conclusion if applicable; please use only one of the titles for this page.
1921 Otherwise, you may delete it. Use this page for your epilogue or conclusion if applicable; please
1922 use only one of the titles for this page. Otherwise, you may delete it. Use this page for your
1923 epilogue or conclusion if applicable; please use only one of the titles for this page. Otherwise,
1924 you may delete it. Use this page for your epilogue or conclusion if applicable; please use only one
1925 of the titles for this page. Otherwise, you may delete it. Use this page for your epilogue or
1926 conclusion if applicable; please use only one of the titles for this page. Otherwise, you may delete
1927 it.

References

- [1] Jens Erler and Paul Langacker. “Electroweak model and constraints on new physics”. In: (July 2004). arXiv: hep-ph/0407097.
- [2] David J Griffiths. *Introduction to elementary particles; 2nd rev. version*. Physics textbook. New York, NY: Wiley, 2008.
- [3] M. Tanabashi et al. “Review of Particle Physics”. In: *Phys. Rev. D* 98 (3 2018), pp. 847–851.
- [4] E. Noether. “Invariante Variationsprobleme”. In: *Nachr. d. König. Gesellsch. d. Wiss. zu Göttingen, Math-phys. Klasse*, Seite 235–157 (1918). eprint: www.physics.ucla.edu/\~\cwp/articles/noether.trans/german/emmy235.html.
- [5] J. H. Christenson et al. “Evidence for the 2π Decay of the K_2^0 Meson”. In: *Phys. Rev. Lett.* 13 (1964), pp. 138–140.
- [6] Michael Gronau. “CP Violation in B Meson Decays”. In: *Nuclear Physics B - Proceedings Supplements* 142 (May 2005), 263–270.
- [7] J. E. Augustin et al. “Discovery of a Narrow Resonance in e^+e^- Annihilation”. In: *Phys. Rev. Lett.* 33 (1974), pp. 1406–1408.
- [8] J. J. Aubert et al. “Experimental Observation of a Heavy Particle J ”. In: *Phys. Rev. Lett.* 33 (1974), pp. 1404–1406.
- [9] Martin L. Perl et al. “Evidence for Anomalous Lepton Production in $e^+ - e^-$ Annihilation”. In: *Phys. Rev. Lett.* 35 (1975), pp. 1489–1492.
- [10] S. W. Herb et al. “Observation of a Dimuon Resonance at 9.5-GeV in 400-GeV Proton-Nucleus Collisions”. In: *Phys. Rev. Lett.* 39 (1977), pp. 252–255.
- [11] F. Abe et al. “Observation of top quark production in $\bar{p}p$ collisions”. In: *Phys. Rev. Lett.* 74 (1995), pp. 2626–2631. arXiv: hep-ex/9503002.
- [12] S. Abachi et al. “Observation of the top quark”. In: *Phys. Rev. Lett.* 74 (1995), pp. 2632–2637. arXiv: hep-ex/9503003.
- [13] K. Kodama et al. “Observation of tau neutrino interactions”. In: *Phys. Lett. B* 504 (2001), pp. 218–224. arXiv: hep-ex/0012035.

- 1955 [14] G. Arnison et al. “Experimental Observation of Lepton Pairs of Invariant Mass Around 95-
 1956 GeV/c**2 at the CERN SPS Collider”. In: *Phys. Lett. B* 126 (1983), pp. 398–410.
- 1957 [15] P. Bagnaia et al. “Evidence for $Z^0 \rightarrow e^+e^-$ at the CERN $\bar{p}p$ Collider”. In: *Phys. Lett. B* 129
 1958 (1983), pp. 130–140.
- 1959 [16] Serguei Chatrchyan et al. “Observation of a New Boson at a Mass of 125 GeV with the
 1960 CMS Experiment at the LHC”. In: *Phys. Lett. B* 716 (2012), pp. 30–61. arXiv: 1207.7235
 1961 [hep-ex].
- 1962 [17] Georges Aad et al. “Observation of a new particle in the search for the Standard Model
 1963 Higgs boson with the ATLAS detector at the LHC”. In: *Phys. Lett. B* 716 (2012), pp. 1–29.
 1964 arXiv: 1207.7214 [hep-ex].
- 1965 [18] K. G. Begeman, A. H. Broeils, and R. H. Sanders. “Extended rotation curves of spiral galaxies:
 1966 Dark haloes and modified dynamics”. In: *Mon. Not. Roy. Astron. Soc.* 249 (1991), p. 523.
- 1967 [19] Y. Ashie et al. “Evidence for an oscillatory signature in atmospheric neutrino oscillation”.
 1968 In: *Phys. Rev. Lett.* 93 (2004), p. 101801. arXiv: hep-ex/0404034.
- 1969 [20] C. Abel et al. “Measurement of the Permanent Electric Dipole Moment of the Neutron”. In:
 1970 *Phys. Rev. Lett.* 124.8 (2020), p. 081803. arXiv: 2001.11966 [hep-ex].
- 1971 [21] Guillaume Albouy et al. “Theory, phenomenology, and experimental avenues for dark showers:
 1972 a Snowmass 2021 report”. In: *The European Physical Journal C* 82.12 (Dec. 2022).
- 1973 [22] Timothy Cohen et al. “LHC searches for dark sector showers”. In: *Journal of High Energy
 1974 Physics* 2017.11 (Nov. 2017).
- 1975 [23] Lyndon Evans and Philip Bryant. “LHC Machine”. In: *Journal of Instrumentation* 3.08
 1976 (2008), S08001.
- 1977 [24] “The ATLAS Experiment at the CERN Large Hadron Collider”. In: *JINST* 3 (2008). Also
 1978 published by CERN Geneva in 2010, S08003.
- 1979 [25] “The CMS experiment at the CERN LHC”. In: *Journal of Instrumentation* 3.08 (2008),
 1980 S08004.
- 1981 [26] “The ALICE experiment at the CERN LHC”. In: *Journal of Instrumentation* 3.08 (2008),
 1982 S08002.
- 1983 [27] “The LHCb Detector at the LHC”. In: *Journal of Instrumentation* 3.08 (2008), S08005.
- 1984 [28] Ana Lopes and Melissa Loyse Perrey. *FAQ-LHC The guide*. 2022.

- 1985 [29] Esma Mobs. “The CERN accelerator complex in 2019. Complexe des accélérateurs du
1986 CERN en 2019”. In: (2019). General Photo.
- 1987 [30] *Pulling together: Super Conducting electromagnets*. <https://home.cern/science/engineering/pulling-together-superconducting-electromagnets>.
1988 Accessed: 2024-01-05.
1989
- 1990 [31] *The High-Luminosity LHC*. <https://voisins.web.cern.ch/en/high-luminosity-lhc-hl-lhc>. Accessed: 2024-01-05.
1991
- 1992 [32] Aad G., et al. (ATLAS Collaboration and CMS Collaboration). “Combined Measurement of
1993 the Higgs Boson Mass in pp Collisions at $\sqrt{s} = 7$ and 8 TeV with the ATLAS and CMS
1994 Experiments”. In: *Phys. Rev. Lett.* 114 (19 2015), p. 191803.
- 1995 [33] O. Aberle et al. *High-Luminosity Large Hadron Collider (HL-LHC): Technical design re-
1996 port*. CERN Yellow Reports: Monographs. Geneva: CERN, 2020.
- 1997 [34] The ATLAS Collaboration. “The ATLAS Experiment at the CERN Large Hadron Collider”.
1998 In: *Journal of Instrumentation* 3.08 (2008), S08003.
- 1999 [35] G Aad, B Abbott, and ATLAS Collaboration. “Performance of the reconstruction of large
2000 impact parameter tracks in the inner detector of ATLAS”. In: *Eur. Phys. J. C Part. Fields*
2001 83.11 (Nov. 2023).
- 2002 [36] Joao Pequenao. *Computer Generated image of the ATLAS calorimeter*. 2008.
- 2003 [37] *ATLAS liquid-argon calorimeter: Technical Design Report*. Technical design report. AT-
2004 LAS. Geneva: CERN, 1996.
- 2005 [38] H A Gordon. “Liquid argon calorimetry for the SSC”. In: () .
- 2006 [39] Henric Wilkens and (on behalf of the ATLAS LArg Collaboration). “The ATLAS Liquid
2007 Argon calorimeter: An overview”. In: *Journal of Physics: Conference Series* 160.1 (2009),
2008 p. 012043.
- 2009 [40] *Technical Design Report for the Phase-II Upgrade of the ATLAS Tile Calorimeter*. Tech.
2010 rep. Geneva: CERN, 2017.
- 2011 [41] “Technical Design Report for the Phase-II Upgrade of the ATLAS Muon Spectrometer”. In:
2012 () .
- 2013 [42] L Pontecorvo. “The ATLAS Muon Spectrometer”. In: (2004). revised version number 1
2014 submitted on 2003-07-27 16:31:16.

- 2015 [43] *ATLAS magnet system: Technical Design Report, 1*. Technical design report. ATLAS. Geneva:
2016 CERN, 1997.
- 2017 [44] 2024.
- 2018 [45] Tommaso Colombo. “Data-flow Performance Optimisation on Unreliable Networks: the AT-
2019 LAS Data-Acquisition Case”. In: *Journal of Physics: Conference Series* 608 (May 2015),
2020 p. 012005.
- 2021 [46] Joao Pequenao. “Event Cross Section in a computer generated image of the ATLAS detec-
2022 tor.” 2008.
- 2023 [47] ATLAS Collaboration. “ATLAS Experiment Implements Heterogeneous Particle Recon-
2024 struction with Intel oneAPI Tools”. General Photo. 2023.
- 2025 [48] ATLAS Collaboration. “Electron and photon performance measurements with the ATLAS
2026 detector using the 2015–2017 LHC proton-proton collision data”. In: *Journal of Instrumen-*
2027 *tation* 14.12 (2019), P12006.
- 2028 [49] Chiara Deponte. “Studies on the properties of non-prompt photons at the ATLAS experi-
2029 ment”. Presented 16 Aug 2022. Technische Universitaet Dortmund (DE), 2022.
- [50] ATLAS Collaboration. “Muon reconstruction performance of the ATLAS detector in pro-
ton–proton collision data at $\sqrt{s} = 13 \text{ TeV}$ ”. In: *The European Physical Journal C* 76.5 (2016).
- 2030
- 2031 [51] Sebastien Rettie. *Muon identification and performance in the ATLAS experiment*. Tech. rep.
2032 Geneva: CERN, 2018.
- 2033 [52] B. R. Webber. *Fragmentation and Hadronization*. 1999. arXiv: hep-ph/9912292 [hep-ph].
- 2034 [53] Eric M. Metodiev. *The Fractal Lives of Jets* | Eric M. Metodiev — ericmetodiev.com. https://
2035 /www.ericmetodiev.com/post/jetformation/. 2019, note = [Accessed 18-
2036 05-2024],
- 2037 [54] Steven Schramm. *ATLAS Jet Reconstruction, Calibration, and Tagging of Lorentz-boosted
2038 Objects*. Tech. rep. Geneva: CERN, 2017.
- 2039 [55] ATLAS Collaboration. “Topological cell clustering in the ATLAS calorimeters and its per-
2040 formance in LHC Run 1”. In: *The European Physical Journal C* 77.7 (July 2017).
- 2041 [56] ATLAS Collaboration. “Jet reconstruction and performance using particle flow with the
2042 ATLAS Detector”. In: *The European Physical Journal C* 77.7 (July 2017).

- 2043 [57] Matteo Cacciari, Gavin P Salam, and Gregory Soyez. “The anti-ktjet clustering algorithm”.
2044 In: *Journal of High Energy Physics* 2008.04 (Apr. 2008), 063–063.
- 2045 [58] Matteo Cacciari, Gavin P. Salam, and Gregory Soyez. “FastJet user manual: (for version
2046 3.0.2)”. In: *The European Physical Journal C* 72.3 (Mar. 2012).
- 2047 [59] Stephen D. Ellis and Davison E. Soper. “Successive combination jet algorithm for hadron
2048 collisions”. In: *Physical Review D* 48.7 (Oct. 1993), 3160–3166.
- 2049 [60] M. Wobisch and T. Wengler. *Hadronization Corrections to Jet Cross Sections in Deep-*
2050 *Inelastic Scattering*. 1999. arXiv: hep-ph/9907280 [hep-ph].
- 2051 [61] Gavin P Salam and Gr  gory Soyez. “A practical seedless infrared-safe cone jet algorithm”.
2052 In: *Journal of High Energy Physics* 2007.05 (May 2007), 086–086.
- 2053 [62] Gavin P. Salam. “Towards jetography”. In: *The European Physical Journal C* 67.3–4 (May
2054 2010), 637–686.
- 2055 [63] *A Monte Carlo study of track association to jets for b-tagging*. Tech. rep. Geneva: CERN,
2056 2021.
- 2057 [64] *Flavor Tagging with Track Jets in Boosted Topologies with the ATLAS Detector*. Tech. rep.
2058 All figures including auxiliary figures are available at <https://atlas.web.cern.ch/Atlas/GROUPS/PHYSICS/P>
2059 PHYS-PUB-2014-013. Geneva: CERN, 2014.
- 2060 [65] ATLAS Collaboration. “Performance of missing transverse momentum reconstruction with
2061 the ATLAS detector using proton-proton collisions at $\sqrt{s} = 13$ TeV”. In: *Eur. Phys. J. C*
2062 78.11 (2018), p. 903. arXiv: 1802.08168.
- 2063 [66] GEANT4 Collaboration, S. Agostinelli, et al. “GEANT4 – a simulation toolkit”. In: *Nucl.*
2064 *Instrum. Meth. A* 506 (2003), p. 250.
- 2065 [67] Christian Bierlich et al. *A comprehensive guide to the physics and usage of PYTHIA 8.3*.
2066 2022. arXiv: 2203.11601 [hep-ph].
- 2067 [68] J. Alwall et al. “The automated computation of tree-level and next-to-leading order differen-
2068 tial cross sections, and their matching to parton shower simulations”. In: *JHEP* 07 (2014),
2069 p. 079. arXiv: 1405.0301 [hep-ph].
- 2070 [69] Jon Butterworth et al. “PDF4LHC recommendations for LHC Run II”. In: *J. Phys. G* 43
2071 (2016), p. 023001. arXiv: 1510.03865 [hep-ph].
- 2072 [70] Peter Skands, Stefano Carrazza, and Juan Rojo. “Tuning PYTHIA 8.1: the Monash 2013
2073 Tune”. In: *Eur. Phys. J. C* 74.8 (2014), p. 3024. arXiv: 1404.5630 [hep-ph].

- 2074 [71] Patrick T. Komiske, Eric M. Metodiev, and Jesse Thaler. “Energy flow networks: deep sets
2075 for particle jets”. In: *Journal of High Energy Physics* 2019.1 (2019).
- 2076 [72] A. Kahn et al. “Anomalous jet identification via sequence modeling”. In: *Journal of Instrumentation* 16.08 (Aug. 2021), P08012.
- 2077
- 2078 [73] Georges Aad et al. “Anomaly detection search for new resonances decaying into a Higgs
2079 boson and a generic new particle X in hadronic final states using $\sqrt{s} = 13$ TeV pp collisions
2080 with the ATLAS detector”. In: *Phys. Rev. D* 108 (2023), p. 052009. arXiv: 2306.03637
2081 [hep-ex].
- 2082 [74] Georgios Choudalakis. *On hypothesis testing, trials factor, hypertests and the BumpHunter*.
2083 2011. arXiv: 1101.0390.
- 2084 [75] Peter Loch. “Jet measurements in ATLAS”. In: *J. Phys. Conf. Ser.* 323 (2011). Ed. by Gior-
2085 gio Bellettini, p. 012002.
- 2086 [76] The ATLAS Collaboration. “Search for diboson resonances in hadronic final states in 139
2087 fb-1 of pp collisions at $\sqrt{s} = 13$ TeV with the ATLAS detector”. In: *Journal of High Energy*
2088 *Physics* 2019.9 (Sept. 2019).
- 2089 [77] *Recommendations for the Modeling of Smooth Backgrounds*. Tech. rep. Geneva: CERN,
2090 2020.
- 2091 [78] The CMS Collaboration. “Search for resonant production of strongly coupled dark matter
2092 in proton-proton collisions at 13 TeV”. In: *Journal of High Energy Physics* 2022.6 (June
2093 2022).
- 2094 [79] Glen Cowan et al. “Asymptotic formulae for likelihood-based tests of new physics”. In: *The*
2095 *European Physical Journal C* 71.2 (Feb. 2011).
- 2096 [80] Ryan Edgar et al. *Functional Decomposition: A new method for search and limit setting*.
2097 2018. arXiv: 1805.04536 [physics.data-an].

Appendix A: Trigger Studies

2100 Both the lowest unprescaled E_T^{miss} and single small-R jet triggers were considered for this
 2101 analysis. The E_T^{miss} trigger is observed to have higher efficiency for low mass, high R_{inv} points,
 2102 while the single small-R trigger favors high mass, low R_{inv} points. Figure A.1 shows the yields
 2103 and signal efficiencies across the grid for both these strategies.

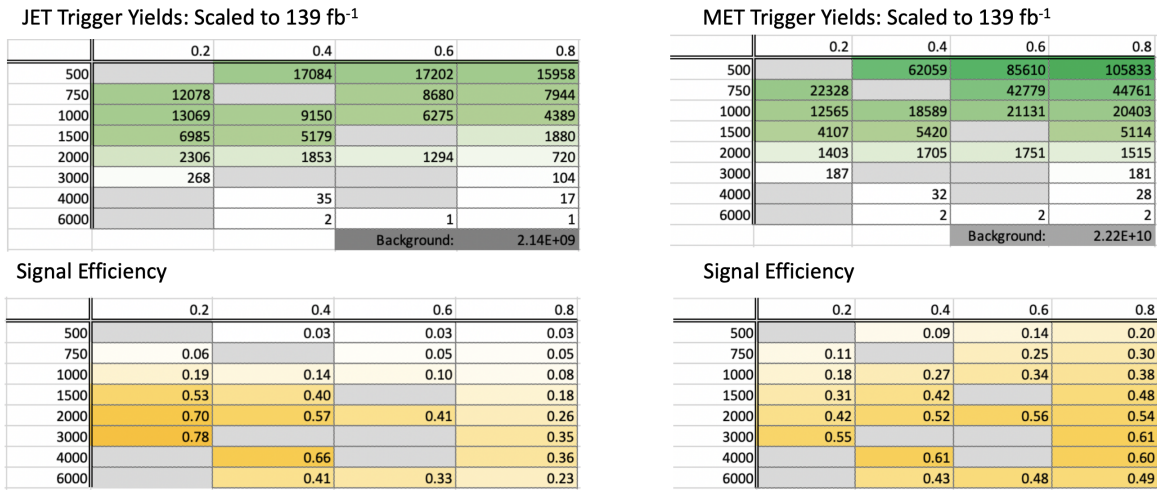


Figure A.1: Trigger yield and efficiency for both the MET trigger and small-R jet trigger approach. Each entry represent a signal point, labelled by the Z' mass and the R_{inv} fraction.

2104 The cross section is higher for the lower Z' mass signal points. As a result, our sensitivity
 2105 to these points and ability to set limits on them is already naturally enhanced. Figure A.2 shows
 2106 the factor of improvement in the inclusive S/\sqrt{B} using each trigger strategy. A cross-check was
 2107 also done calculating S/\sqrt{B} in windows around the mT mass. The results of this cross-check
 2108 confirmed the results shown in Figure A.2.

2109 Figure A.3 shows the ratio of S/\sqrt{B} across the signal grid for the jet trigger compared to the
 2110 E_T^{miss} trigger.

2111 This plot makes clear that the E_T^{miss} trigger favors the low mass, high R_{inv} signal points, while

$(\text{JET Trigger } S/\sqrt{B}) / (\text{Untriggered } S/\sqrt{B})$				
	0.2	0.4	0.6	0.8
500		1.26	1.43	1.53
750	2.99		2.52	2.68
1000	9.24	6.74	5.03	4.07
1500	26.45	20.15		8.83
2000	34.66	28.24	20.57	12.85
3000	39.05			17.35
4000		32.94		17.96
6000		20.57	16.55	11.53

$(\text{MET Trigger } S/\sqrt{B}) / (\text{Untriggered } S/\sqrt{B})$				
	0.2	0.4	0.6	0.8
500		1.43	2.21	3.15
750	1.72		3.86	4.69
1000	2.76	4.26	5.26	5.89
1500	4.83	6.56		7.47
2000	6.55	8.08	8.65	8.40
3000	8.46			9.38
4000		9.51		9.32
6000		6.68	7.43	7.59

Figure A.2: The factor of improvement in S/\sqrt{B} for each trigger method compared to the untriggered case.

	0.2	0.4	0.6	0.8
500		0.89	0.65	0.49
750	1.74		0.65	0.57
1000	3.35	1.58	0.96	0.69
1500	5.47	3.07		1.18
2000	5.29	3.49	2.38	1.53
3000	4.62			1.85
4000		3.46		1.93
6000		3.08	2.23	1.52

Figure A.3: The ratio of S/\sqrt{B} of jet trigger over E_T^{miss} trigger selection.

2112 the single jet trigger favors the high mass, low R_{inv} signal points. A number of considerations led
2113 us to selecting the single jet trigger. First, Figure A.2 illustrates that the sensitivity enhancement is
2114 greater for signals favored by the jet trigger than signals favored by the E_T^{miss} trigger. This indicates
2115 we have more to gain from focusing on the region of our signal grid where the jet trigger is most
2116 efficient. We combined this with the observation that the jet trigger is beneficial for high mass
2117 points where the cross-section is lower and we need to maximize sensitivity to hope to set limits
2118 on these points.

2119 Second, there are a number of analysis variables at our disposal which are more discriminant for
2120 high R_{inv} signals than for low R_{inv} signals. A collection of these variables are shown in Figure A.4.
2121 Given that we had multiple avenues available to enhance sensitivity to low R_{inv} signals through
2122 analysis strategy cuts, we opted for a trigger strategy that benefitted the low R_{inv} signal points.
2123 Additionally, we know E_T^{miss} is highly correlated with these discriminant analysis variables, and a
2124 E_T^{miss} trigger would reduce the effectiveness of these variables. Not implementing the E_T^{miss} trigger
2125 allows us to explore other ways of leveraging E_T^{miss} in the analysis using a cut that is more finely
2126 tuned to the specifics of the signal model than the E_T^{miss} trigger is.

2127 Third, we know that fitting the high R_{inv} mass points would be challenging given their very
2128 broad shapes in the key analysis variable m_T . Given the analysis decision to do a search for
2129 resonant features in m_T , we chose to design a search that emphasized maximizing sensitivity
2130 to the signal points that we were mostly to appear as a resonant feature in m_T . The shape of
2131 m_T and our reduced ability to set limits on high R_{inv} points is demonstrated in the body of this
2132 note. Another search strategy may be more optimal for setting limits on high R_{inv} semi-visible jet
2133 signals, but it is currently outside the scope of this analysis.

2134 A jet or E_T^{miss} trigger was also considered, but abandoned due to concerns about sculpting
2135 features in the smoothly falling E_T^{miss} or leading jet p_T distributions, as shown in Figure A.5.

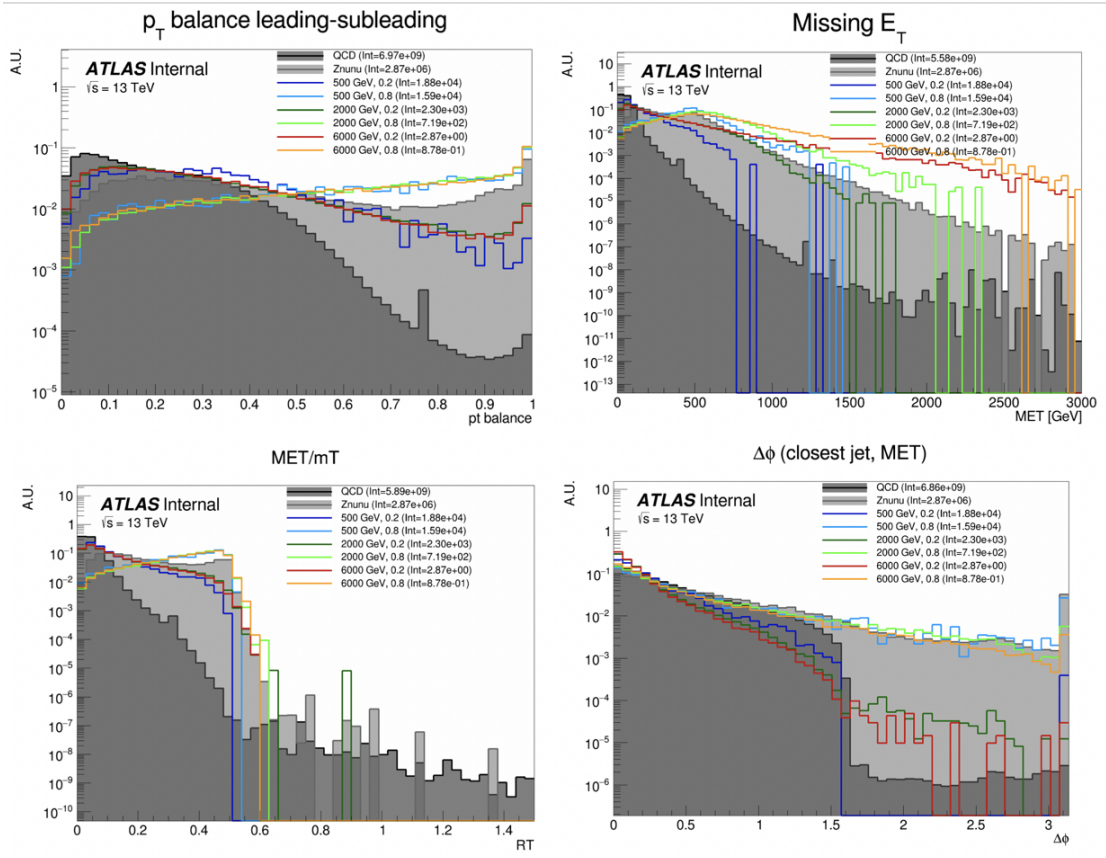


Figure A.4: Analysis variables where high R_{inv} signals a clearly distinct from background and low R_{inv} variables. On the contrary, leading jet p_T is one of the only variables where low R_{inv} signals are distinct from background.

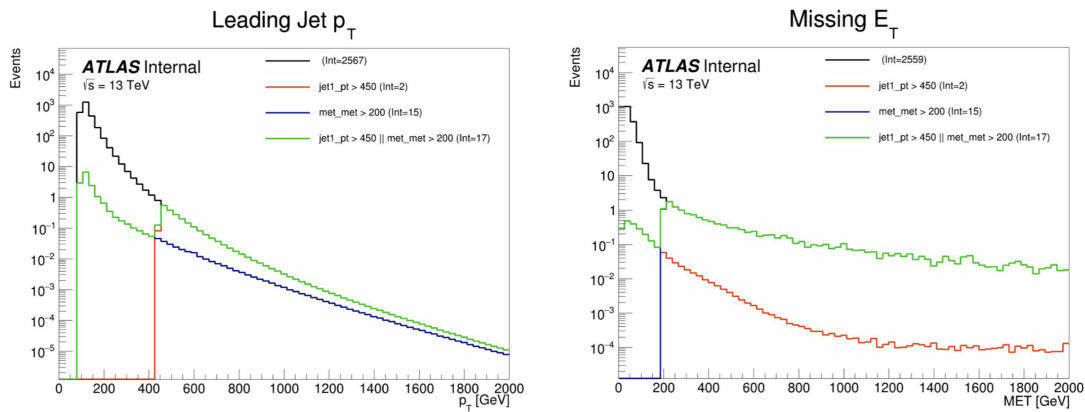


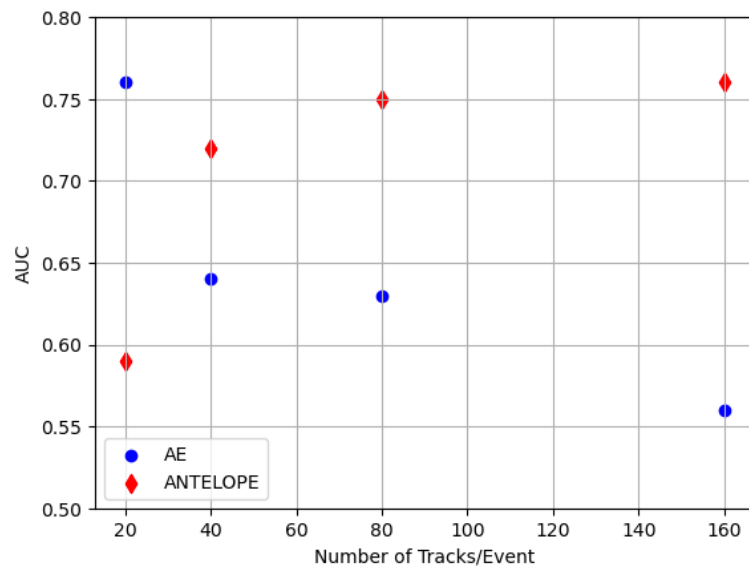
Figure A.5: OR of jet and E_T^{miss} triggers.

Appendix B: Machine Learning Approaches

2138 B.1 Unsupervised: AE vs. ANTELOPE

2139 To understand the benefits of the semi-supervised ANTELOPE approach, we study the AN-
 2140 TELope in comparison to a traditional anomaly detection architecture like an autoencoder. The
 2141 autoencoder cannot accommodate variable length or permutation invariant inputs.

2142 Figure B.1 shows the AUC determined by each of these two tools as a function of number
 2143 of tracks. The trend is that the AE suffers when more information is given, due to the presence
 2144 of 0-padding. In contrast, the ANTELOPE architecture performs better with more information,
 motivating the use of high dimensional input modelin with this method.

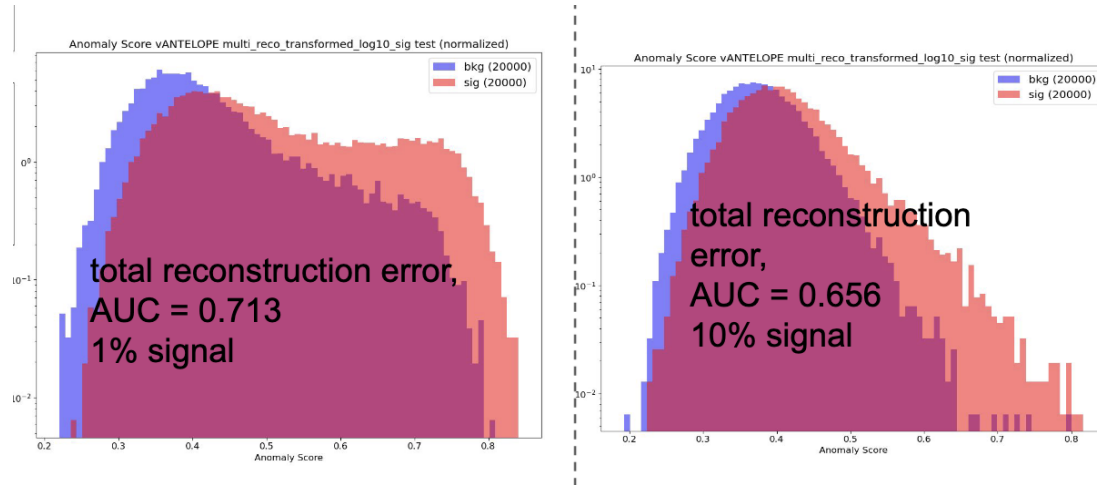


- Confirms that AE is negatively sensitive to zero padding while ANTELOPE sees a performance improvement as it sees more “information”

2145 Figure B.1

2146 **Signal Contamination**

2147 To understand the effect of signal contamination in training on the ANTELOPE score, we inject
2148 a percent of signal events into the data used to train the ANTELOPE autoencoder stage and look
2149 at the AUC on signals. Figure B.2 shows no variation in AUC with 1% contamination in training
data, but a few % drop going up to 10%.



2150 Figure B.2

2151 **B.2 PFN Optimality Checks**

2152 The PFN is trained using QCD as the background. A study was done to compare the perfor-
2153 mance of the tool in the analysis context if it trains against QCD or a representative MC background
2154 considering the small fractions of other processes ($V+jets$, top) that would contribute at preselec-
2155 tion. Figure B.3 shows the AUC across the grid for both training approaches, revealing better
2156 performance if the tool focuses on learning QCD differences.

2157 Further studies were done to ensure the relatively optimality of the single PFN model, trained
2158 over combined signals, across the grid. As the grid spans signals with a large range of E_T^{miss} , their
2159 varying input features and background composition may be conducive to separate PFN models
2160 trained on high and low E_T^{miss} signal points to better capture the signal-background differences.
2161 Figure B.4 shows a comparison of the signal-inclusive PFN model performance and the perfor-

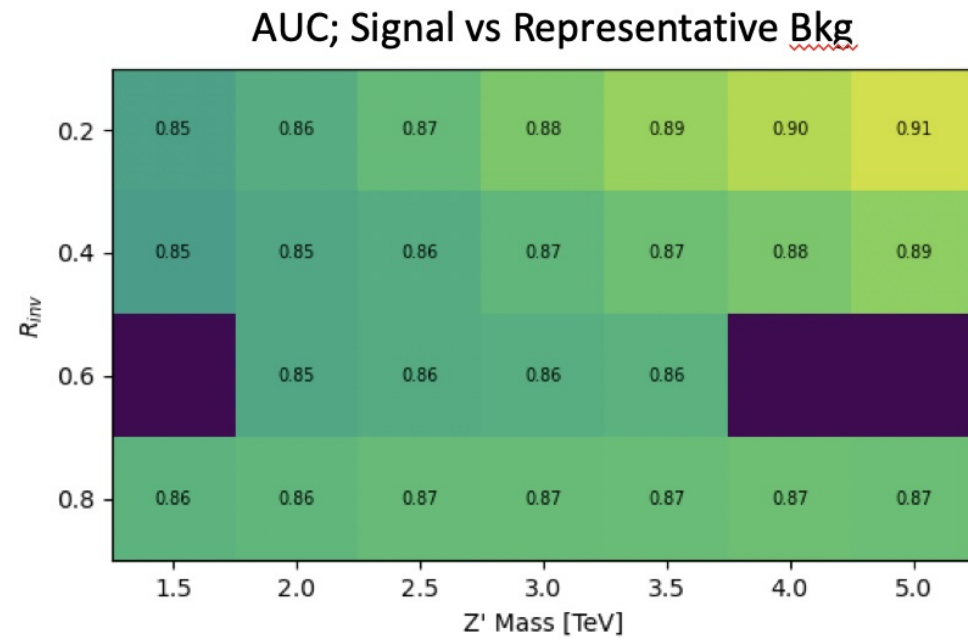
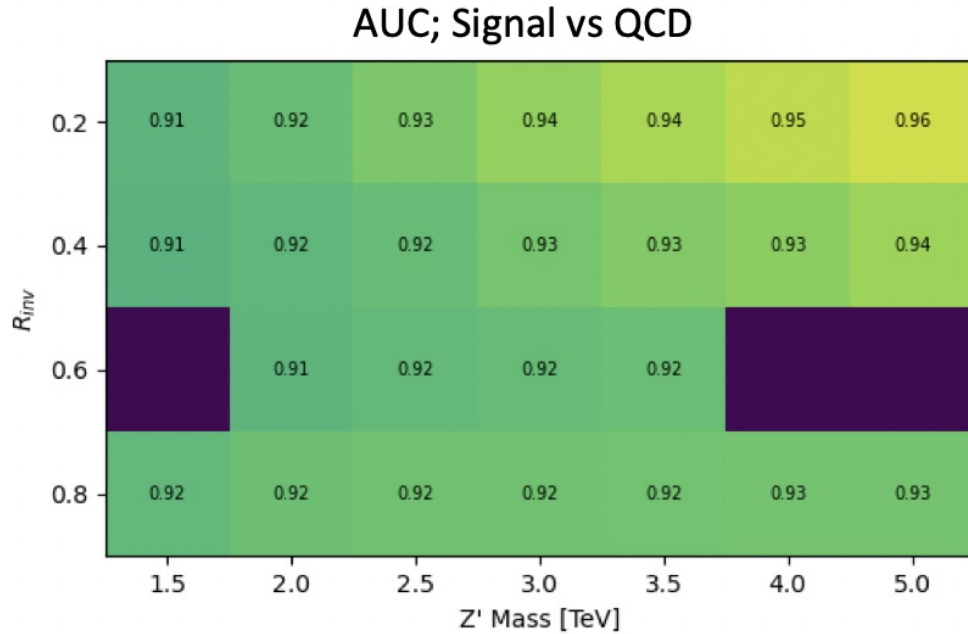


Figure B.3: AUC from the PFN score for each signal in the SVJ grid, shown versus the QCD-only training sample (top) and the total MC background (bottom). Note the three missing points will be added shortly - they were delayed due to a DAOD production mistake.

2162 mance of models separated into high and low R_{inv} signals in training. The most notable impact is
 2163 found for the low R_{inv} and high mass points, indicating that the signal-inclusive PFN is learning
 2164 morning about the distinction between high- E_T^{miss} signals and backgrounds. However, these high
 2165 mass points are also the most challenging to find due to their very wide resonance on top of m_T ,
 2166 and in the final projected sensitivity in the m_T window the differences are $< 10\%$ across the grid.
 2167 To maintain a harmonized strategy with the ANTELOPE region we keep the inclusive PFN model
 2168 as the final version.

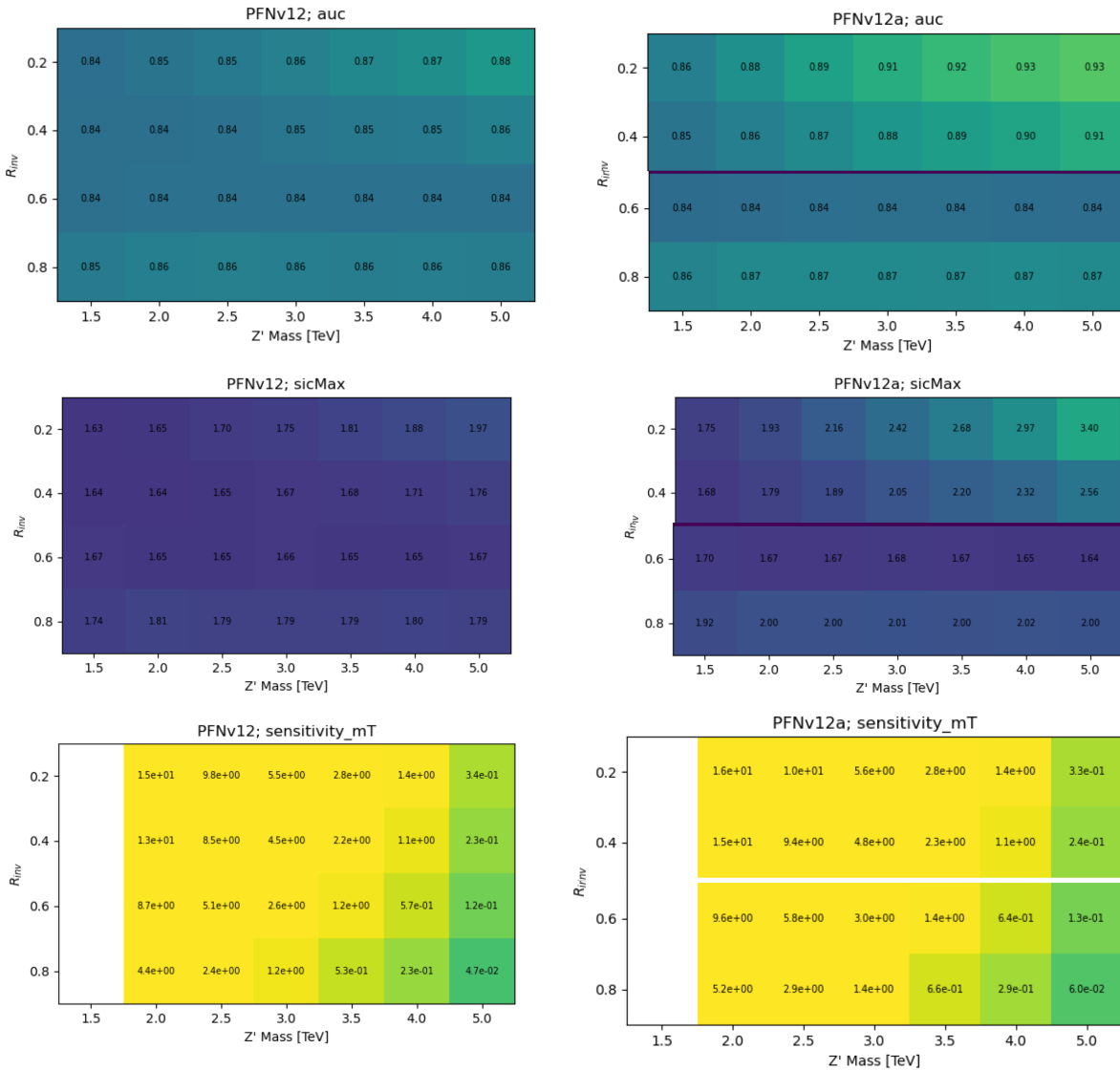


Figure B.4: Comparison of PFN AUC (top), SIC (middle), and sensitivity in the m_T mass window (bottom) for a single PFN model (left) vs. two models, trained on $R_{inv} < 0.5$ and > 0.5 separately.

2169 Figure B.5 shows the optimal cut on the PFN score for each point in the signal grid, motivating
the loose inclusive choice used to define the SR.

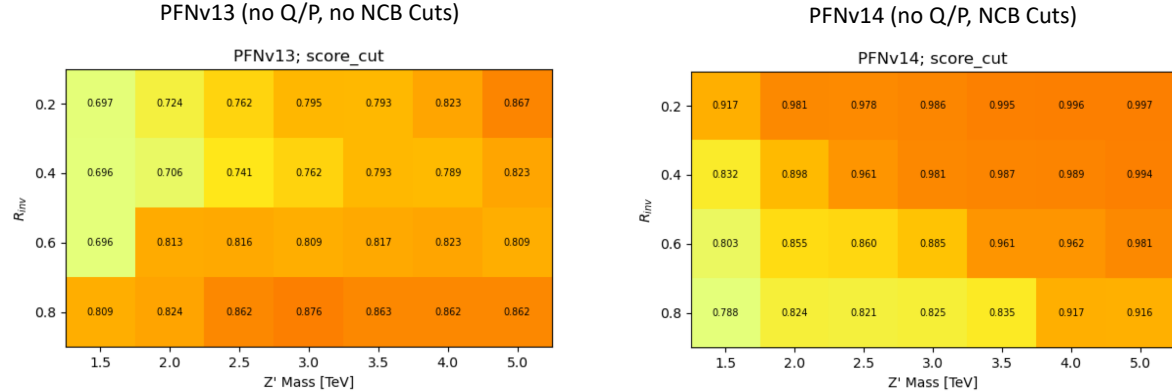


Figure B.5: Preferred cuts on the PFN score for each point in the grid, comparing the effect of adding the NCB preselection.

2170
2171 Grid cans for optimality were also performed on the number of training epochs, number of
2172 training events, batch size, learning rate, number of neurons, and dimension of the Φ space. The
2173 results of these scans are summarized in the tables in Figure B.6. The selected or default parameters
2174 were found to be optimal, or close enough to optimal to justify not increasing the training time or
2175 complexity of the network for negligible increases in performance.

2176 B.3 Supervised: BDT vs. PFN

2177 Studies of the BDT compared to the PFN performance, where training over events modeled
2178 with jet-related HLVs (high-level track variables, etas, angles, etc.) are compared to events mod-
2179 eled by the tracks of the 2 leading jets. Figure B.7 shows the performance of the BDT with and
2180 without explicit use of energy scale variables.

2181 B.4 Single Jet vs Jet System ML Approach

2182 The analysis considered both a single jet and jet system ML approach. A jet system approach,
2183 where the leading two jets and their orientation with respect to each other was selected for a variety
2184 of reasons. The jet system approach captures the MET information which is crucial to identifying

	default s_events=500096 b_events=501396	s_events:49135 b_events: 48220 *	s_events:246205 b_events:245136
AUC	.905	.874	.892

	default n_neuro n 40	n_neuro n 150	phi_dim 32	phi_dim 128	learning rate 0.0005	learning rate 0.002	nepochs 50	nepochs 200*	
AUC	.905	.898	.906	.902	.906	.898	.905	.893	.909

	default	batchsize_pfn 250	batchsize_pfn 1000
AUC	.905	.903	.902

Figure B.6: Scans done to check for optimality of PFN training parameters.

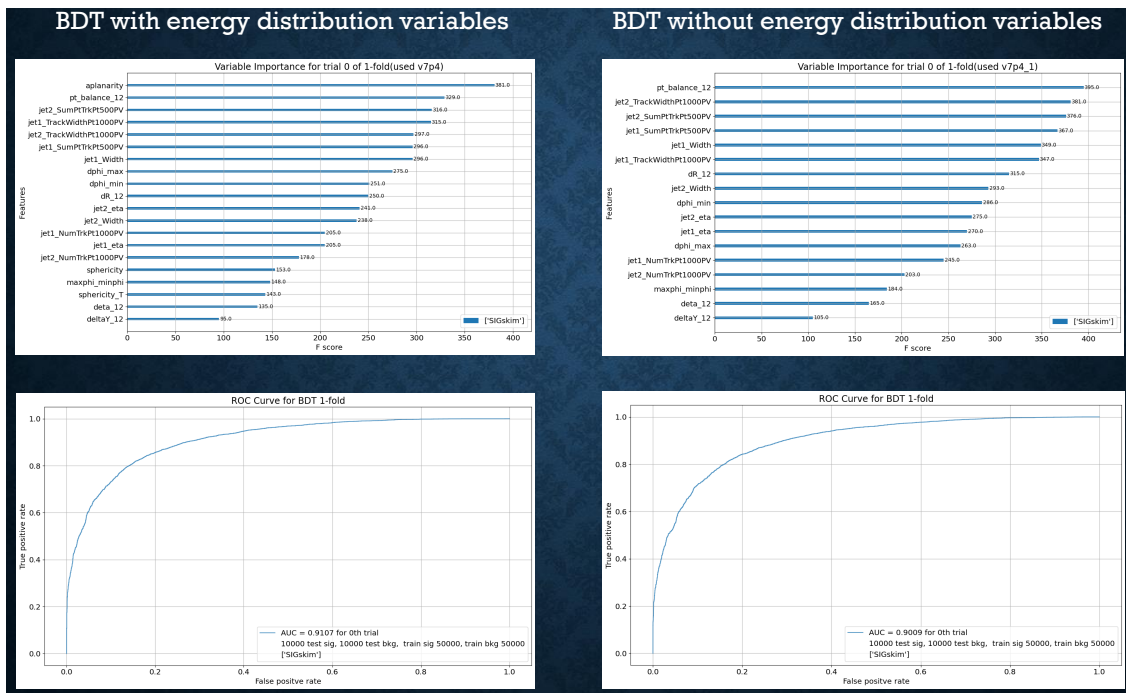


Figure B.7

2185 SVJs. In the topology where the dark quarks come from a heavy Z' decay and are back to back,
 2186 the measurable MET will have to be aligned with one or the other.

2187 Additionally, the performance of both a supervised PFN approach and an unsupervised AE ap-
 2188 proach was studied in the case of a single jet tagger. While the PFN approach was still performant
 2189 on a single jet case, the unsupervised approach was significantly improved by using both jets. This
 2190 is shown in Figure B.8.

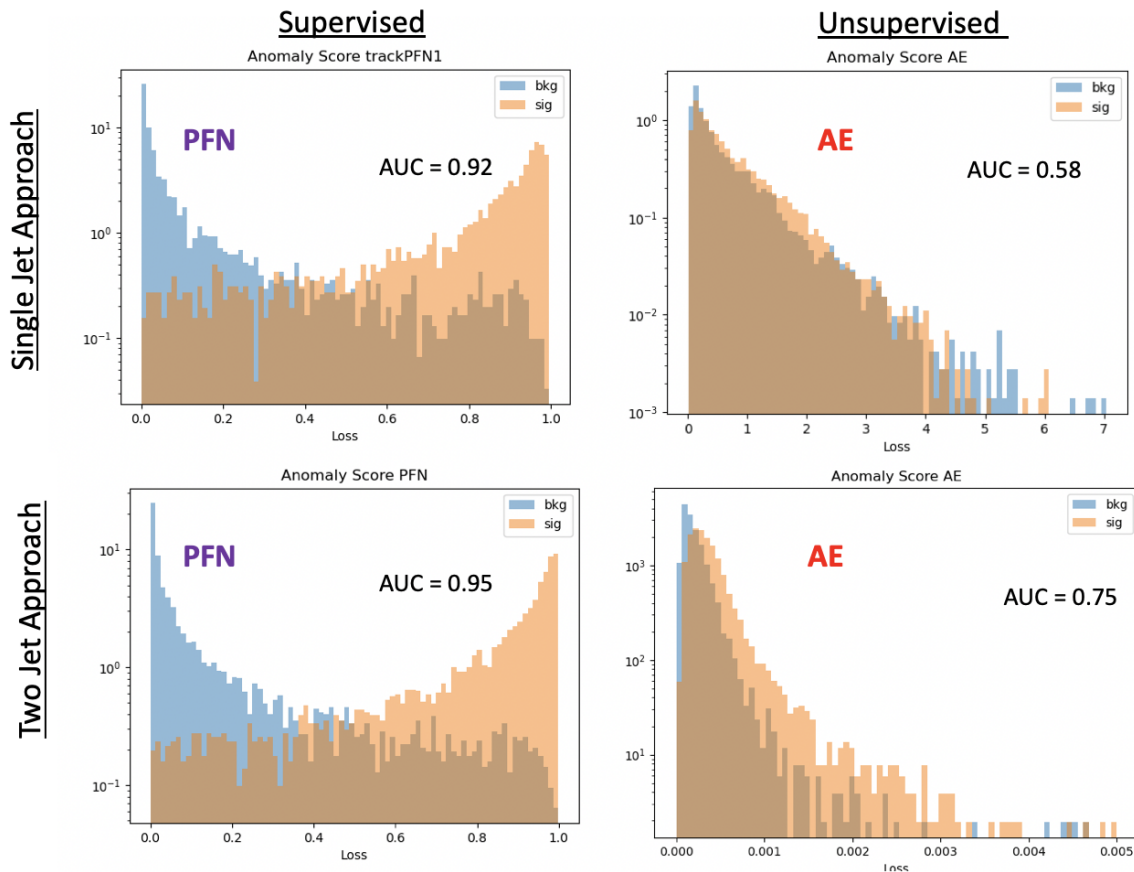


Figure B.8: ϕ Performance comparison between single jet and jet system ML approach

2191 B.5 PFN Training Composition

2192 The overall sensitivity and stability across the signal grid is observed to benefit by training
 2193 the ML tool to reject only the dominant background, QCD. This is evidenced by the PFN response
 2194 plots shown in Section 7.1.1 and the following AUC and sensitivity comparison plots in Figure B.9.

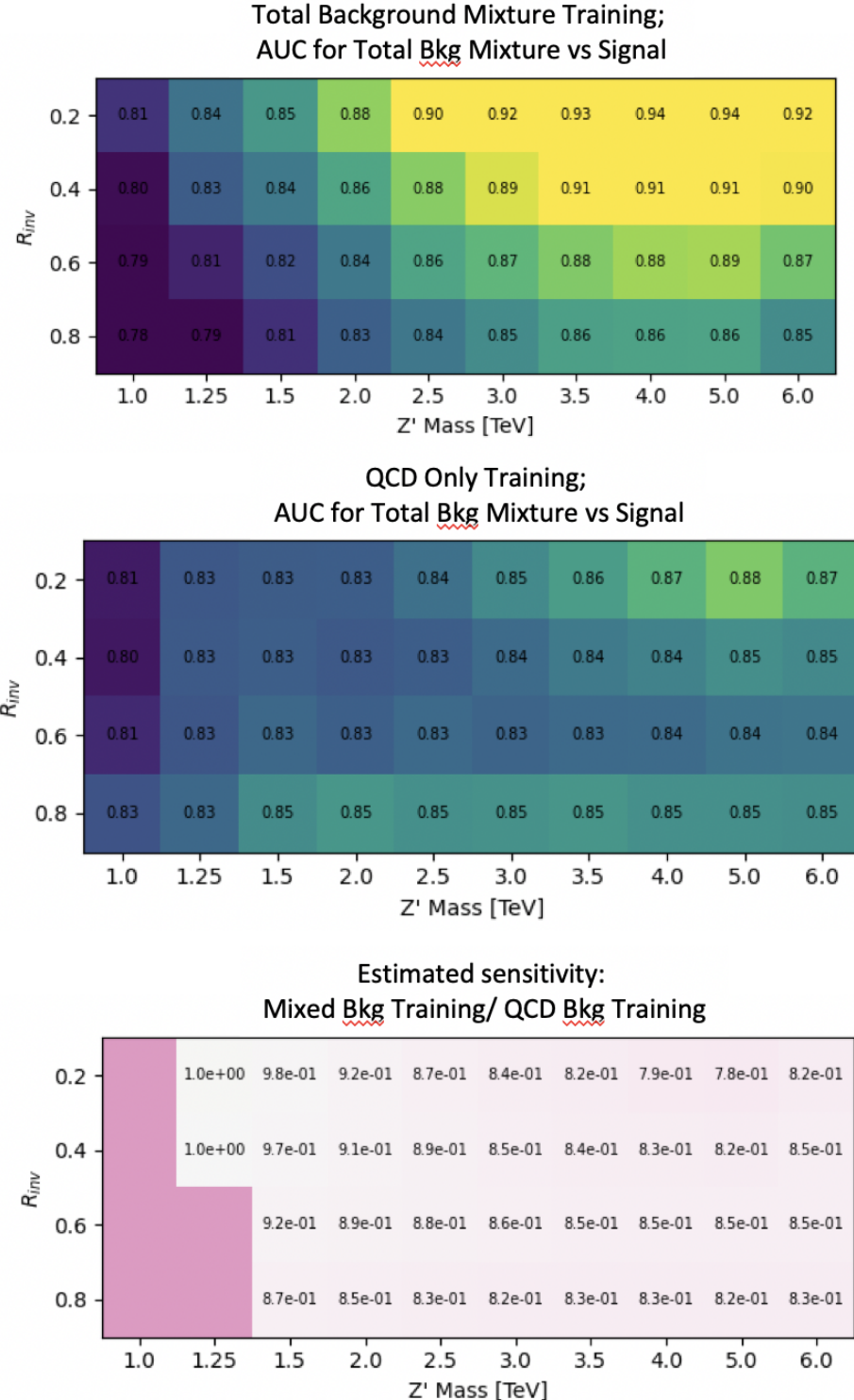


Figure B.9: ϕ Comparison in the AUC score across the grid for the mixed background strategy vs the QCD only strategy. The bottom table highlights that the QCD only strategy gives superior sensitivity across the signal grid.

2195 **B.6 E_T^{miss} and $E_T^{\text{miss}}\phi$ Shapes**

2196 The Tight cleaning working point was found to be necessary due to the nature of our signal
 2197 being E_T^{miss} and hadronic activity that are closely aligned, presenting a signature that is very af-
 2198 fected by beam-induced background (BIB). As per the cleaning recommendations, any event with
 2199 a jet that fails Tight criteria is rejected. Figure B.10 shows the effect of Tight cleaning on the shape
 of E_T^{miss} in data, fixing a feature present in Loose cleaning only.

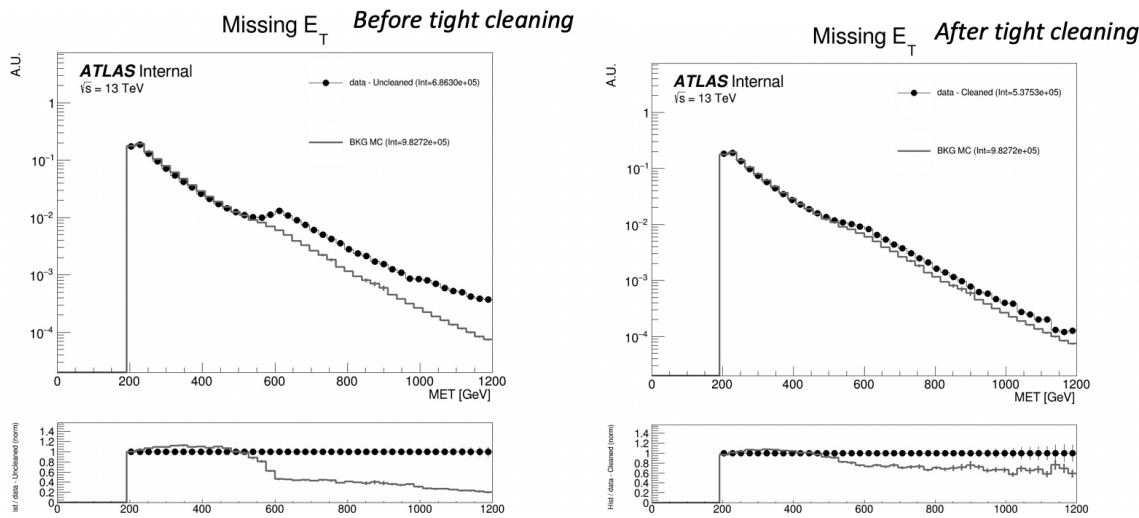


Figure B.10: E_T^{miss} in data before and after Tight event cleaning is applied.

2200
 2201 Figure B.11 further illustrates the correlation between the excess events and the leading jet p_T ,
 2202 and illustrates the impact of the tight cleaning in reducing this feature.

2203 Figure B.12 illustrates the 2D η vs ϕ distribution of the leading and subleading jets before and
 2204 after tight cleaning. No major spikes or hot areas are observed. One bright spot in the subleading
 2205 jet map at $\eta \approx 0$ and $\phi \approx -1.0$ was studies and found to have no impact on the E_T^{miss} shape, indicating
 2206 a likely missed spot in the Tile cleaning which does not affect E_T^{miss} .

2207 **B.6.1 NCB Preselection**

2208 A final preselection was derived to entirely remove the presence of non-collision background,
 2209 particularly noted through its impact on the E_T^{miss} shape. Cuts are added on the subleading jet

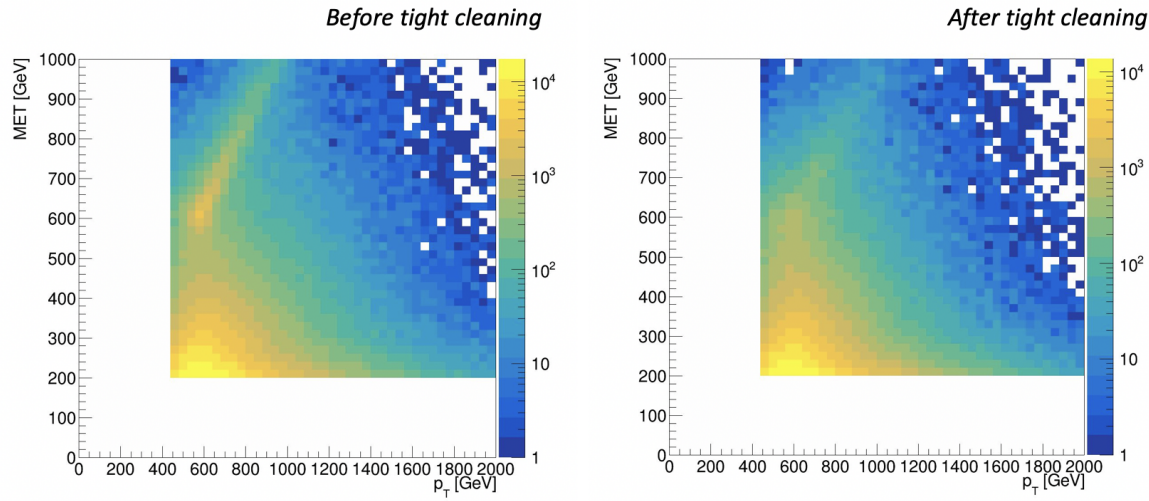


Figure B.11: E_T^{miss} vs jet1 p_T in data before and after Tight event cleaning is applied.

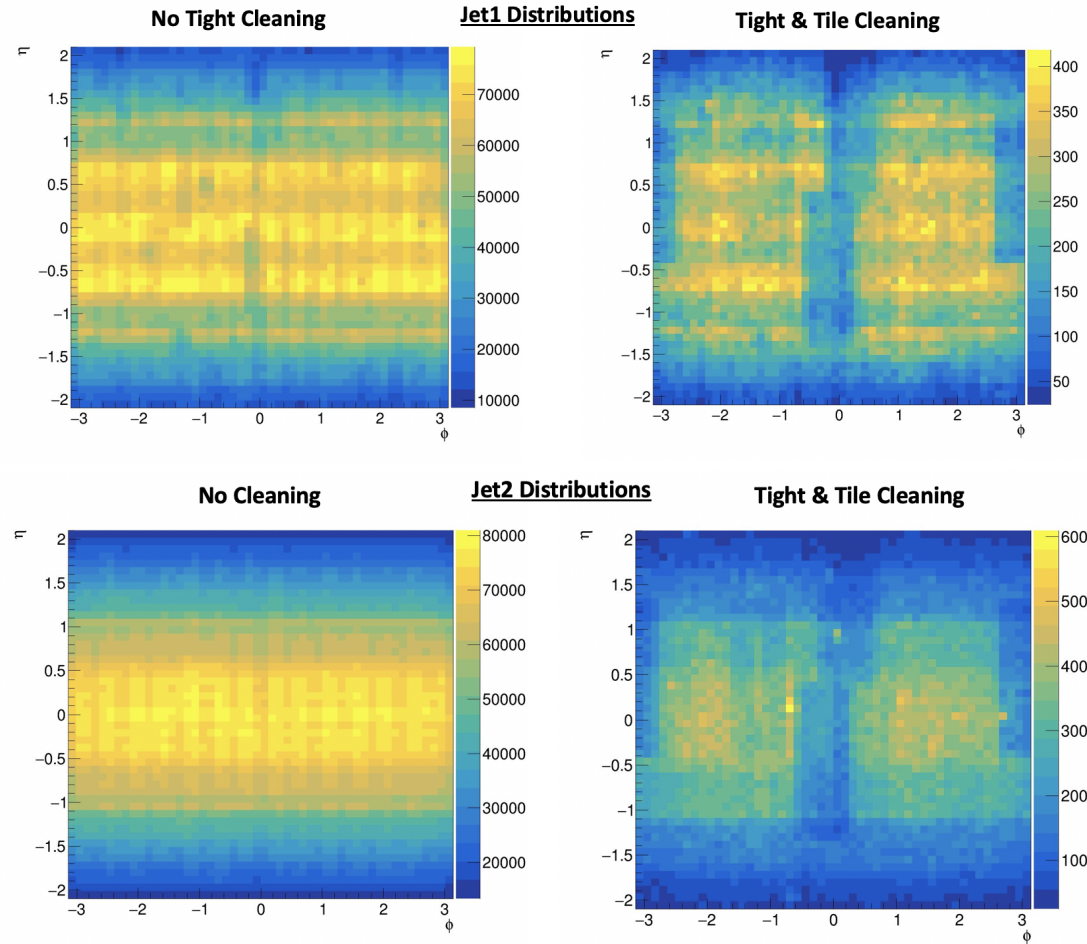


Figure B.12: η vs ϕ for leading and subleading jets, before and after the application of tight cleaning.

2210 $p_T > 150$ GeV and $\Delta\Phi(j1,j2) > 0.8$. Figure B.13 shows the impact of these cuts to create a fully
 2211 smoothly falling E_T^{miss} distribution. Figure B.14 shows the impact on the data yields in the CR and
 2212 VR and several signals in the SR; the greatest inefficiencies are found for the signal points that are
 2213 not sensitive in the analysis anyway. The reduction in background ultimately means that no impact
 is noticed on the limits.

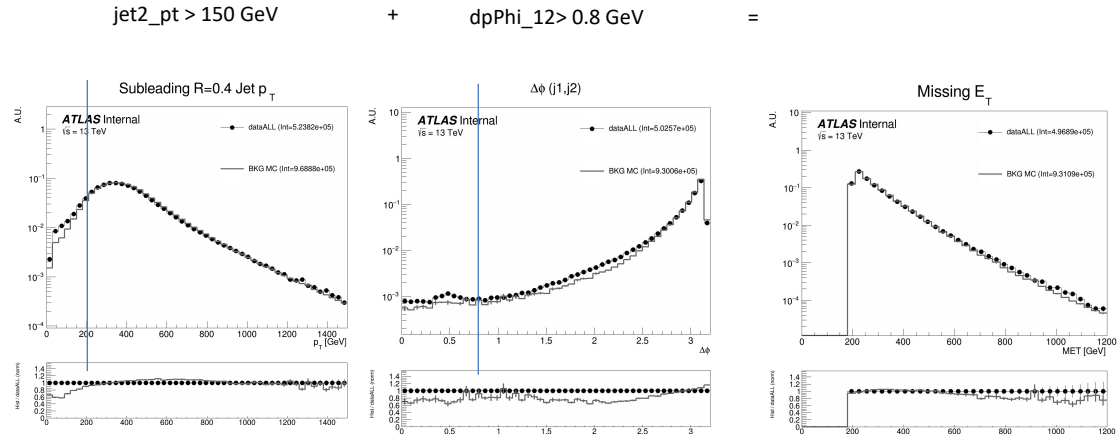


Figure B.13: Added NCB preselection and impact on E_T^{miss} shape.

2214
 2215 Figure B.15 shows the impact of these cuts on the 2D E_T^{miss} vs jet1 p_T distribution, where the
 2216 feature is also observed to be smoothed.
 2217 This strategy was discussed and signed off by the Jet/ E_T^{miss} CP group¹.

2218 B.6.2 TileCal Correction

2219 The $E_T^{\text{miss}}\phi$ distribution was fixed through the implementation of an offline TileCal correction
 2220 tool, which removes certain lumiblocks of certain runs based on poor functioning in TileCal mod-
 2221 ules. Figure B.16 shows the $E_T^{\text{miss}}\phi$ distribution in data across runs, before and after the application
 2222 of the tool, showing the ability of the tool to remove spikes due to instrumental problems.

¹<https://indico.cern.ch/event/1413217/>

Region	Before Extra Cleaning Cuts	After Extra Cleaning Cuts	Efficiency
Data - CR	108957	107435	0.99
Data - VR	116917	116008	0.99
2500, 0.2 - SR	1921	1709	0.89
2500, 0.4 - SR	1819	1424	0.78
2500, 0.6 - SR	1150	735	0.64
2500, 0.8 - SR	543	251	0.46
5000, 0.2 - SR	21.5	20.3	0.94
5000, 0.4 - SR	22.3	19.4	0.87
5000, 0.6 - SR	16.0	11.6	0.73
5000, 0.8 - SR	8.1	4.1	0.51

Figure B.14: NCB preselection impact on data and signal yields.

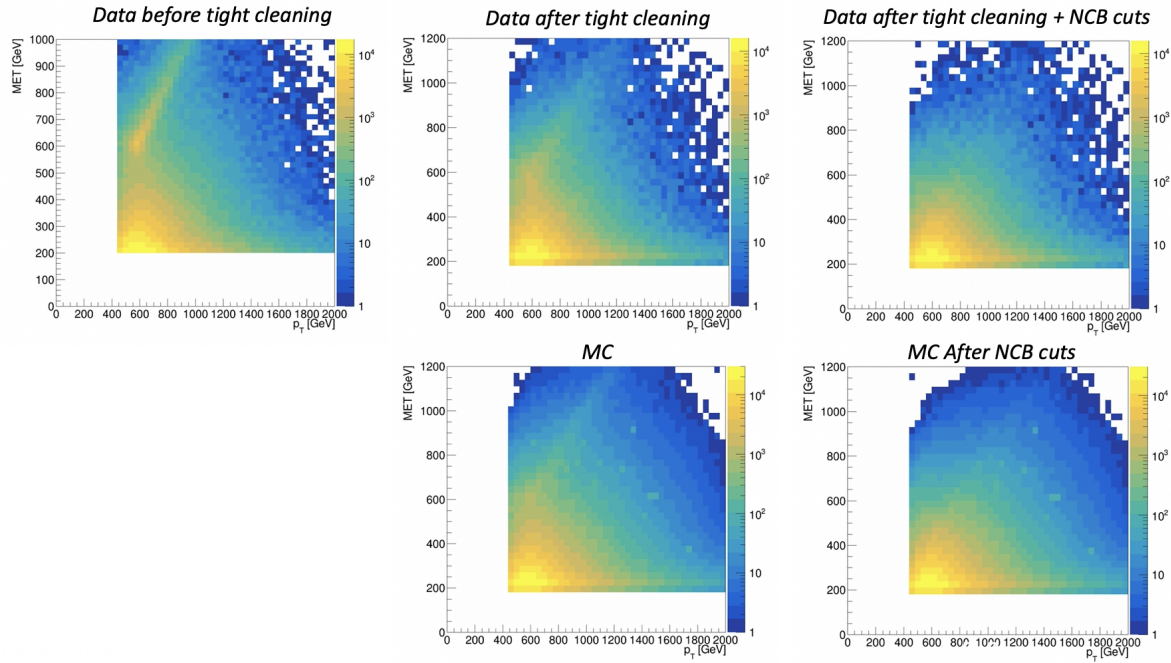


Figure B.15: Impact of tight cleaning and non-collision background preselection.

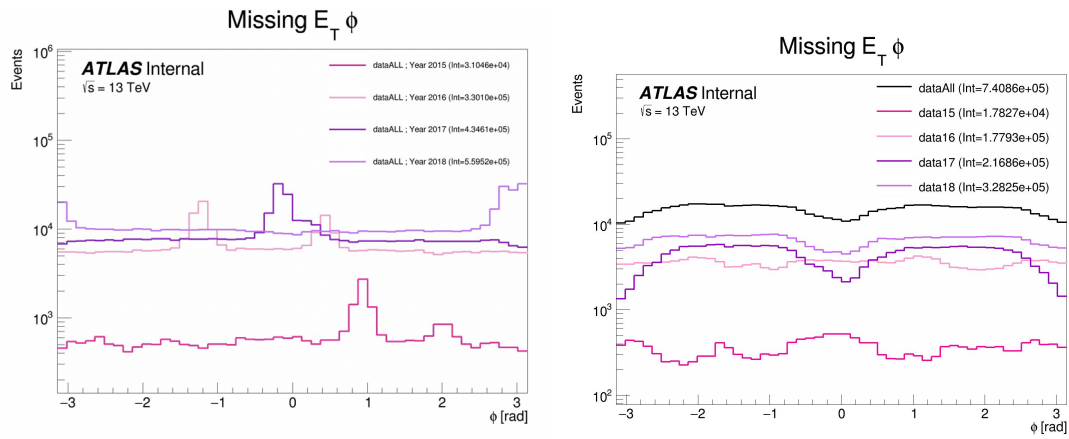


Figure B.16: $E_T^{\text{miss}}\phi$ in data, before (left) and after (right) application of the TileCal correction tool.

2223

2224

Appendix C: Truth Studies

2225 C.1 Jet dR Matching

2226 Figure C.1 demonstrates that the leading and subleading jet are overwhelmingly the most likely
2227 jets to be matched to a dark quark.

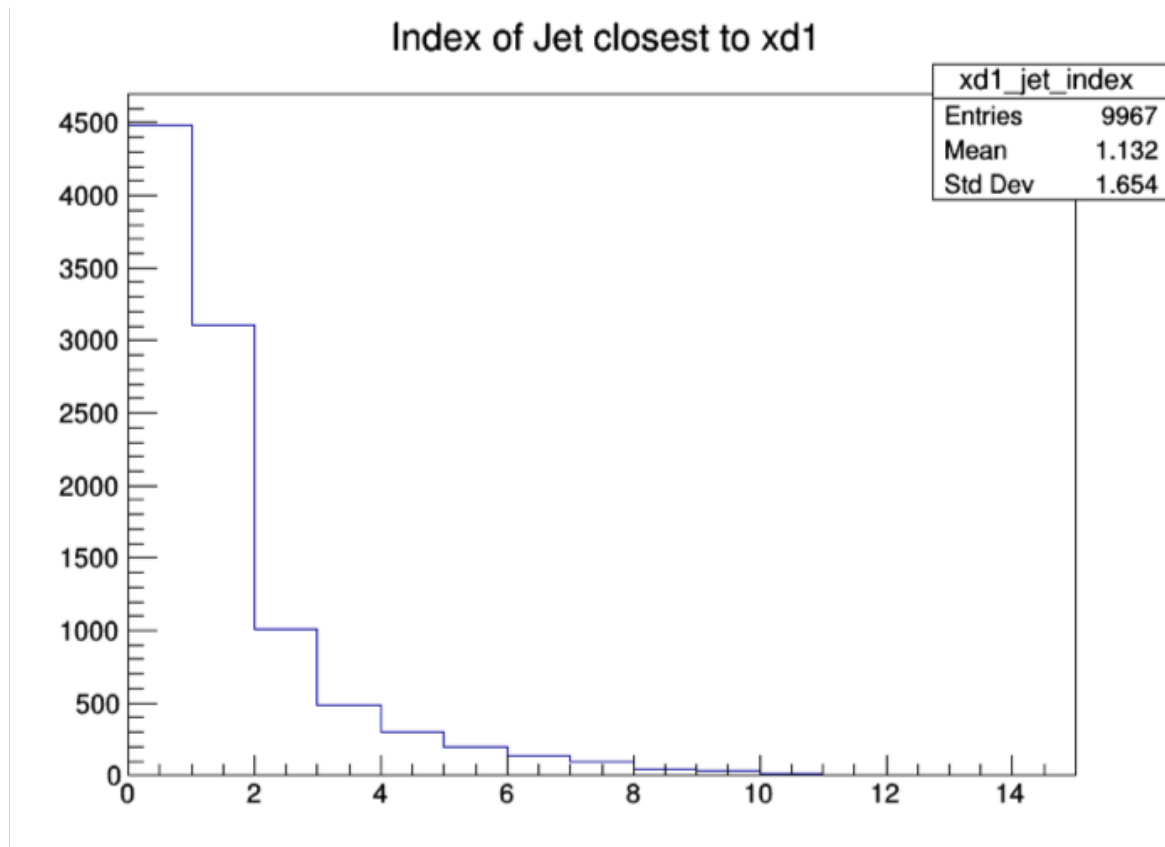


Figure C.1: Index of jets truth matched (by requirement of $\Delta R < 0.4$) with dark quark.

2228 Other matching strategies were explored, such as choosing the jet most aligned with $E_T^{\text{miss}}(\min$
2229 $\Delta\phi(j, E_T^{\text{miss}}))$ and the jet most anti-aligned with $E_T^{\text{miss}}(\max \Delta\phi(j, E_T^{\text{miss}}))$. However, in most cases
2230 these two measurements correspond to the subleading and leading jets respectively. Additionally,
2231 as shown in Figure C.2 the leading/subleading strategy generally results in more matched jets than

2232 the E_T^{miss} aligned and E_T^{miss} anti-aligned strategy. Therefore the leading and subleading jets were
 2233 chosen for consideration in this analysis.

Signal ($M_{Z'}$, r_{inv})	% Leading Jets dR Matched	% MET anti- aligned Jets dR matched	% Subleading Jets dR Matched	% MET aligned jets dR matched
750 GeV, 0.2	0.432883	0.3567	0.3777	0.3504
750 GeV, 0.8	0.187819	0.1589	0.1826	0.1803
3500 GeV, 0.2	0.692931	0.5408	0.5097	0.4144
3500 GeV, 0.8	0.344057	0.2927	0.2634	0.2585
6000 GeV, 0.2	0.647237	0.5047	0.4975	0.3919
6000 GeV, 0.8	0.345542	0.2882	0.2517	0.249

Figure C.2: Percent of jets with $\Delta R(j, E_T^{\text{miss}}) < 0.4$ comparing two jet identification strategies. Leading and subleading jets are seen to be the better metric for identifying jets associated with the dark quark decay.

2234

2235

Appendix D: BumpHunter

2236 D.1 Signal Mass Resolution m_T Binning

2237 In the discovery region, a binning for m_T is determined that is based on the expected signal
2238 width. This is done to improve the BumpHunter performance. The signal mass resolution for a
2239 given point is determined with a double-sided Crystal Ball fit to the mass. These fits are performed
2240 across Z' mass, and a linear fit to these values is performed to determine the optimal bin width
2241 across m_T .

2242 The x-axis value used is a data-driven way to determine the appropriate value of m_T for a given
2243 signal, given that the considerable E_T^{miss} from the dark particles means that the truth Z' mass does
2244 not well approximate the peak m_T value. The E_T^{miss} in the final state is generally an underestimate
2245 of the amount of energy that could be attributed to dark hadrons, as any dark hadrons that are
2246 back-to-back in the transverse plane will cancel out and not register as E_T^{miss} . Therefore m_T is
2247 always an underestimate of the Z' mass, so the truth Z' mass can be used as an upper bound. An
2248 integral is then performed backwards from that value until 60% of the total signal yield is included.
2249 This window is referred to as the 60% mass window; the mean of this window then provides an
2250 approximate localization of the signal mass peak in m_T . Figure D.1 shows some examples of this
2251 algorithm on several signal points of varying R_{inv} and mass.

2252 Figure D.2 shows the result of this linear fit for the four R_{inv} values considered in the signal
2253 grid. As expected, the resolution is considerably different for low and high R_{inv} points.

2254 A single m_T binning for the final SR plotting and BumpHunting is determined by selecting a
2255 harmonized binning at low m_T , and moving to wider bins at high m_T . As for higher R_{inv} signal
2256 points the mass resolution linear fit gives negative results, we require each bin to have a width of
2257 at least 100 GeV. Figure D.3 shows the resulting bins for each R_{inv} category that comes from the

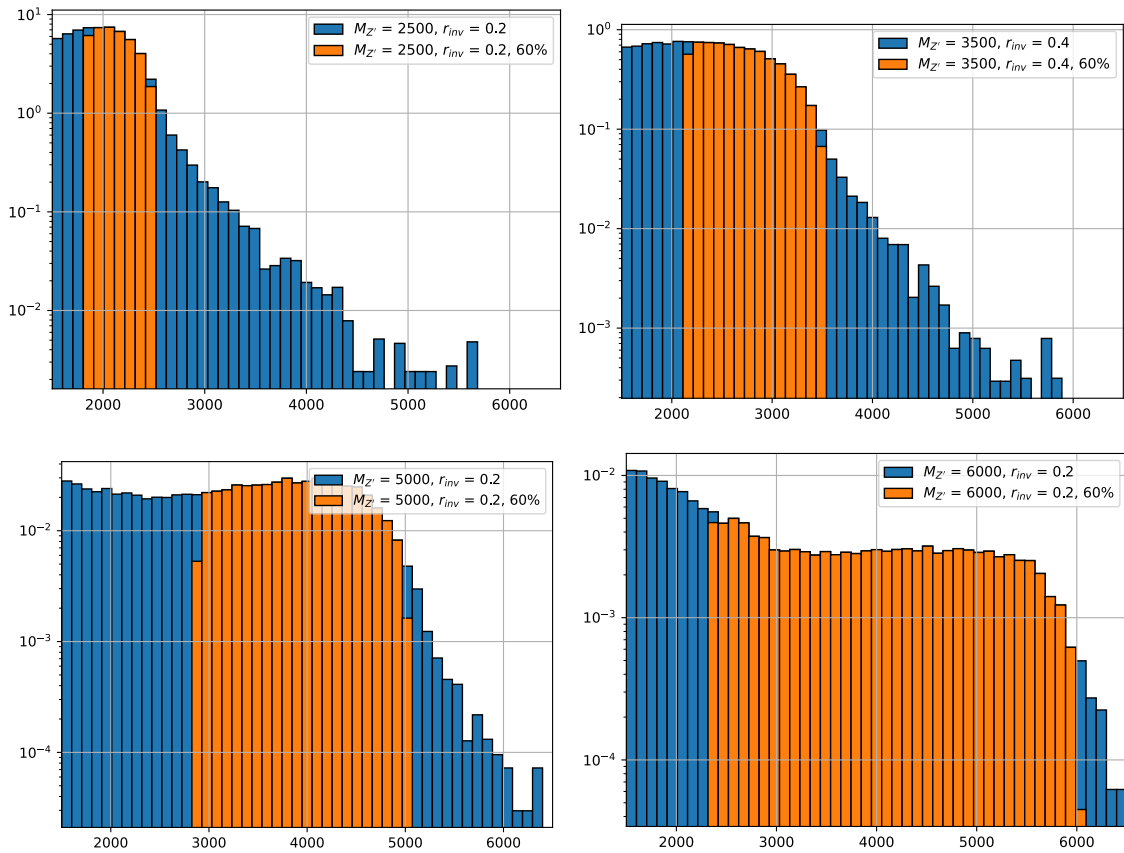


Figure D.1: Example determinations of the 60% mass window means for several signal points.

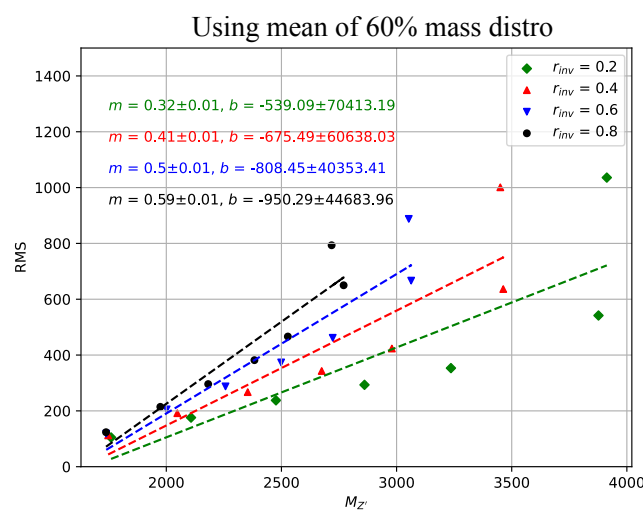


Figure D.2: Signal mass resolution for m_T binning for the signal grid in (R_{inv} , mass) space.

mass resolution fits, with the addition of the minimum 100 GeV bin width requirement.

$r_{inv} = 0.2 \rightarrow [1500, 1600, 1700, 1800, 1904, 2029, 2177, 2356, 2569, 2824, 3128, 3493, 3929, 4451, 5075, 5822, 6715]$

$r_{inv} = 0.4 \rightarrow [1500, 1600, 1700, 1800, 1910, 2053, 2238, 2477, 2787, 3187, 3704, 4374, 5240, 6361]$

$r_{inv} = 0.6 \rightarrow [1500, 1600, 1700, 1800, 1919, 2087, 2321, 2650, 3110, 3755, 4659, 5925, 7698]$

$r_{inv} = 0.8 \rightarrow [1500, 1600, 1700, 1800, 1927, 2117, 2400, 2823, 3455, 4400, 5811, 7918]$

Figure D.3: m_T bins based on the signal mass resolution and the minimum 100 GeV width requirement, for each R_{inv} signal category.

2258

2259 In order to have a final m_T binning that is not highly model-dependent, we consolidate these
2260 four different bins into a single binning which is provided below:

2261 **[1500, 1600, 1700, 1800, 1900, 2025, 2175, 2350, 2575, 2825, 3125, 3500, 3925, 4450, 5075,
2262 6000]**